

5-2019

## A Hybrid Vortex Solution for Radial Equilibrium in Axial Compressors

Wenyu Li

Follow this and additional works at: <https://commons.erau.edu/edt>



Part of the [Aerospace Engineering Commons](#)

---

### Scholarly Commons Citation

Li, Wenyu, "A Hybrid Vortex Solution for Radial Equilibrium in Axial Compressors" (2019). *Dissertations and Theses*. 459.

<https://commons.erau.edu/edt/459>

This Thesis - Open Access is brought to you for free and open access by Scholarly Commons. It has been accepted for inclusion in Dissertations and Theses by an authorized administrator of Scholarly Commons. For more information, please contact [commons@erau.edu](mailto:commons@erau.edu).

A HYBRID VORTEX SOLUTION FOR RADIAL EQUILIBRIUM  
IN AXIAL COMPRESSORS

A Thesis

Submitted to the Faculty

of

Embry-Riddle Aeronautical University

by

Wenyu Li

In Partial Fulfillment of the

Requirements for the Degree

of

Master of Science in Aerospace Engineering

May 2019

Embry-Riddle Aeronautical University

Daytona Beach, Florida

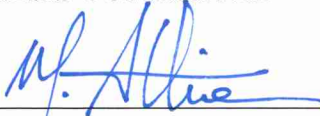
A HYBRID VORTEX SOLUTION FOR RADIAL EQUILIBRIUM  
IN AXIAL COMPRESSORS

by

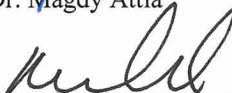
Wenyu Li

A Thesis prepared under the direction of the candidate's committee chairman, Dr. Magdy Attia, Department of Aerospace Engineering, and has been approved by the members of the thesis committee. It was submitted to the School of Graduate Studies and Research and was accepted in partial fulfillment of the requirements for the degree of Master of Science in Aerospace Engineering.

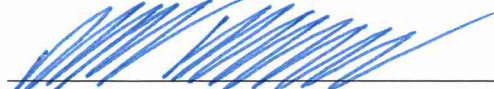
THESIS COMMITTEE



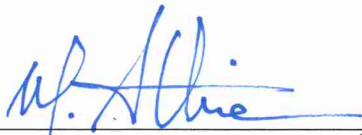
Chairman, Dr. Magdy Attia



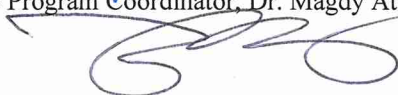
Member, Dr. Reda Mankbadi



Member, Dr. Mark Ricklick



Graduate Program Coordinator, Dr. Magdy Attia



Dean of College of Engineering, Dr. Maj Mirmirani



Senior Vice President for Academic Affairs and Provost, Dr. Lon Moeller

4.22.2019

Date

4/22/2019

Date

4/22/19

Date

## ACKNOWLEDGMENTS

I would like to express my appreciation to my advisor, Dr. Magdy Attia, for his guidance and support throughout the thesis and all the meetings and discussions that we had. Not only his academic advices but also his career advices are invaluable to me.

I would like to thank my parents who sponsor my study and my boyfriend who has always been there for me and cheered me up. Without their support, I would never be able to finish my degree.

Finally, I would like to extend my appreciation to my colleagues in the Gas Turbine Lab, Christian Guzman, Anish Prasad, Neil Sullivan, Shane Colon, Karthik Krishna and Michael Blaser; for your helps during my study in ERAU. I will remember those late nights in the lab when we had discussions and lightened the mood during stressful times.

## TABLE OF CONTENTS

ACKNOWLEDGMENTS .....	iii
TABLE OF CONTENTS.....	iv
LIST OF TABLES .....	vi
LIST OF FIGURES .....	vii
SYMBOLS.....	xi
ABBREVIATIONS .....	xii
ABSTRACT.....	xiii
1. Introduction.....	1
1.1. Development of Axial Compressors .....	1
1.1.1. Preliminary Design.....	2
1.1.2. Throughflow and Streamline Curvature .....	3
1.1.3. 2D Blade Design.....	5
1.1.4. 3D Blade Design.....	6
1.2. Current Design Dilemma .....	6
1.3. Compressor Map .....	7
1.3.1. Compressor Stall/ Surge.....	8
1.4. Problem Statement .....	9
2. Literature Review .....	11
2.1. Radial Equilibrium .....	11
2.2. Simple Radial Equilibrium Equation (SREE) .....	11
2.3. Actuator Disk Theory.....	12
2.4. Modifications to the SREE (Deriving Radial Equilibrium with Streamline Curvature) 13	
3. Hybrid Vortex Concept and Derivations.....	15
3.1. Concept .....	15
3.2. Equation Derivation .....	17
3.3. Hybrid Vortex Implementation .....	19
4. Blade Design and Methodology .....	22
4.1. 1D Design .....	22
4.1.1. Baseline Design Choice .....	22
4.1.2. Hybrid Vortex Design Cases .....	25
4.1.3. Meanline and Throughflow .....	33
4.2. 2D Design and CFD .....	35
4.2.1. 2D Meshing and Sensitivity Studies .....	35
4.3. 3D Design and CFD .....	38
4.3.1. 3D Meshing and Sensitivity Studies .....	39
4.3.2. Simulation Setup .....	41

5.	Results.....	45
5.1.	Baseline – Free Vortex.....	45
5.1.1.	1D Design Point .....	45
5.1.2.	2D Airfoil Design .....	46
5.1.3.	3D Performance and Observation .....	47
5.2.	Hybrid Vortex.....	52
5.2.1.	1D Design Point .....	52
5.2.2.	Axial Velocity Convergence Iteration .....	52
5.3.	Final Hybrid Vortex Case .....	53
5.3.1.	2D Airfoil Stacking and Comparison.....	53
5.3.2.	Observed Flow Features and Comparison .....	57
5.3.3.	Off-Design Behavior .....	66
6.	Conclusion .....	71
7.	Recommendations.....	73
	REFERENCES .....	74
A.	Radial Equilibrium Derivations.....	76
B.	Various Vortex Solutions .....	80
C.	NASA GRAPE Sample Input.....	81
D.	NASA RVCQ3D Sample Input.....	82
E.	Sample CFX Inlet Velocity Profile File .....	83
F.	2D Mach Profile Output for the Baseline Case .....	85
G.	2D Mach Profile Output for the Hybrid Vortex Case C.....	88
H.	2D Blade Geometry Comparison.....	91

## LIST OF TABLES

Table 4.1 Mid-Section Design Values .....	22
Table 4.2 Hybrid Vortex Solution Design Cases – LE Distribution .....	27
Table 4.3 2D Mesh Sensitivity study total nodes count.....	36
Table 4.4 2D Mesh Size and Parameters for Baseline Case. ....	40
Table 5.1 Mid-Section Design Values .....	45
Table 5.2 Baseline 3D Design Point Parameters .....	47
Table 5.3 Hybrid Vortex Case C 3D Design Point Parameters .....	57
Table 5.4 Design Point Values.....	67
Table 5.5 Mass Flow Operating Range Comparison .....	68
Table 5.6 Surge Margin Comparison.....	69
Table B.1 Vortex solutions (Horlock, 1958) .....	80

## LIST OF FIGURES

Figure 1.1 Four Stages of Turbomachinery Design (Molinari & Dawes, 2006). .....	2
Figure 1.2 Turbine Velocity Triangles for a Blade Row (Stodola, 1905). .....	2
Figure 1.3 Intersecting S1 and S2 Surface in a Blade Row (Wu, 1952).....	4
Figure 1.4 Two Interacting Surfaces:(a) Blade-to-Blade Surface and (b) Axisymmetric Analysis of Flow in a Meridional Plane (Cumpsty & Greitzer, 2004). .....	4
Figure 1.5 Cascade View of Axial Compressor (Philip & Peterson, 1992). .....	5
Figure 1.6 Axial Compressor Map (Hall & Dixon, 2013).....	7
Figure 1.7 Cascade Stall (Philip & Peterson, 1992). .....	9
Figure 2.1 Streamlines in Cylindrical Annulus for Simple Radial Equilibrium Assumption (Cumpsty & Greitzer, 2004). .....	12
Figure 2.2 Models for (a) Radial Equilibrium and (b) Actuator Disc Analysis (Horlock, 1958). .....	12
Figure 2.3 Flow Diagram for the Solution of Equation 2.2 (Korakianitis & Zou, 1993). ..	14
Figure 3.1 Three-Dimensional Flow Effects in a Cascade Tunnel (Howell, 1945). .....	15
Figure 3.2 Axial Velocity Radial Distribution Showing Uniform Profile (Yellow Line) and Profile with 3D Effects (Red Line) .....	16
Figure 3.3 Tangential Motion of A Small Fluid Element (Hill, 1992). .....	17
Figure 3.4 The Comparison of $v_{ax}$ Profile Shape Between Uniform Profile and Profile Derived from Equation 3.5 .....	18
Figure 3.5 Baseline Design Flowchart.....	20
Figure 3.6 Hybrid Vortex Design Flowchart .....	21
Figure 4.1 Constant Reaction 1D Design Angle Distribution .....	23
Figure 4.2 Forced Vortex 1D Design Angle Distribution .....	23
Figure 4.3 Free Vortex 1D Design Angle Distribution .....	24
Figure 4.4 Exponential 1D Design Angle Distribution .....	24
Figure 4.5 Circumferential Mass Flow Averaged Axial Velocity Profiles for R1 and S1 Using Steady and Unsteady Simulations (Zheng, 2017) .....	26
Figure 4.6 Fitting Curve for Axial Velocity Profile of The First Rotor Outlet .....	26
Figure 4.7 Trailing Edge Pressure Profile Comparison between The Free Vortex Solution (a) and The Hybrid Vortex Solution (b) .....	27
Figure 4.8 LE Velocity triangle comparison at 50% .....	29
Figure 4.9 LE Velocity Triangle Comparison at (a) 2% Span Location and (b) 98% Span Location .....	30



Figure 4.10 Pressure Distribution at the Trailing Edge for case B without modification (a) and With “tip-strong” modification (b).....	32
Figure 4.11 Pressure Distribution at the Trailing Edge Hub for case B without modification (a) and with “tip-strong” modification (b).....	33
Figure 4.12 CSPAN code flowpath result.....	34
Figure 4.13 ACD 3D Blade Elements Stacking.....	34
Figure 4.14 Mesh Sensitivity Analysis for Baseline at 3% Location (a) and Enlarged View (b) .....	36
Figure 4.15 Hybrid Vortex Case Grid Sample of LE at 35 % Span (a) and LE Enlarged View at 35 % Span (b) .....	37
Figure 4.16 Density Contour at 35 % Span for Free Vortex Case(a) and Hybrid Vortex Case (b) .....	37
Figure 4.17 Mach Profile at 35 % Span for Free Vortex Case (a) and Hybrid Vortex Case (b).....	38
Figure 4.18 Topology Example .....	39
Figure 4.19 Final Domain Mesh (a) and LE Enlargement View (b) .....	40
Figure 4.20 Final Domain Mesh with Mesh Planes (a) and Tip Gap Enlargement (b) ....	40
Figure 4.21 Results for Baseline Case Using SST and SST+RM Comparison .....	42
Figure 4.22 RMS Convergence Sample near the Design Point .....	43
Figure 4.23 Mass Imbalance Convergence Sample near the Design Point .....	43
Figure 4.24 RMS Convergence Sample near the Surge Line .....	44
Figure 4.25 Mass Imbalance Convergence Sample near the Surge Line .....	44
Figure 5.1 Free Vortex Baseline Blade Stacking View .....	46
Figure 5.2 Free Vortex Baseline 3% Span location Velocity Streamline Plot .....	47
Figure 5.3 Free Vortex Baseline 3% Span location Velocity Contour .....	48
Figure 5.4 Free Vortex Baseline 35% Span location Density Contour (a) and LE Enlarged View(b) .....	49
Figure 5.5 Free Vortex Baseline Streamline Plot near Hub (Side View) .....	49
Figure 5.6 Static Pressure Distribution Comparison for the Baseline Case .....	50
Figure 5.7 Mach Profile Comparison for Baseline Case (a) 3% Span Location and (b) 35% Span Location .....	51
Figure 5.8 Mach Profile Comparison for Baseline Case at 98% Span Location.....	51
Figure 5.9 The Comparison of Vax Profile Shape.....	53
Figure 5.10 Hybrid Vortex Case C Blade Stacking View .....	54
Figure 5.11 3D Blades Geometry Comparison (a) Free Vortex and (b) Hybrid Vortex	

Case C .....	55
Figure 5.12 2D Airfoils Shape Comparison at 3% Span Location .....	55
Figure 5.13 2D Airfoils Shape Comparison at 35% Span Location .....	56
Figure 5.14 3D Geometry Comparison between Baseline Case (a) and Hybrid Vortex Case C (b) .....	57
Figure 5.15 Hybrid Vortex Case C 35% Span location Density Contour (a) and LE Enlarged View(b).....	58
Figure 5.16 Baseline Case Flow Path Streamline Plot on 3% Span Location (Side View) .....	59
Figure 5.17 Hybrid Vortex Case C Flow Path Streamline Plot on 3% Span Location (Side View).....	60
Figure 5.18 Baseline Case Flow Path Streamline Plot on 3% Span Location (Front View) .....	60
Figure 5.19 Hybrid Vortex Case C Flow Path Streamline Plot on 3% Span Location (Front View).....	61
Figure 5.20 Baseline Case Flow Path Streamline Plot on 10% Span Location (Side View) .....	62
Figure 5.21 Hybrid Vortex Case C Flow Path Streamline Plot on 10% Span Location (Side View) .....	62
Figure 5.22 Baseline Case Flow Path Streamline Plot on 10% Span Location (Front View).....	63
Figure 5.23 Hybrid Vortex Case C Flow Path Streamline Plot on 10% Span Location (Front View).....	63
Figure 5.24 Static Pressure Distribution Comparison for Baseline Case (a) and Hybrid Vortex Case C (b) .....	64
Figure 5.25 Mach Profile Comparison for Hybrid Vortex Case C (a) 3% Span Location and (b) 35% Span Location.....	65
Figure 5.26 Mach Profile Comparison for Hybrid Vortex Case C at 98% Span Location.....	65
Figure 5.27 Compressor Map Comparison between Free Vortex Case and Hybrid Vortex Case C .....	66
Figure 5.28 Characteristic Line Comparison at RPM 6100 between Free Vortex Case and Hybrid Vortex Case C.....	67
Figure 5.29 Hypothetical Characteristic Line Comparison at RPM 6100 between Free Vortex Case and Hybrid Vortex Case C .....	68
Figure 5.30 Hypothetical Compressor Map Comparison between Free Vortex Case and Hybrid Vortex Case C.....	69
Figure F.1 Free Vortex Baseline 3% Span location 2D Mach Profile.....	85

Figure F.2 Free Vortex Baseline 35% Span location 2D Mach Profile.....	85
Figure F.3 Free Vortex Baseline 61% Span location 2D Mach Profile.....	86
Figure F.4 Free Vortex Baseline 82% Span location 2D Mach Profile.....	86
Figure F.5 Free Vortex Baseline 98% Span location 2D Mach Profile.....	87
Figure G.1 Hybrid Vortex Case C 3% Span location 2D Mach Profile .....	88
Figure G.2 Hybrid Vortex Case C 35% Span location 2D Mach Profile .....	88
Figure G.3 Hybrid Vortex Case C 61% Span location 2D Mach Profile .....	89
Figure G.4 Hybrid Vortex Case C 82% Span location 2D Mach Profile .....	89
Figure G.5 Hybrid Vortex Case C 98% Span location 2D Mach Profile .....	90
Figure H.1 2D Airfoil Comparison at 3% Span location.....	91
Figure H.2 2D Airfoil Comparison at 35% Span location.....	91
Figure H.3 2D Airfoil Comparison at 61% Span location.....	92
Figure H.4 2D Airfoil Comparison at 82% Span location.....	93
Figure H.5 2D Airfoil Comparison at 98% Span location.....	94

## SYMBOLS

$\alpha$	Absolute Flow Angle
$\beta$	Relative Flow Angle
$\gamma$	Specific Heat Ratio
$\Delta$	Change
$\sigma$	Solidity
$\sigma_s$	Stagger
$\delta$	deviation
$\eta$	Efficiency
$\pi$	Pressure Ratio
$\rho$	Density
$\Phi$	Flow Coefficient
$\lambda$	Work Coefficient
$U$	Tangential /Circumferential velocity
$V$	Absolute velocity
$W$	Relative velocity
$r$	Radial Direction
$ax$	Axial Direction
$u$	Tangential /Circumferential Direction

## ABBREVIATIONS

2D	Two-Dimensional
3D	Three-Dimensional
CFD	Computational Fluid Dynamics
DF	Diffusion Factor
DH	DeHaller Number
FV	Free Vortex
GRAPE	Grids about Airfoils using Poisson's Equation
H/T	Hub-to-Tip Ratio
HV	Hybrid Vortex
I/O	Input/Output
LE	Leading Edge
NACA	National Advisory Committee for Aeronautics
NASA	National Aeronautics and Space Administration
NoB	Number of Blades
RM	Reattachment Modification
RPM	Revolutions Per Minute
RVCQ3D	Rotor Viscous Quasi-3D
SM	Surge Margin
SREE	Simple Radial Equilibrium Equation
SST	Shear-Stress-Transport
T.M.	Turbomachinery
TE	Trailing Edge

## ABSTRACT

Li, Wenyu MSAE, Embry-Riddle Aeronautical University, May 2019. A Hybrid Vortex Solution For Radial Equilibrium In Axial Compressors.

A hybrid vortex solution using the radial equilibrium equation for three-dimensional design in axial compressors is generated. One of the most common used vortex solutions is Free Vortex. However, it ignores the fact that axial velocity varies with radius. The Hybrid Vortex includes axial velocity distribution with radius, which gives a more effective design. A single stage is first designed using the Free Vortex design method. A low hub-to-tip ratio is set to ensure subsonic flow. The axial velocity profile is exported from the CFX solver of the inlet diffuser. Using the Hybrid Vortex solution to the radial equilibrium equation, a redesign is conducted by altering the circumferential velocity distribution to adhere to the imported axial velocity distribution and the newly derived method. A tip-strong pressure distribution is also used in new design to adjust loading on the blade. CFX simulations are generated after 1D design, meanline design, throughflow design and blade design.

One of the key factors to evaluate compressor operation is off-design performance, which can be represented by the compressor map. Compressor maps are also generated and compared for each blade to show the advantage of the new design approach. It can be said that, by introducing real axial velocity profiles, complete with 3D effects, into the early stages of design and incorporating it with the new vortex solution, this new design approach delivers airfoils that are better aligned to the real boundary conditions with enhanced surge and stability margins, which is verified by CFD results.

## 1. Introduction

### 1.1. Development of Axial Compressors

One of the first documented turbomachinery invention can be traced back to 60 A. D. It was Heron of Alexandria (Greek origin) who designed the first steam engine. A radial flow reaction steam engine was a sphere rotated by hot steam expanding and going through attached pipes (Krain, 2005). However, there was no remarkable development until the emergence of Euler's Turbomachinery Equation and one-dimensional analysis of Fluid Dynamics. In the eighteenth century, Leonhard Euler analyzed Heron's steam turbine and performed experiments which resulted in "Euler's Equation". (Wilson, 1998) It can be described as "the change of the angular momentum is equal to the sum of the external moments". Stodola (Stodola, 1905) was the first to introduce the velocity vector relationships between blade row inlet and outlet. It was a milestone for later developments, and it is still widely taught as a primary tool for blade design.

In 1930, Frank Whittle was the first to patent a turbojet engine with an axial-plus-centrifugal compressor and a two-stage turbine, but he failed to make it run on his first flight. (Wilson, 1998) However, even though Hans von Ohain started later than Whittle, he succeeded in his first engine sooner. It had a centrifugal compressor driven with a radial turbine. Notice that the concepts of centrifugal compressor and axial compressor came up around the same time, but the development of axial compressor was slower. This is because axial compressors are more aerodynamically demanding.

The unique advantages of axial compressors are less frontal area and more capability to ingest higher mass flow, making it play an important role in modern propulsion. After decades of development, the general design process of axial

compressors can be divided into four parts, preliminary design, throughflow design, 2D blade design and 3D blade design, as shown in Figure 3.1. (Molinari & Dawes, 2006)

The detailed design procedure and applied theories will be discussed in later sections.

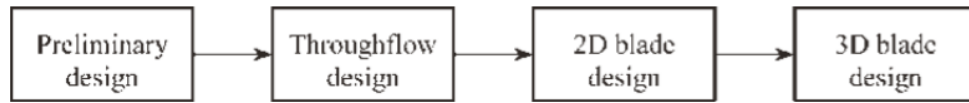


Figure 1.1 Four Stages of Turbomachinery Design (Molinari & Dawes, 2006).

### 1.1.1. Preliminary Design

Preliminary design is where one-dimensional and two-dimensional treatments are implemented. It resolves aerodynamic and thermodynamic properties at a specified spanwise location using empirical correlations. As mentioned above, one-dimensional analysis, Euler's Turbomachinery Equation, and the velocity triangles introduced by Stodola (Stodola, 1905) are applied in this stage.

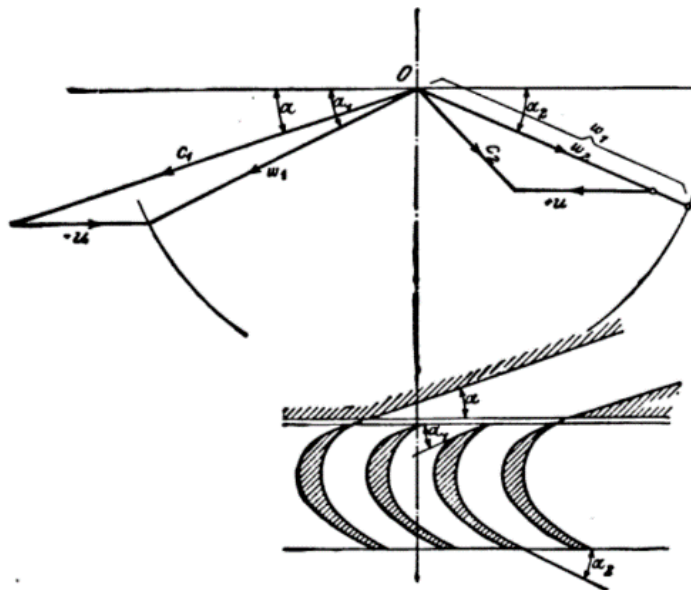


Figure 1.2 Turbine Velocity Triangles for a Blade Row (Stodola, 1905).



However, although one-dimensional treatment is useful, it is at an elementary level. Early on it was determined that blade rows should be considered as passages with more emphasis on blade shapes. It was discovered that the inlet and outlet flow angle, maximum thickness, and camber distributions are what really mattered. Two-dimensional treatment was considered. According to cascade tests, new correlation for blade row performance was introduced by Lieblein (Lieblein, 1965), which is called the diffusion factor as shown in (1.1).

$$D = \left(1 - \frac{V_2}{V_1}\right) + \frac{\Delta V_\theta}{2\sigma V_1} \quad (1.1)$$

The diffusion factor, as a function of blade shape and cascade configuration, managed to connect the blade aerodynamic loading and blade geometry together and evaluate blade losses at a very early stage of design.

### **1.1.2. Throughflow and Streamline Curvature**

The difficulties occur when hub-to-tip ratio is small, or the slope of the annulus walls is large. The change of radius causes unneglectable radial accelerations, which leads to three-dimensional considerations. The first effective approach related to this problem was introduced by Wu (Wu, 1952). He simplified the flow through a cascade into two parts: blade-to-blade (S1) and hub-to tip (S2) along a stream surface, as shown in Figure 1.3. By introducing the radial dimension, this theory allows axisymmetric analysis. And later on, both throughflow method and streamline curvature method, which are still commonly used today, were based on Wu's theory.

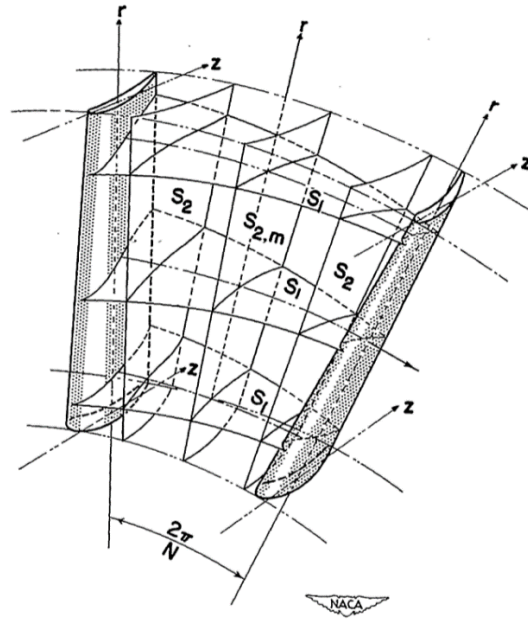


Figure 1.3 Intersecting S1 and S2 Surface in a Blade Row (Wu, 1952).

The throughflow calculation decouples two surfaces and solves them separately, furthermore, it solves on a blade-to-blade surface and meridional plane instead of S2 surface as presented in Figure 1.4.

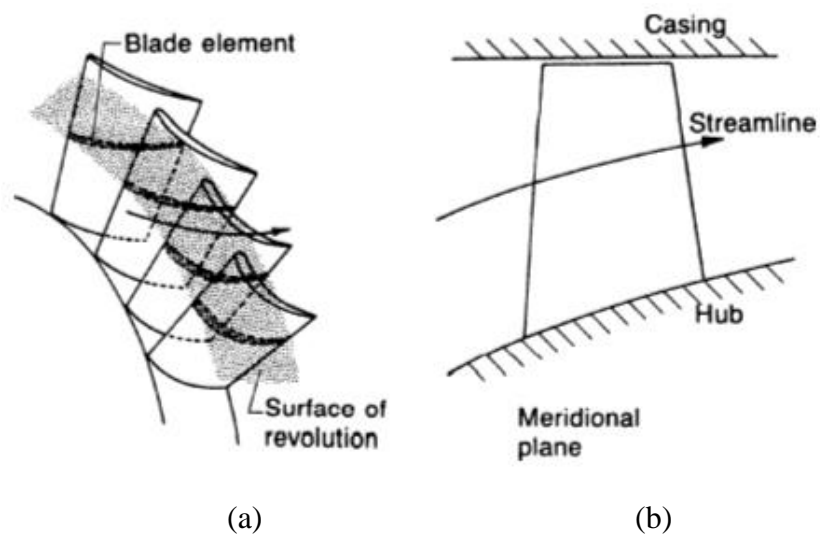
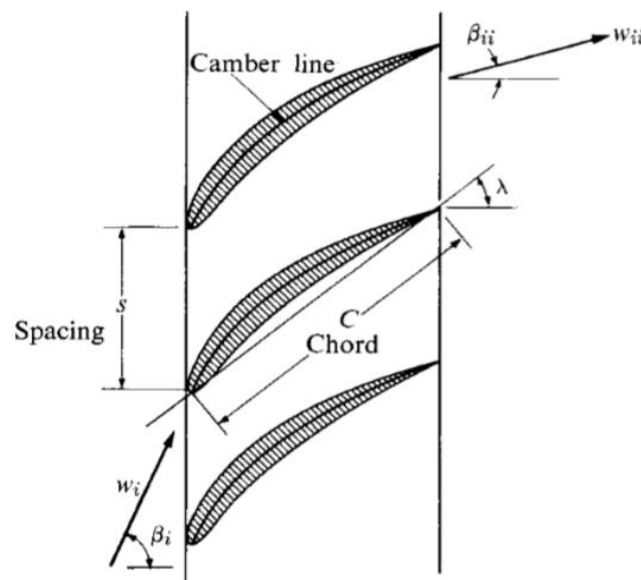


Figure 1.4 Two Interacting Surfaces:(a) Blade-to-Blade Surface and (b) Axisymmetric Analysis of Flow in a Meridional Plane (Cumpsty & Greitzer, 2004).

An iterative calculation process between the two surfaces is necessary. The radial component of the momentum equation is calculated along the curvature of the streamlines until the solution has converged for mass-flow balance. (Cumpsty & Greitzer, 2004; Wilson, 1998)

### 1.1.3. 2D Blade Design

As mentioned before, the diffusion factor can evaluate the blade losses based on inlet, outlet flow conditions, and blade solidity. However, it cannot estimate the peak local suction-surface velocity, which is a key factor of flow separation as well. With the development of computer and numerical method, it not only takes account of inlet and outlet flow conditions but also allows us to fully investigate flow in a cascade, as shown in Figure 1.5.



*Figure 1.5 Cascade View of Axial Compressor (Philip & Peterson, 1992).*

There are two different approaches: one is called the inverse approach, and the other one is called the direct approach. (Köller & Schreiber, 1999) The inverse approach

is to solve the equations of motion, generate the appropriate singularity (logarithms at the inlet and outlet velocities) and examine the streamline passing through the stagnation point, which describes the shape of the airfoil. (Korn, 1978) The direct approach is to start from a contour shape and then describe the boundary conditions, which leads to less computing time. (Schmidt, 1980) After the shapes of the airfoil for each section are determined, the 3D blade geometry can be generated.

#### **1.1.4. 3D Blade Design**

Notice that both throughflow calculation and the 2D blade design include boundary-layer calculations to some extent, but they are still inviscid and compressible solutions; neither of them includes viscous losses. Therefore, the blockage caused by three-dimensional separation is impossible to predict in previous stage of the design. (Cumpsty & Greitzer, 2004; Korn, 1978) The use of computational turbulence models, Reynolds averaged Navier-Stokes equations (RANS), is a landmark for turbomachinery design. It makes viscous effects possible to be examined. Thus, three-dimensional blade design is a tool to assess and refine the final blade geometry using CFD tools.

#### **1.2. Current Design Dilemma**

The possibility of whether the current turbomachinery design can have a further improvement is mainly in two aspects: design methodology and design process. For design methodology, the losses near the end walls because of viscous effects were never included until the last stage of 3D blade design. However, the purpose of 3D blade design is more concerned on testing and verifying blade behavior other than making major changes. The three-dimensional method still needs to be accommodated and understood.

As for the design process, it is classified into three main categories: design-by-

analysis, design optimization and design-by-sensitivity. (Molinari & Dawes, 2006)

However, both the design optimization and the design-by-sensitivity processes require high computational cost. The design-by-analysis process is not highly demanding for computational resources, but it has its own disadvantages. The designer cannot predict the effects of the modification to the design until it is examined by expensive trial and error.

### 1.3. Compressor Map

The general performance of a high-speed compressor can be represented by its compressor map. As shown in the example in Figure 1.6, the pressure ratio across the whole compressor is a function of mass flow rate for several fixed rotational speeds. (Hall & Dixon, 2013) Each of the constant-speed characteristic lines terminate at the surge line. Beyond the surge line, the operation of the compressor becomes aerodynamically unstable.

A compressor can operate at anywhere on the map below the surge line and above the choke line, but it is often constrained on a single operating line where the compressor performance is matched to the other components of the engine such as the turbine.

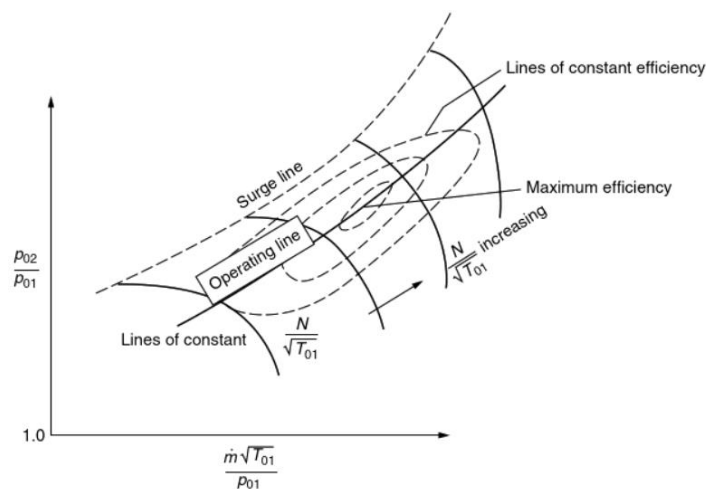


Figure 1.6 Axial Compressor Map (Hall & Dixon, 2013).

The Surge Margin is one method to quantify the operating limit of the compressor. (Cumpsty, 1989) There are many different ways of defining surge margin.

Equation (1.2) shows the most popular definition:

$$SM = \frac{(\pi_s - \pi_{0-design})}{\pi_{0-design}} \quad (1.2)$$

In Equation (1.2), where  $\pi_{0-design}$  is defined as the design point total pressure ratio, and  $\pi_s$  is the pressure ratio on the surge line for the same mass flow rate as the condition on the design operating line. There is another definition given by Dixon (Hall & Dixon, 2013), where  $\pi_s$  is the pressure ratio on the surge line for the same rotating speed on the characteristic line. In general, larger surge margin indicates more ability to deal with aerodynamic instability, which is a key limiting factor of compressor design.

### 1.3.1. Compressor Stall/ Surge

As shown in Figure 1.7, when operating under normal conditions, increasing  $\beta_i$  does not affect  $\beta_{ii}$ , but it will increase the adverse pressure gradient on the suction surface of the blade. When the adverse pressure gradient rises to an intolerable level, boundary layer separation will happen and will result in increasing  $\beta_{ii}$ . Similarly, decreasing  $\beta_i$  beyond a reasonable level, separation will occur on the pressure surface of the blade. Separation resulting from increasing  $\beta_i$  is called ‘positive stall’, while separation resulting from reducing  $\beta_i$  is called ‘negative stall’. (Philip & Peterson, 1992)

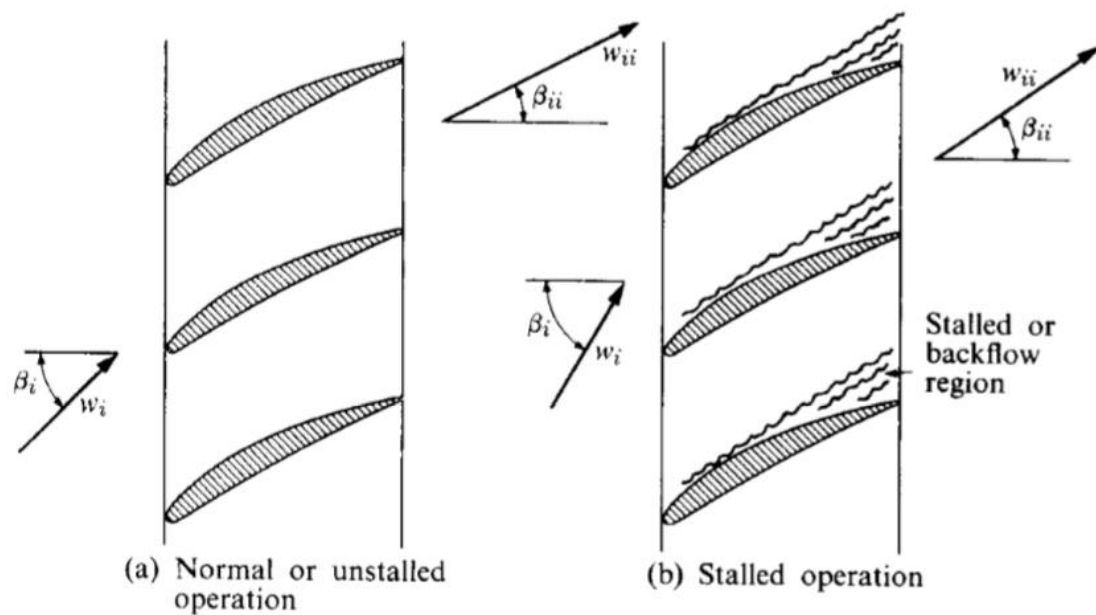


Figure 1.7 Cascade Stall (Philip & Peterson, 1992).

Rotating stall (Hall & Dixon, 2013) is another phenomenon when the blade reaches the 'stall point'. Instead of all stalling together, only some of the blades will stall and the stall patches travel around the compressor annulus. So, rotating stall is a circumferential disturbance of the flow in the compressor. Moreover, rotating stall could initiate surge, which is a disturbance that affects flow conditions throughout the entire compression system. Both instabilities need to be avoided in compressor design. (Day, 1971).

#### 1.4. Problem Statement

As it is well known, turbomachinery design is an iterative process involving optimization until the design goal is achieved. Looking at the big picture, preliminary design has a more lasting impact compared to the others. It is because that is where the main stage characteristics are decided. However, there is no direct understanding how

subtle changes in preliminary design will affect the later stages of design and overall performance. Thus, the iterations between these design steps tend to be lengthy and time consuming. In this paper, a new hybrid vortex solution is introduced, and compared with other existing vortex solutions used in preliminary design. The goal is to introduce a higher level of fidelity early into the design process that is based on the actual physics of the flow. This will produce a better airfoil in less time, minimize iterations, and extend the surge margin of the fan or the compressor.



## 2. Literature Review

### 2.1. Radial Equilibrium

As mentioned before, two-dimensional treatment doesn't consider radial change. It is acceptable when the hub-to-tip ratio is between 0.85 - 1.0, because there are only small changes of the velocity diagram with radius. (Wilson, 1998) However, the hub-to-tip ratio is below 0.75, the change of radius is large enough that the velocity diagrams are completely different from hub to tip. The thinking of altering the velocity triangles along spanwise and taking account of huge static pressure change along spanwise in order to balance the centrifugal force is called radial equilibrium.

### 2.2. Simple Radial Equilibrium Equation (SREE)

The solution for the change of velocity diagrams for axial compressor is simple radial equilibrium equation (SREE), as shown in Equation (2.1). Detailed derivation will be given in Appendix "A".

$$\frac{d}{dr} (V_{ax})^2 = -\frac{1}{r^2} \frac{d}{dr} (rV_u)^2 \quad (2.1)$$

With a tangential velocity distribution given, the axial velocity distribution can be determined. Horlock summarized several vortex solutions (Free Vortex, Constant Reaction, Exponential and Forced Vortex) which will be presented in Appendix "B". Notice that the Equation (2.1) is valid for constant work delivery and constant total pressure loss along the radius. (Horlock, 1958) Simple radial equilibrium is still an approximation because it assumes negligible streamlines curvature in other directions (except for centrifugal direction). Furthermore, it also implies that the streamlines follow a constant radius path between blade rows, as shown in Figure 2.1.

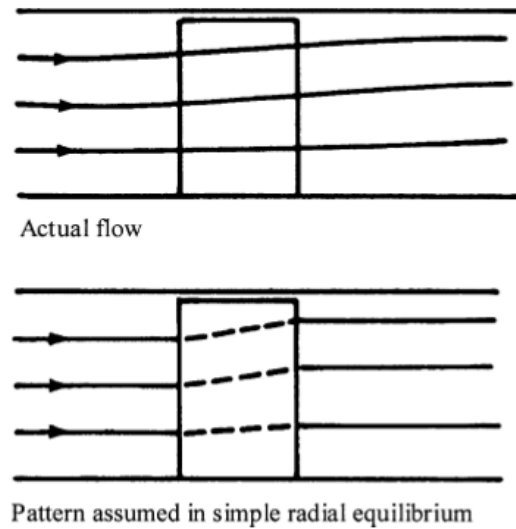


Figure 2.1 Streamlines in Cylindrical Annulus for Simple Radial Equilibrium Assumption (Cumpsty & Greitzer, 2004).

### 2.3. Actuator Disk Theory

An alternative approach for radial equilibrium is called actuator disk theory. It is assumed that all the flow turning in the blade row is achieved in a very small axial distance- within an actuator disc, as shown in Figure 2.2(b).

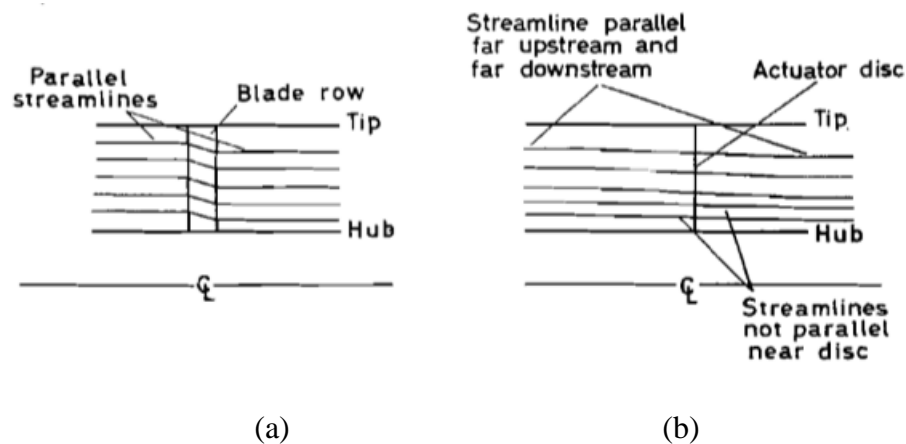


Figure 2.2 Models for (a) Radial Equilibrium and (b) Actuator Disc Analysis (Horlock, 1958).

However, the actuator disk theory has its own limitation. Because it assumes that the radial velocity and the product of axial velocity and density are continuous across the disk, the mathematic complexity is huge especially with various radius and density. (Cumpsty & Greitzer, 2004) Even though it is not very applicable in axisymmetric turbomachinery problems, but it becomes useful in other two areas: inlet distortions and conjunction with three-dimensional computation to represent boundary conditions.

#### **2.4. Modifications to the SREE (Deriving Radial Equilibrium with Streamline Curvature)**

The lengthwise change in radius will create an additional pressure gradient acting on the flow in axial compressors. Although the SREE can be used to balance the centrifugal force caused by spanwise change in radius, it assumes constant radius path between blade rows. Therefore, it fails to take into effect the additional pressure gradient from the streamwise change of streamline curvature. (Wilson, 1998)

Korakianitis and Zou (Korakianitis & Zou, 1993) proposed a throughflow streamline method in addition to the SREE. With the assumption of  $\frac{ds}{dr} = 0$ , the Equation (2.1) was rederived and became Equation (2.2):

$$\begin{aligned} \frac{dV_{ax}(r, u)}{dr} + \frac{V_{ax}(r, u)}{1 + \tan^2 \alpha_u} \left[ \frac{\sin \alpha_u}{\cos^3 \alpha_u} \frac{d\alpha_u}{dr} - \frac{1}{\cos^2 \alpha_r} \frac{d\alpha_r}{dx} + \frac{\tan^2 \alpha_u}{r} \right] \\ - \frac{\tan \alpha_r}{1 + \tan^2 \alpha_u} \frac{dV_{ax}(r, u)}{dx} = \left[ \frac{dh_0}{dr} \right] = 0 \end{aligned} \quad (2.2)$$

The Equation (2.2) must be solved numerically with an iterative process, as shown in *Figure 2.3*. This approach succeeds in solving radial equilibrium with streamwise radial change at different locations of streamlines. But it requires computational effort and it is not applicable in preliminary design as the SREE.

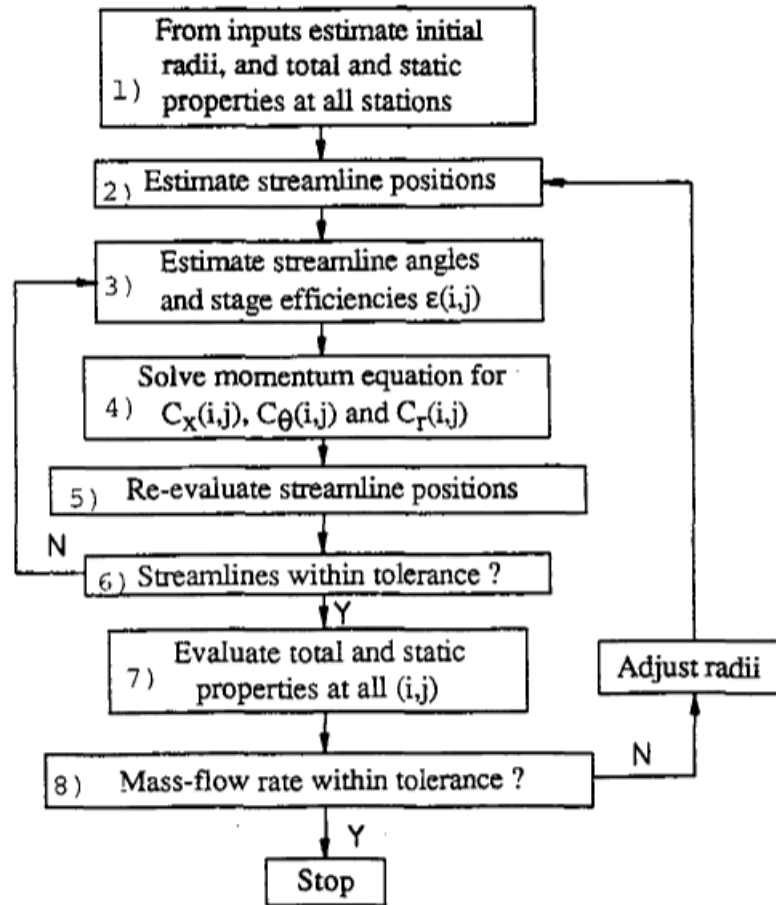
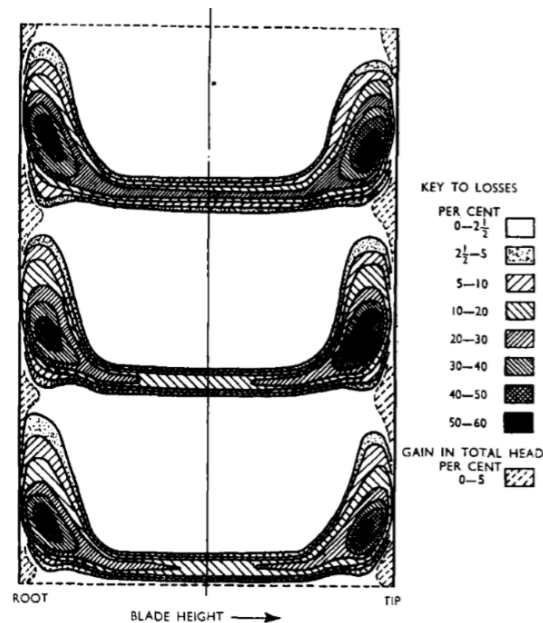


Figure 2.3 Flow Diagram for the Solution of Equation 2.2 (Korakianitis & Zou, 1993).

### 3. Hybrid Vortex Concept and Derivations

#### 3.1. Concept

As mentioned before, the simple radial equilibrium equation has the advantage of predicting swirling flow between blades rows and providing a radial pressure distribution from hub to tip, but it still has some drawbacks. As studied by Howell (Howell, 1945), the performance analysis of the compressor was conducted by using two-dimensional cascade tunnel data with certain correction factor. As shown in Figure 3.1, the losses in a cascade are due to the boundary layers buildup on the wall, tip clearance and wakes from the previous blade rows. It is very clear that the losses are not uniform. So, either more work must be put into where the losses are high (especially near the end walls), or the assumption of uniform axial velocity will fail.



*Figure 3.1 Three-Dimensional Flow Effects in a Cascade Tunnel (Howell, 1945).*

A new vortex solution is introduced and is named the Hybrid Vortex Solution.

The intent is to infuse the reality of the end wall, and other losses, effects directly into the

equation. Instead of assuming some axial velocity distribution which cannot well represent three-dimensional effects, an axial velocity profile after an inlet guide vane will be imported into the radial equilibrium equation to derive a correlated tangential velocity distribution. The axial velocity profile selected for this study was constructed by Howell (Howell, 1945), with the boundary layer being fully considered, as shown in Figure 3.2. This realistic profile is more accurate and reliable than a constant profile. In this thesis, curve 0 is selected as the desired input for the Hybrid Vortex derivation, however, the method is independent of the profile's shape and other profiles may be selected depending on the circumstance.

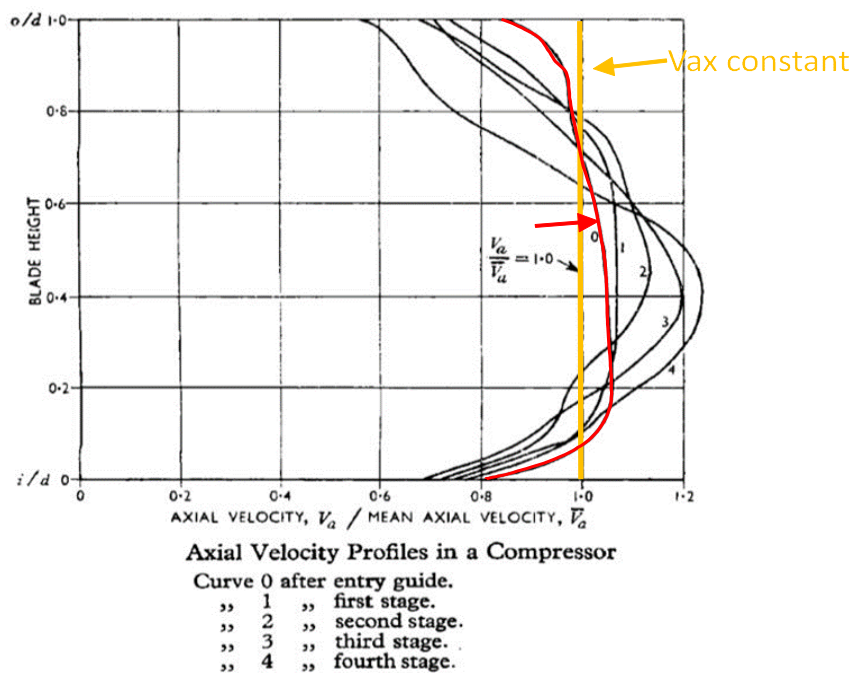


*Figure 3.2* Axial Velocity Radial Distribution Showing Uniform Profile (Yellow Line) and Profile with 3D Effects (Red Line)

### 3.2. Equation Derivation

The purpose of the vortex solution is to add a pressure force (from tip to hub) to balance the centrifugal force (from hub to tip) that develops when the blade is spinning (Philip Hill, 1992). The centrifugal force can be represented as in Equation (3.1).

$$F_r = \delta m \cdot \frac{V_u^2}{r} \quad (3.1)$$

To ensure radial equilibrium, a pressure gradient in the radial direction is assumed and resolved according to Newton's Second Law for a flow particle:

$$\begin{aligned} P(r d\theta dx) - \left( P + \frac{\partial P}{\partial r} dr \right) ([r + dr] dx d\theta) + 2(P dr dx) \frac{d\theta}{2} \\ = -\delta m \cdot \frac{V_u^2}{r} \end{aligned} \quad (3.2)$$

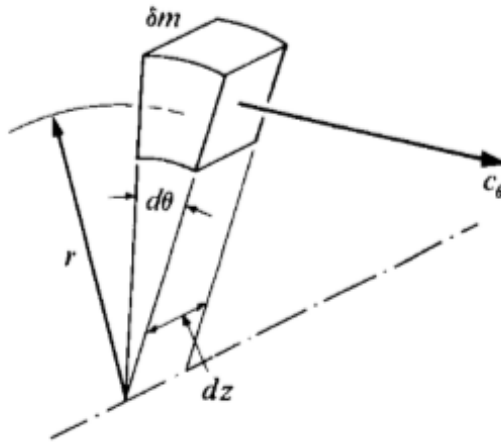


Figure 3.3 Tangential Motion of a Small Fluid Element (Hill, 1992).

Thus, the pressure distribution can be written as

$$\frac{\partial P}{\partial r} = \rho \cdot \frac{V_u^2}{r} \quad (3.3)$$

With the assumptions of incompressible flow; total pressure, stagnation enthalpy and entropy do not vary with radius, Equation (3.4) can be derived. Full derivations are shown in Appendix “A”.

$$\frac{d}{dr} (V_{ax})^2 = -\frac{1}{r^2} \frac{d}{dr} (rV_u)^2 \quad (3.4)$$

Axial velocity and circumferential velocity are correlated together by this equation as a function of radius to represent the radial pressure distribution. In order to produce the new vortex solution, a matching curve and corresponding equation are generated by using Plot Digitizer and MATLAB. The equation describing the axial velocity distribution is:

$$\begin{aligned} V_{ax} = & 9.4718 \times 10^6 r^7 - 2.7984 \times 10^7 r^6 \\ & + 3.3557 \times 10^7 r^5 - 2.148 \times 10^7 r^4 \\ & + 7.9936 \times 10^6 r^3 - 1.739 \times 10^6 r^2 \\ & + 2.0553 \times 10^5 r - 10073 \end{aligned} \quad (3.5)$$

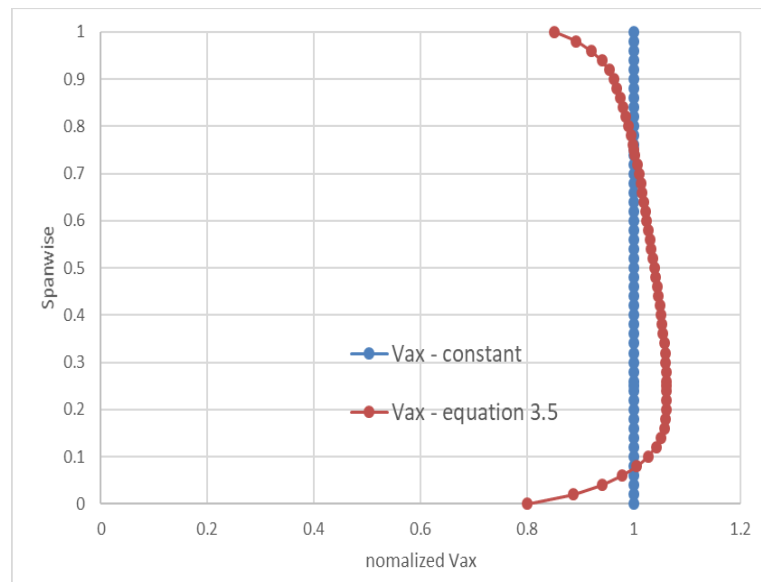


*Figure 3.4* The Comparison of  $V_{ax}$  Profile Shape Between Uniform Profile and Profile Derived from Equation (3.5)



The corresponding comparison of the axial velocity profile shapes is shown in Figure 3.4 above. With this axial velocity (Equation (3.5), and from Equation (2.1)), the tangential velocity profile can be obtained:

$$\begin{aligned}
 V_u = & \text{SQRT}(-7.85 \times 10^{13}r^{16} + 4.594 \times 10^{14}r^{15} \\
 & - \frac{8.512 \times 10^{15}r^{14}}{7} + \frac{2.51 \times 10^{16}r^{13}}{13} \\
 & - \frac{6.199 \times 10^{15}r^{12}}{3} + \frac{1.729 \times 10^{16}r^{11}}{11} \\
 & + 8.79 \times 10^{14}r^{10} + \frac{3.3 \times 10^{15}r^9}{9} - 1.147 \times 10^{14}r^8 \\
 & + \frac{1.865 \times 10^{14}r^7}{7} - \frac{1.348 \times 10^{13}r^6}{3} + 5.25 \times 10^{11}r^5 \\
 & - 3.86 \times 10^{10}r^4 + 1.38 \times 10^9r^3 - 93576.6)/r
 \end{aligned} \tag{3.6}$$

As can be seen in Equation (3.6), the non-constant distribution of the axial velocity component results in a highly non-linear radial equilibrium equation. This new solution alters the circumferential component and the entire velocity triangle, as will be demonstrated in later sections.

### 3.3. Hybrid Vortex Implementation

The general turbomachinery design process can be divided into four stages, preliminary design, throughflow design, 2D blade design and 3D blade design. With the development of computers, computational tools play a key role in advancing turbomachinery design. Meanline (Arthur, 1995) and Throughflow codes (Crouse, 1981) are used for one-dimensional analysis to obtain stream surface designs. NASA's grid generating code, GRAPE, and Quasi 3-D Viscous solver Code, RVCQ3D (Chima, 1999) are used for the two-dimensional blade design in order to get an optimized 2D streamsection profile which corresponds to the aerodynamic and thermodynamic boundary conditions gained from the throughflow design. Then, the airfoil will be

stacked in ANSYS bladegen and 3D overall stage performance will be conducted to finalize the design by using ANSYS TurboGrid and ANSYS CFX software. The design process for the baseline case is shown in Figure 3.5.

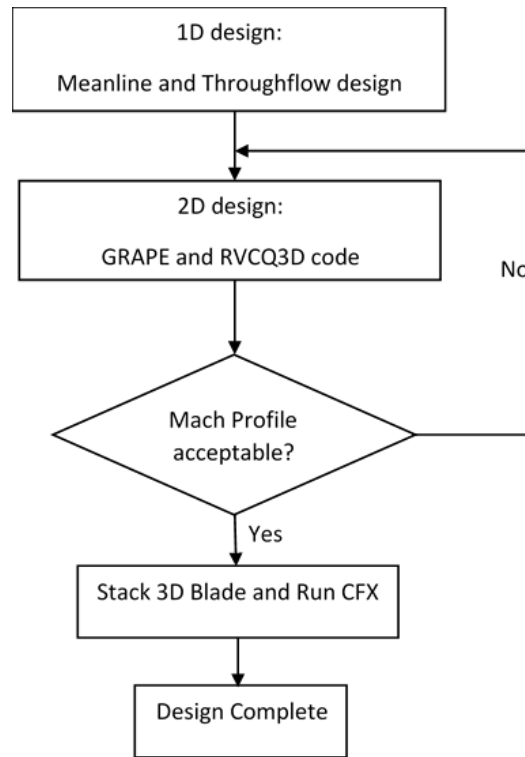


*Figure 3.5* Baseline Design Flowchart

As for the Hybrid Vortex case, the design process is similar to the baseline case. Isentropic Mach profiles will be verified and kept in line with the baseline case for each airfoil section in order to isolate the effect of the new method. It is essential to check the axial velocity profile from the CFX results to eliminate potential errors using inaccurate input. The design process for the Hybrid Vortex case is shown in Figure 3.6. The Hybrid Vortex Solution is derived from an actual axial velocity profile after an inlet guide vane generated from 3D CFD analysis, as discussed in the section 3.1. The annulus boundary condition was taken into account at the early stage of preliminary design, which is closer

to mimicking real operating conditions. This procedure takes less efforts during the iteration process.

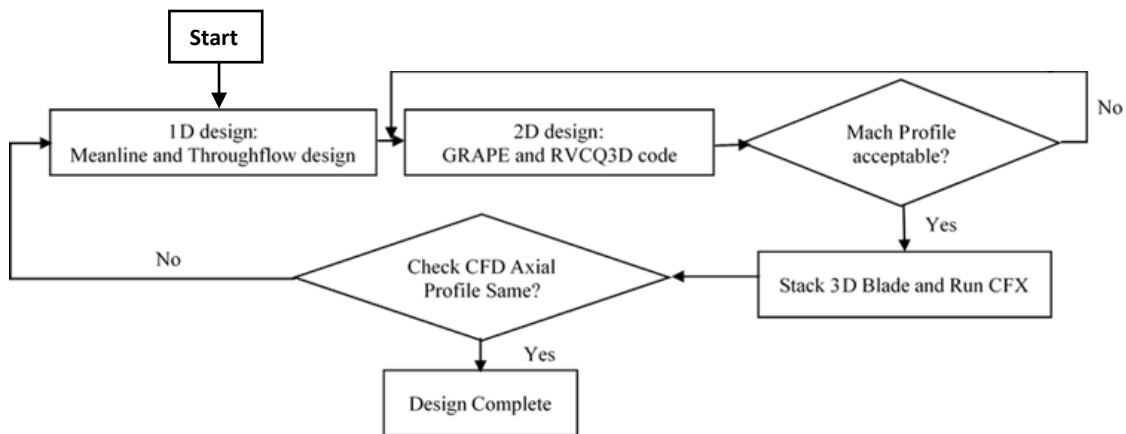


Figure 3.6 Hybrid Vortex Design Flowchart

## 4. Blade Design and Methodology

### 4.1.1D Design

A low hub-to-tip ratio was selected for the design to fully examine the impact of the new method with differently staggered sections. The main design parameters are summarized in Table 4.1 below.

Table 4.1

*Mid-Section Design Values*

Variable		Value
Mass Flow	$\dot{m}$	80 kg/s
Total Pressure Ratio	$\pi_0$	1.3
Hub-to-Tip Ratio	H/T	0.4
Rotational Speed	RPM	6,100
Absolute Mach Number at LE	$M_{LE}$	0.38
Total Pressure at LE	$P_{O,LE}$	101,005 Pa
Total Temperature at LE	$T_{O,TE}$	298.49 K
Absolute Inlet Flow Angle	$\alpha_{LE}$	13°
Number of Blades	NOB	20

#### 4.1.1. Baseline Design Choice

The first task is to construct a baseline case to act as a benchmark. After initial and 1D design choices were decided, the same aerodynamic, thermodynamic and geometric properties at the mid were maintained for all existing vortex solutions. Using radial equilibrium equation 3.4 to complete the velocity triangles from hub to tip. *Figure*

4.1 to Figure 4.4 show spanwise angle distributions with a mid-reaction of 0.638 for Constant Reaction, Forced Vortex, Free Vortex and Exponential Vortex cases. The shadowed range in the figures highlights the difference between LE and TE beta angle. These results are consistent with plots generated by Horlock (Horlock, 1958), sharing the same trends.

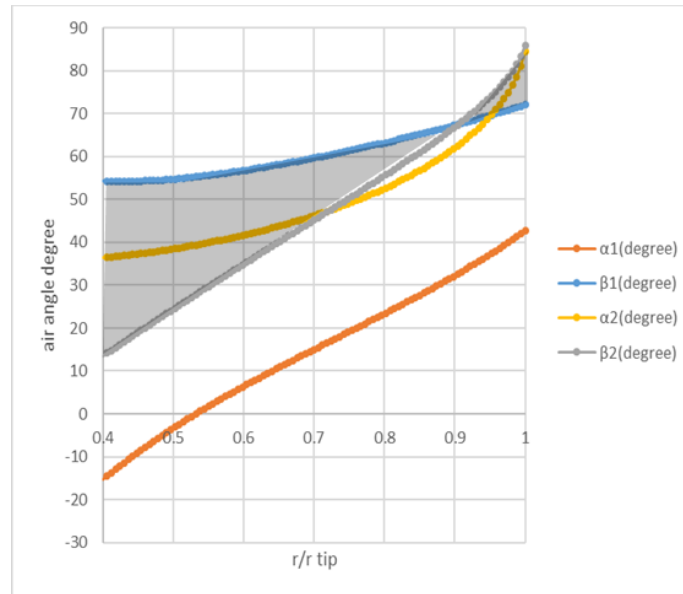


Figure 4.1 Constant Reaction 1D Design Angle Distribution

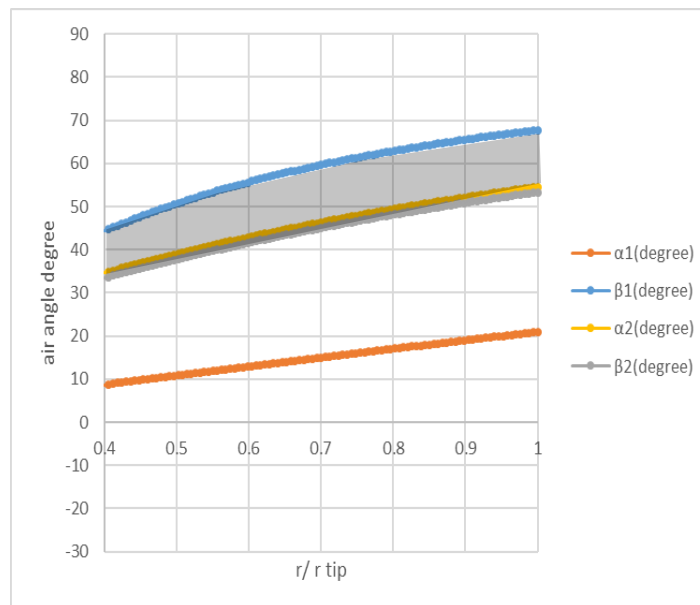


Figure 4.2 Forced Vortex 1D Design Angle Distribution

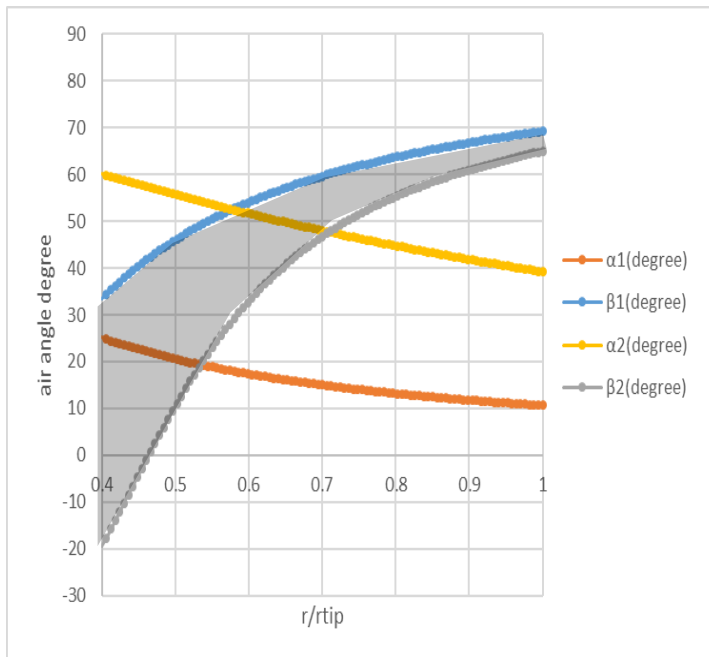


Figure 4.3 Free Vortex 1D Design Angle Distribution

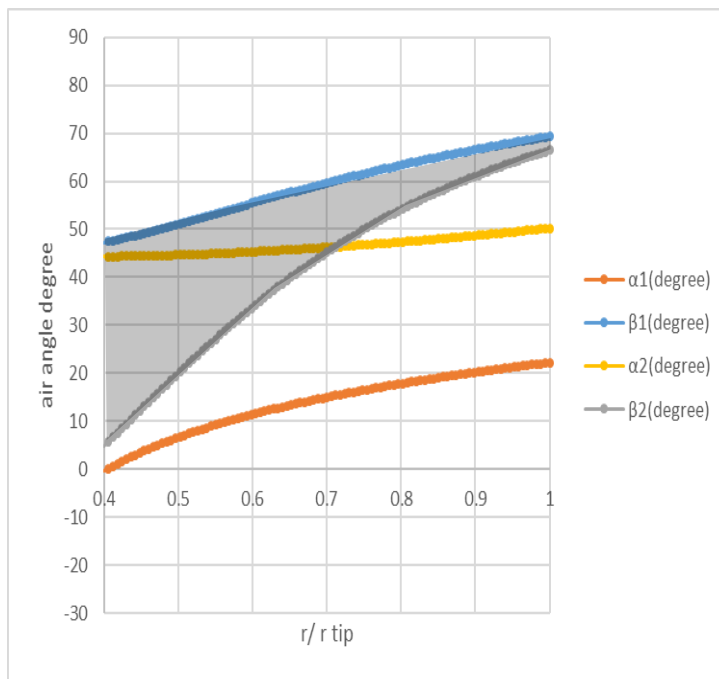


Figure 4.4 Exponential 1D Design Angle Distribution

As is shown in *Figure 4.1*, at the same mid-reaction condition, the Constant Reaction solution has a crossed beta distribution, which causes the blade section to alter

its curvature. This design should be avoided. The forced Vortex solution, *Figure 4.2*, seems to have the same amount of beta variation from hub to tip, which is undesired because the wheel speed is much larger at the tip than at the hub. Therefore, the blade loading is likely to vary widely and flow at the tip is more likely to separate. From analytical reasoning, blade turning, or net deflection, at the hub should be larger than at the tip. Hence, Forced Vortex should be avoided as well.

*Figure 4.3* and *Figure 4.4* show the Free Vortex and the Exponential Vortex angle distributions, with no doubt that they are superior designs compared with the previous two cases. The Free Vortex solution at the hub has a  $\Delta\beta$  of over 50 degrees, while  $\Delta\beta$  for the Exponential solution at the hub is around 40 degrees, which indicates that the Exponential solution hub is working at a reduced loading. However, with respect to efficiency and convenience, the Exponential Vortex design procedure is much more complicated than the Free Vortex. It requires two different axial velocity profiles at LE and TE. Furthermore, each equation has three unknown constants to resolve, which makes the Exponential solution less suitable for a highly iterative design process. Hence, the Free Vortex solution has been chosen as the baseline case.

#### **4.1.2. Hybrid Vortex Design Cases**

In order to determinate the best way to investigate the new hybrid vortex solution, three cases have been studied in this thesis. All three cases shared the same methodology but had slight differences in the leading edge design. As for the trailing edge, attempts to express the velocity profile using the same method have been made. However, after comparing the results with the free vortex solution at the TE, it was decided that keeping the Free Vortex method was acceptable.

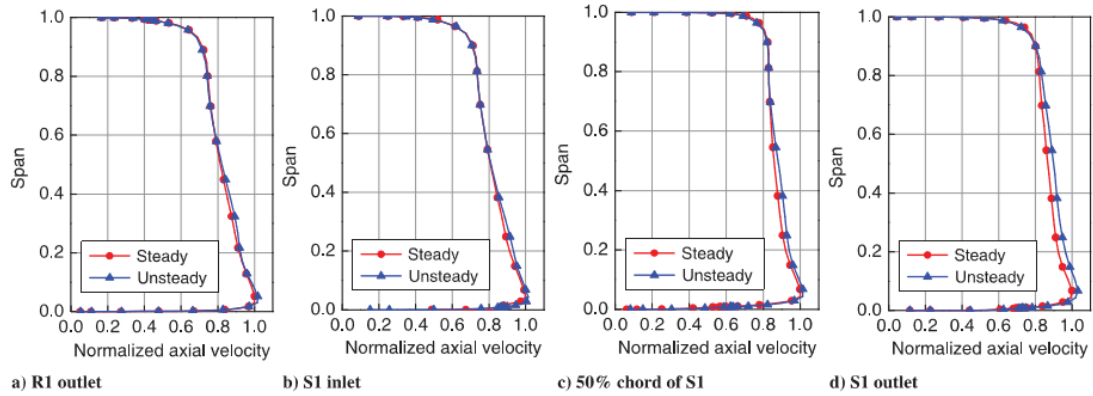


*Figure 4.5* Circumferential Mass Flow Averaged Axial Velocity Profiles for R1 and S1 Using Steady and Unsteady Simulations (Zheng, 2017)

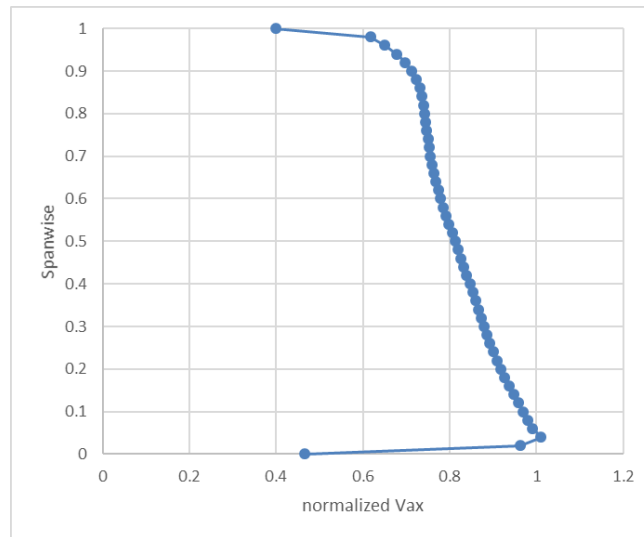
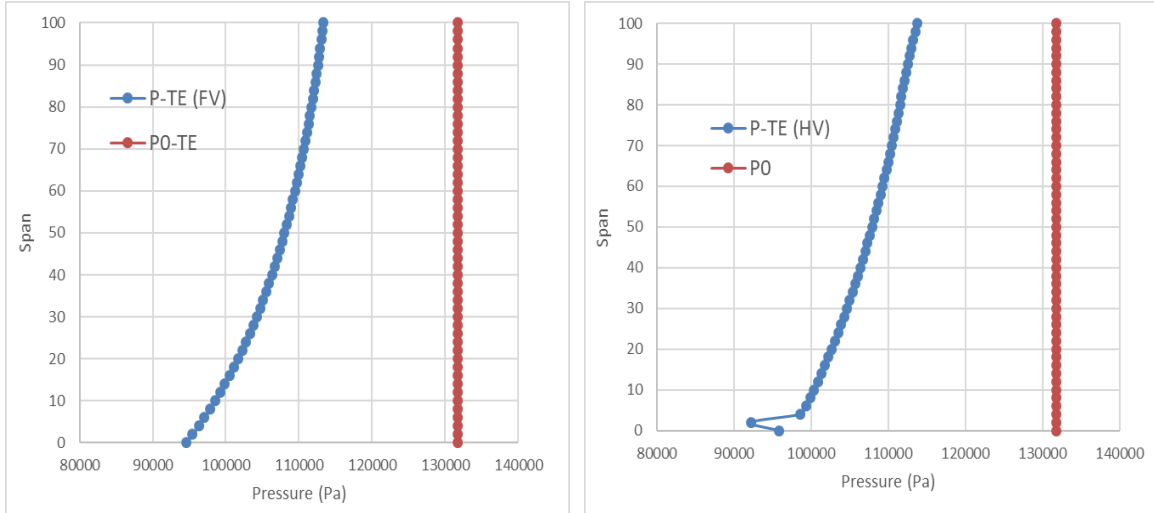


*Figure 4.6* Fitting Curve for Axial Velocity Profile of The First Rotor Outlet

A curve fit was applied to the result of the trailing edge design as well. Zheng and Yang studied the end-wall boundary layer and introduced blockages for multistage axial compressors. (Zheng, 2017) According to their study, the normalized axial velocity profiles of the first rotor and the first stator are shown in *Figure 4.5*. The profile for the first rotor outlet has been selected for the investigation. *Figure 4.6* is the corresponding matching curve plotted by the same method mentioned in section 3.2.





(a)

(b)

Figure 4.7 Trailing Edge Pressure Profile Comparison between The Free Vortex Solution (a) and The Hybrid Vortex Solution (b)

In Figure 4.7, the result shares the same trend with the free vortex solution.

Therefore, the characteristics of the Hybrid Vortex solution at the TE can be represented by the Free Vortex solution. The new design method was the combination of the Hybrid Vortex solution at the LE and the Free Vortex solution at the TE. The details are summarized in Table 4.2 and will be discussed in the following paragraphs.

Table 4.2

*Hybrid Vortex Solution Design Cases – LE Distribution*

Case	Axial Velocity	Circumferential Velocity
A	HV method: profile after IGV	HV method: equation 3.6
B	HV method: profile after IGV	HV method: equation 3.3
C	HV method: profile from CFX	HV method: equation 3.3

**Case #A**

The first case applied equation 3.5 and equation 3.6 to build the axial and circumferential velocity profiles. They were derived originally from equation 3.3 with the assumptions of incompressible flow, and that the total pressure, stagnation enthalpy and entropy do not vary with radius. Those assumptions might affect the results and deliver unrealistic alpha and circumferential velocity distributions as will be discussed later. This leads to case B, which is an improvement over case A.

**Case #B**

Instead of deriving the circumferential velocity from the axial velocity distribution (equation 3.5), case B applied equation 3.5 and the alpha profile from the baseline to complete the velocity triangles at the leading edge.

**Case #C**

It was discovered that the axial velocity profile generated from CFX results was not the same as what was used for the hybrid vortex cases A and B. One iteration of the design process was necessary to ensure the axial velocity profile was properly imported into the new design methodology. Therefore, case C uses the axial velocity profile from the CFX result of case B.

**Leading Edge Treatment**

Velocity triangles comparison among the free vortex case, the hybrid vortex cases A and B at the LE at 2%, 50%, and 98% span locations are given. A closer look shows that, in *Figure 4.8*, the three velocity triangles overlap at the 50 % span location. This indicates that the 3 cases have identical mid conditions for the 1D design. It was guaranteed that the velocity triangle differences among the three cases were caused by

the different vortex solution treatments.

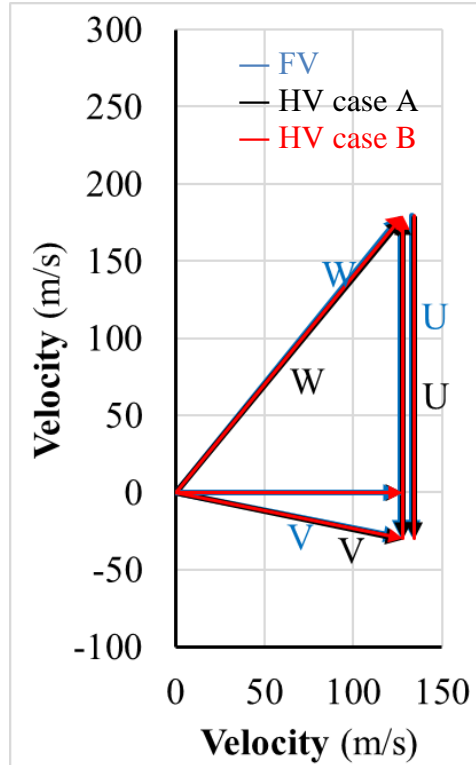


Figure 4.8 LE Velocity triangle comparison at 50%

It is obvious that case B has the largest beta angle at LE hub and tip as shown in Figure 4.9. By introducing the axial velocity profile after the IGV and maintaining the same mid conditions for all cases, the free vortex case (“FV”) has a larger beta but also a smaller alpha at the LE hub section than the hybrid vortex (“HV”) case A. While the HV case A has nearly the same beta angle at the LE tip section, but a larger alpha angle than the FV case as shown below. It is evident that the HV case A had no improvement in beta distribution compared with the FV case, because of the larger alpha. But it can be said that the HV case A has the potential to have larger surge margin if the change of alpha profile can be isolated, because the beta profile is more aligned with the flow.

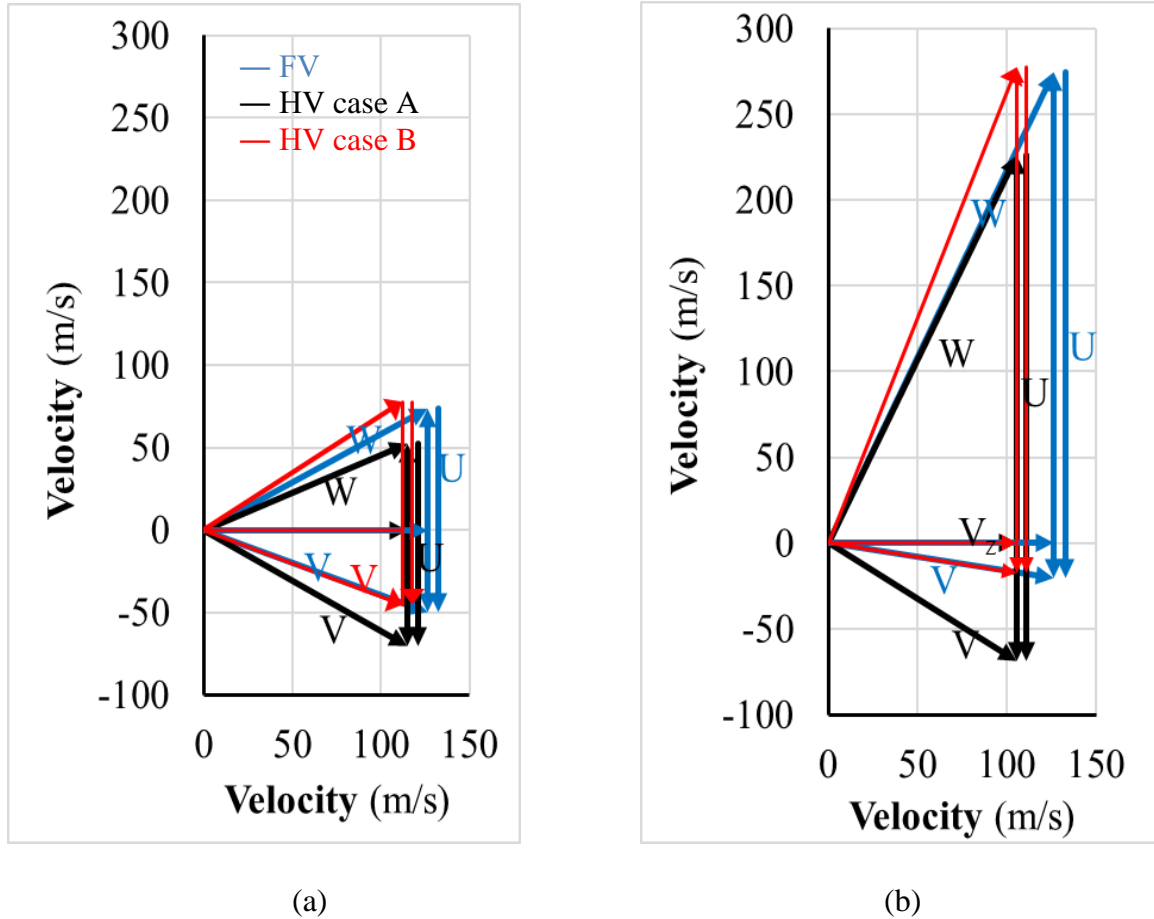


Figure 4.9 LE Velocity Triangle Comparison at (a) 2% Span Location and (b) 98% Span Location

An understanding of the mechanism of the IGV is crucial to investigating what caused the differences among the three cases shown above. IGVs can be considered as convergent channels formed by blades that accelerate the flow. They are used to generate inlet swirl and reestablish optimum incidence for the rotor. It is common to design an IGV that delivers a positive pre-swirl to maintain optimum incidence at reduced mass flow. Moreover, mass flow is reduced at the hub and tip because of the blockage near the wall. So, the off-design absolute angle at hub and tip is larger than at the mid. However, the IGV and rotor use different methods to deal with stall. The rotor, when it is designed

with negative incidence, will have better operation near stall.

By introducing a real normalized  $V_{ax}$  profile after the IGV into the hybrid vortex design, the circumferential velocity distribution and alpha profile at the leading edge can be determined. Moreover, the hybrid vortex solution LE alpha profile inherits the same tendency as the IGV exit profile (the off-design alpha angle at the hub and tip is larger than at the mid). However, this method also introduced an unrealistic alpha profile for the compressor rotor and swirl was introduced even though the mid radius absolute angle was zero.

Therefore, a modification has been made for the hybrid vortex case B, which provides a better option by decoupling the axial velocity profile from the alpha profile. It has the advantage of incorporating the actual  $V_{ax}$  distribution after the IGV, and prevents the alpha profile from being unrealistically altered. As presented in *Figure 4.9*, the HV case B has the same alpha profile as the FV case and a bigger beta profile than the FV case. The methodology used for the hybrid vortex case B was employed for the final leading edge treatment.

## Trailing Edge Treatment

The trailing edge was designed by using the free vortex method as discussed in section 4.1.2. However, after closely investigating the pressure profile at the TE, an undesired adverse pressure distribution was observed near the hub section, as shown in *Figure 4.11(a)*. As mentioned in chapter 3, the purpose of the vortex solution is to impose a force due to a pressure gradient from hub to tip to balance the centrifugal force caused by the rotation. Therefore, a positive pressure gradient is demanded for design purposes. Even though there was a better positive pressure gradient in *Figure 4.11(a)* than in *Figure 4.11(b)*, the hub section was showing expansion instead of compression. Hence, the hub section needed additional modification. By maintaining the same amount of  $\Delta h_o$ , total temperature ratio and total pressure ratio, the total pressure distribution at the trailing edge can be manipulated by changing alpha at the trailing edge. The final pressure distribution for the hybrid vortex case B is shown in *Figure 4.10(b)*.

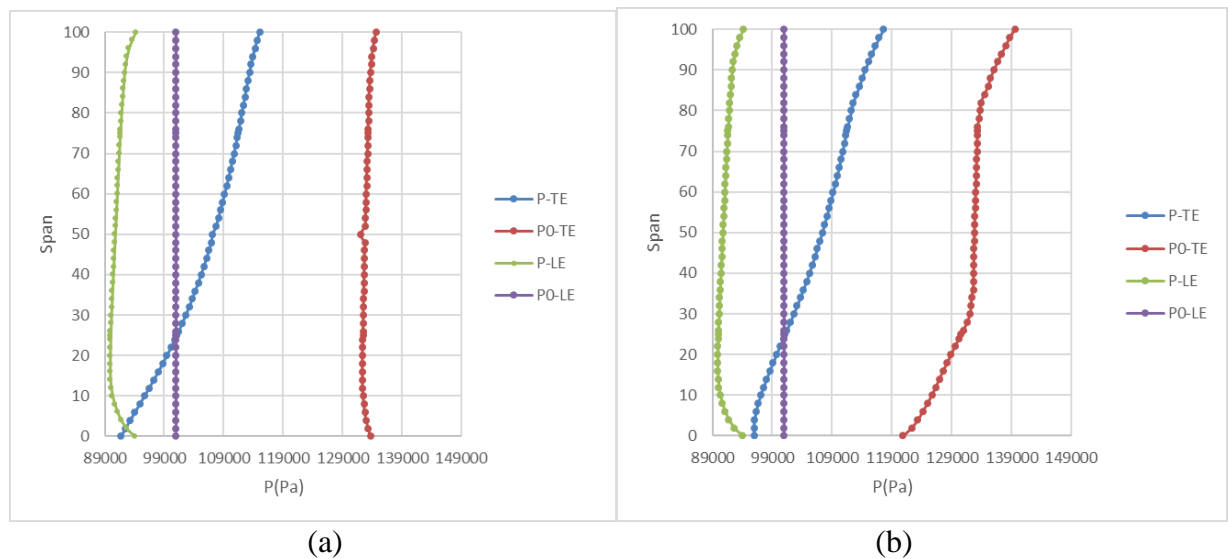


*Figure 4.10* Pressure Distribution at the Trailing Edge for case B without modification (a) and With “tip-strong” modification (b)

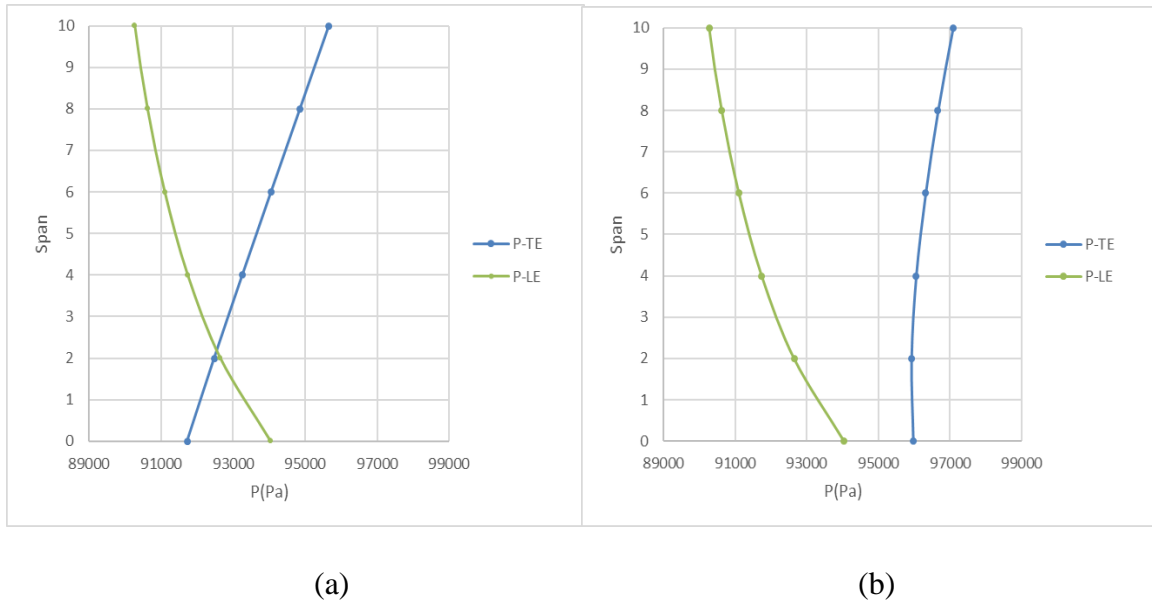


*Figure 4.11* Pressure Distribution at the Trailing Edge Hub for case B without modification (a) and with “tip-strong” modification (b)

#### 4.1.3. Meanline and Throughflow

The computational code CSPAN (Arthur, 1995) and ACD (Crouse, 1981) were used to perform meanline and throughflow analysis. CSPAN provides conceptual sizing analysis and determines the flowpath given certain input parameters for axial compressors. The result is shown in *Figure 4.12*.

Code ACD delivers streamline analysis, it can produce thermodynamic and aerodynamic analysis, and has the capability for designing and stacking the blade elements. However, the limitations of CSPAN and ACD were evident. It did provide reliable flowpath parameters and streamline analysis, but the corresponding blade elements (stream sections) were impractical. The solidity of the blade at the hub section was 1.4 in the 1D analysis compared with 2.52 delivered by the ACD code. The result is shown below. The blade geometry will be corrected and studied in the next stage of design.

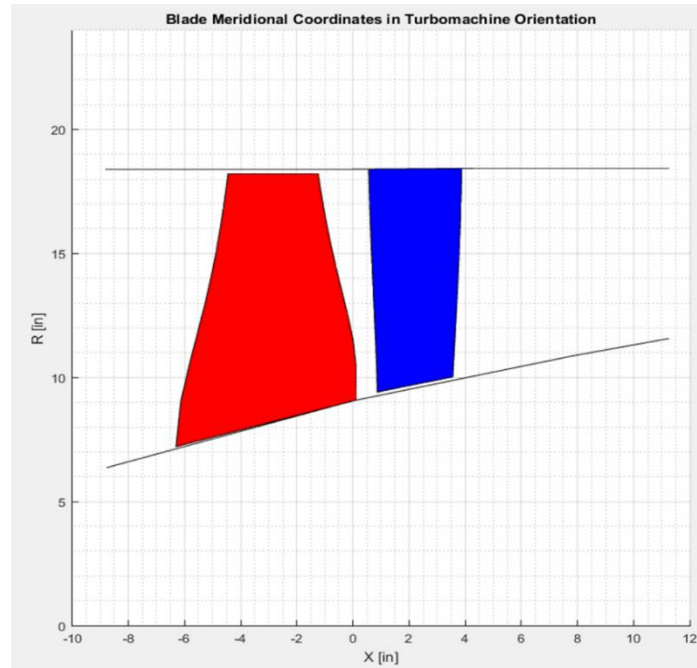


Figure 4.12 CSPAN code flowpath result

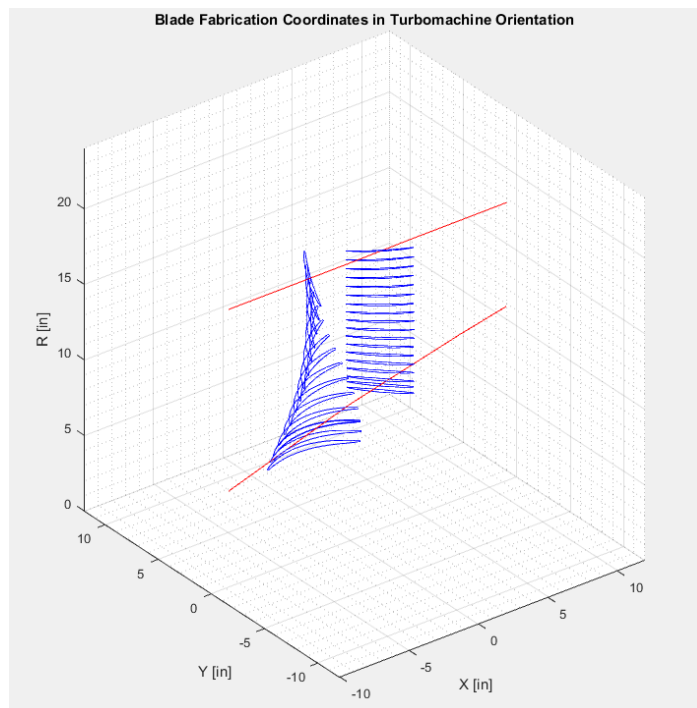


Figure 4.13 ACD 3D Blade Elements Stacking



## **4.2.2D Design and CFD**

The streamline analysis from the throughflow code was used in 2D CFD section design and the computed streamtube contraction used as one of the inputs for the Quasi 3D Viscous solver Code. The 2D blade design and aerodynamic analysis were performed at five different span locations 3%, 35%, 61%, 82% and 98%.

The GRAPE code (Grids about Airfoils using Poisson's Equation) is an elliptic grid generator to produce C-type grids and is able to give good resolution of the blade leading edge and wakes. (Chima, 1999) It works directly with RVCQ3D code. RVCQ3D (Rotor Viscous Code Quasi-3-D) is a rapid computer program for quasi-three-dimensional viscous flow analysis in turbomachinery. (Chima, 1999) This code uses an explicit finite-difference technique to solve thin-layer Navier-Stokes equations on blade-to-blade surfaces. NASA's grid generating code, GRAPE, and Quasi 3D Viscous solver Code, RVCQ3D were used for assessing the isentropic Mach profile for the stream sections. The blade shape design, which was conducted using ANSYS BladeGen, has been modified to deliver the desired Mach profiles and ensure a smooth 3D blade surface. The shape of the Mach profiles for the free vortex and hybrid vortex blades were kept identical in order to isolate the effect of the new design approach. Examples of inputs for the two programs are given in Appendix "C" and "D".

### **4.2.1. 2D Meshing and Sensitivity Studies**

Mesh sensitivity analysis was performed for the GRAPE code in order to eliminate numerical variation due to mesh size. The mesh size was varied from 6000 to 21000 nodes. An appropriate mesh size is desired to balance numerical accuracy with computational resources. Table 4.3 is a summary of the tested sizes and the selected mesh

size is highlighted.

Table 4.3

2D Mesh Sensitivity study total nodes count.

Total Nodes		k		
		60	45	30
j	350	21000	15750	10500
	300	18000	13500	9000
	250	15000	11250	7500
	200	12000	9000	6000

Figure 4.14 Mesh Sensitivity Analysis for Baseline at 3% Location (a) and Enlarged View (b) presents the pressure surface Mach number distribution for the baseline case at 3% span location. As is shown, mesh independence was achieved when the mesh size was over 10000 nodes.

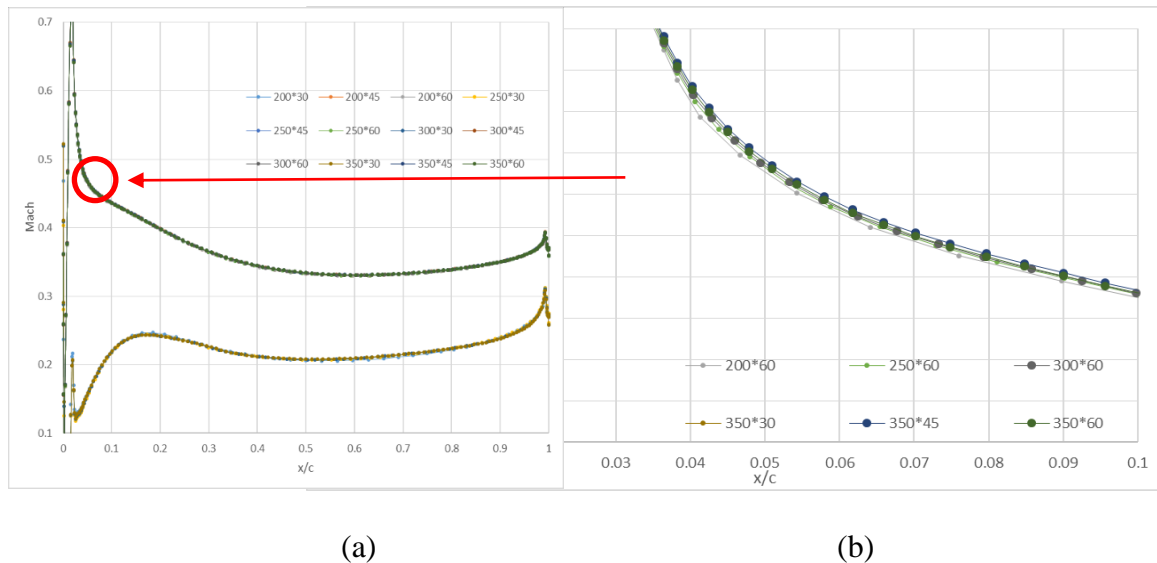
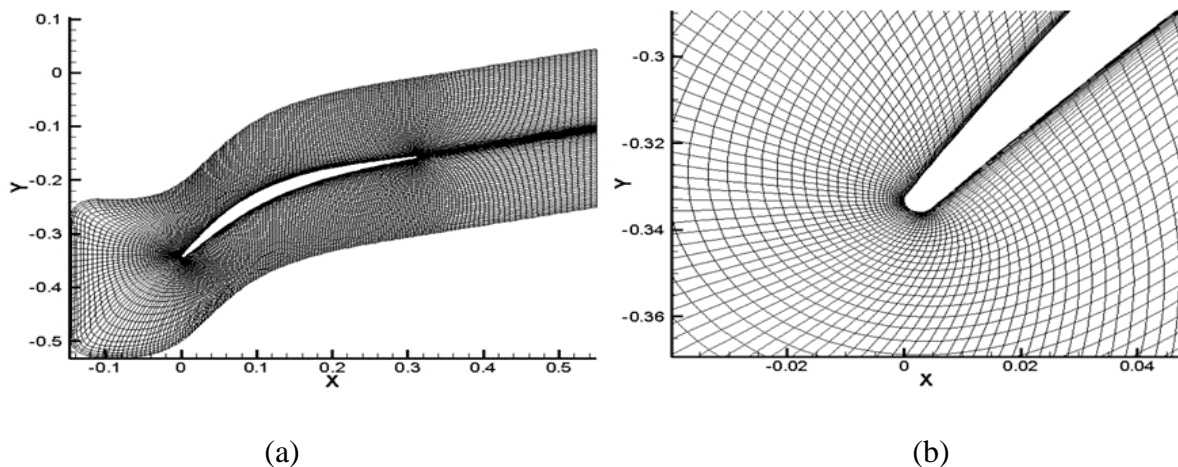
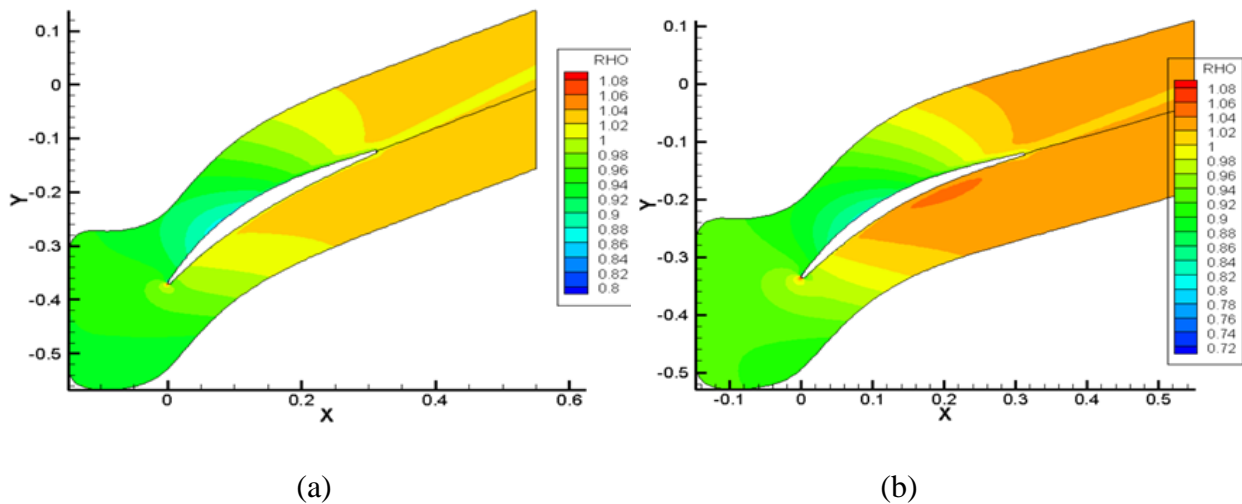


Figure 4.14 Mesh Sensitivity Analysis for Baseline at 3% Location (a) and Enlarged View (b)

A sample of the computational grid, enlarged view of the leading edge region, density contours, and the corresponding Mach profile for the 35% span location, are given in *Figure 4.15* to *Figure 4.17* below.



*Figure 4.15* Hybrid Vortex Case Grid Sample of LE at 35 % Span (a) and LE Enlarged View at 35 % Span (b)



*Figure 4.16* Density Contour at 35 % Span for Free Vortex Case(a) and Hybrid Vortex Case (b)

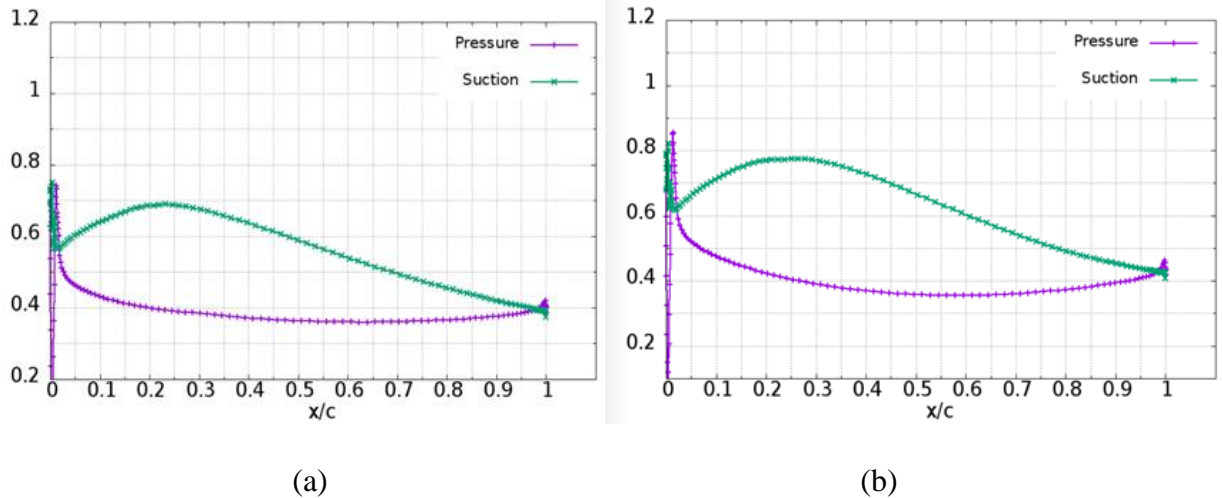


Figure 4.17 Mach Profile at 35 % Span for Free Vortex Case (a) and Hybrid Vortex Case (b)

#### 4.3.3D Design and CFD

The software ANSYS BladeGen, TurboGrid, and CFX were used to complete the three-dimensional design of the blades. ANSYS BladeGen is a geometry creation tool that is customized for turbomachinery blades. The preliminary airfoil and stream section shapes were initialized in BladeGen and refined using the NASA 2D analysis described earlier. Five span sections were stacked on the centroid to generate the 3D blade geometry using ANSYS BladeGen. ANSYS TurboGrid is a meshing tool that is specialized for CFD analysis of turbomachinery blade rows. ANSYS CFX is composed of two parts: CFX-Pre is for preprocessing and simulation set up and CFX-Post is for postprocessing simulation results (ANSYS, 2013).

### 4.3.1. 3D Meshing and Sensitivity Studies

ANSYS TurboGrid uses ATM Optimized topology, which can automatically select the appropriate topology based on the blade type and blade angles. Hexahedral meshes were utilized to resolve boundary layer regions and tip gap. It is critical that the boundary layer is well captured in order to predict stall. *Figure 4.18* is a topology example; the master topology is shown with thick lines, while the refined mesh is shown with fine lines. Five topology layers were produced at 3%, 35%, 61%, 82% and 98% span locations to capture the 3D features of the airfoil and improve mesh quality. A constant tip gap of 0.5% was selected for mesh generation. An example of tip gap meshing is presented in *Figure 4.20* (b).

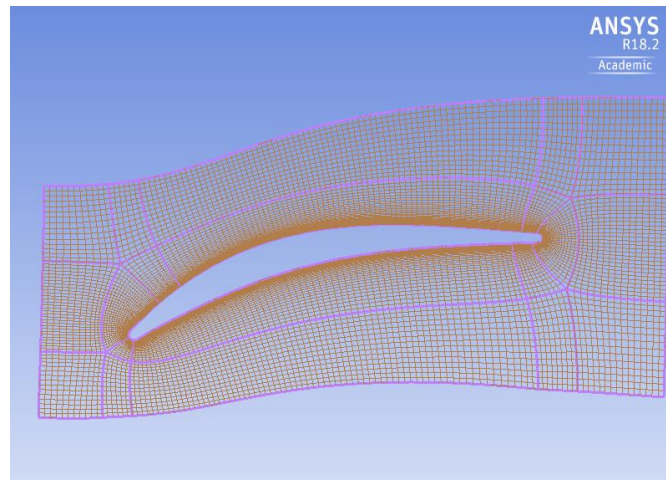


*Figure 4.18* Topology Example

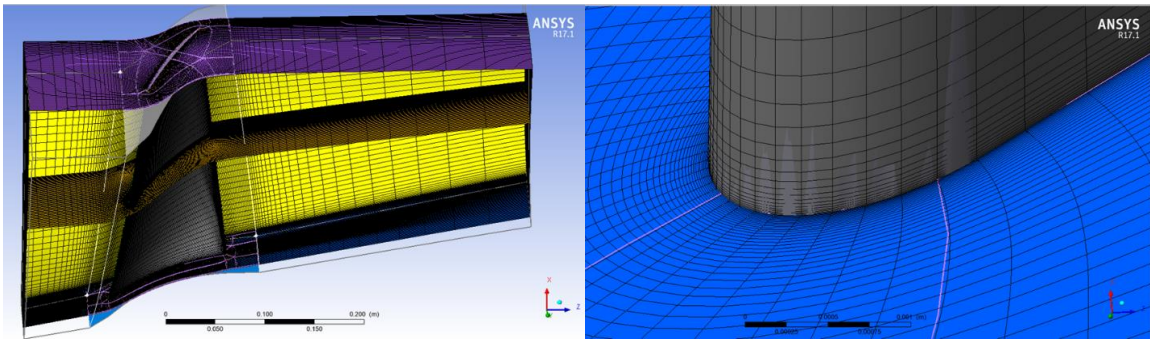
Table 4.4 shows mesh statistics for the baseline case rotor. According to Cornelius (Cornelius, 2014), typical mesh size per blade passage is one million cells and the near wall spacing  $y^+$  should be below 2. However, after conducting mesh sensitivity analysis, it was discovered that a medium mesh was good enough for CFX simulations.

Table 4.4

*2D Mesh Size and Parameters for Baseline Case.*

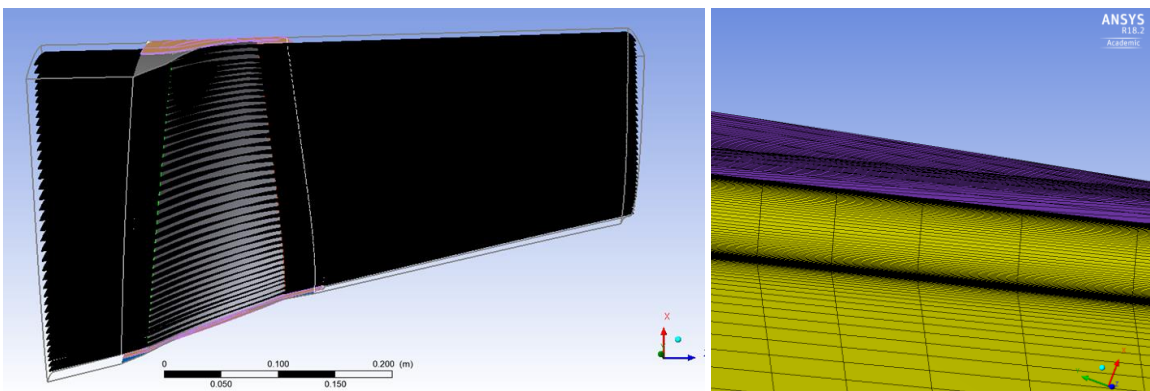
Rotor	Course Mesh	Medium Mesh	Fine Mesh
Cells	1.0M	2.5M	5.0M
Target Y+	$\leq 10$	$\leq 5$	$\leq 2$

33 mesh planes were built across the whole domain from inlet to outlet in order to well capture the blade twist, which is demonstrated in *Figure 4.20* (a). The final Domain Mesh is shown in *Figure 4.19* (a) with the leading edge refined view presented in *Figure 4.19* (b).



(a)

(b)

*Figure 4.19* Final Domain Mesh (a) and LE Enlargement View (b)

(a)

(b)

*Figure 4.20* Final Domain Mesh with Mesh Planes (a) and Tip Gap Enlargement (b)

### 4.3.2. Simulation Setup

ANSYS CFX was used for this analysis, it has the capability to achieve reliable and accurate solutions quickly and robustly.

#### Boundary Conditions

The boundary conditions for the simulations were taken from the previous stage of design. Steady state has been chosen for the simulation type. Total pressure and total temperature profiles at inlet were specified, as well as mass flow rate at outlet, which is a more stable method to run the simulations than other boundary controls, especially near the stall points. By conducting simulations at different mass flow rate and RPM, off-design operations can be examined, and the compressor map can be generated.

In addition to the inlet conditions, an inlet initialized velocity profile was imported into the simulations to assume same rotor inlet conditions from the inlet guide vane were achieved for all four cases. The initialized profile is shown in Appendix “E”.

#### Turbulence Model

There are several turbulence models available to complete the simulation setup. However, most standard two-equation turbulence model fails to predict the proper amount of flow separation under adverse pressure gradient (ANSYS, 2013).  $\epsilon$ - equation turbulence model tends to have overly optimistic prediction performance characteristics and delay the prediction of stall.  $k - \epsilon$  model is an improvement but still has the same tendency according to Cornelius (Cornelius,2014). Cornelius further mentioned Shear Stress Transport (SST) with the Reattachment Model (RM) can better predict the stall than applying Shear Stress Transport (SST) turbulence model alone.

A sensitivity study was performed between the SST model and SST with RM

model. However, as shown in *Figure 4.21*, there was no noticeable difference between the two models for pre-stall prediction. Therefore, the Shear Stress Transport model has been chosen as the turbulence model of all simulations.

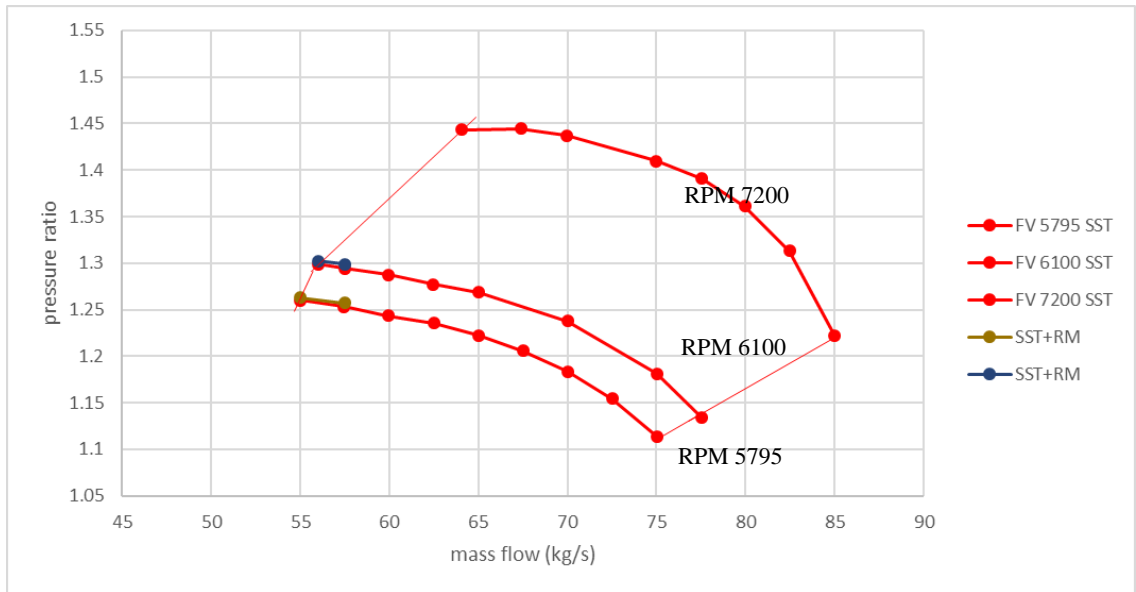


*Figure 4.21* Results for Baseline Case Using SST and SST+RM Comparison

### Convergence Criteria

The residuals were monitored in order to declare convergence has been achieved. RMS (root mean square) residual type has been chosen and its residual level is  $10^{-4}$ , which is a relatively loose convergence, but it is sufficient for these cases. Mass flow variation was also monitored. Convergence was achieved between 1500-2000 iterations, however it tended to take more iterations to converge near the surge line, as shown from *Figure 4.22* to *Figure 4.25*.



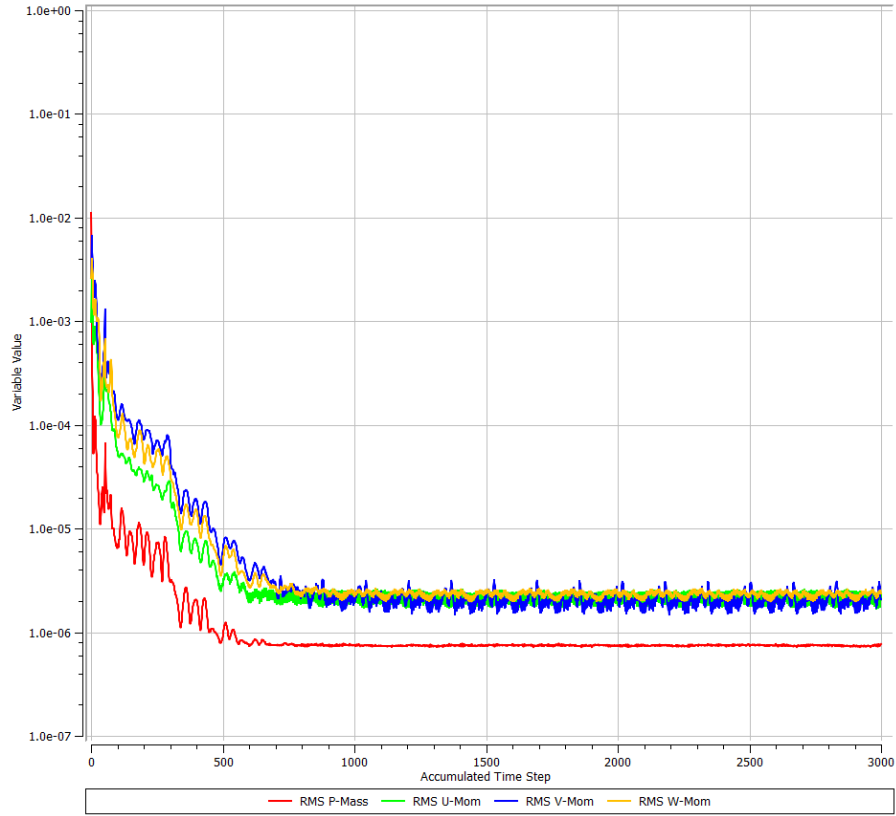


Figure 4.22 RMS Convergence Sample near the Design Point

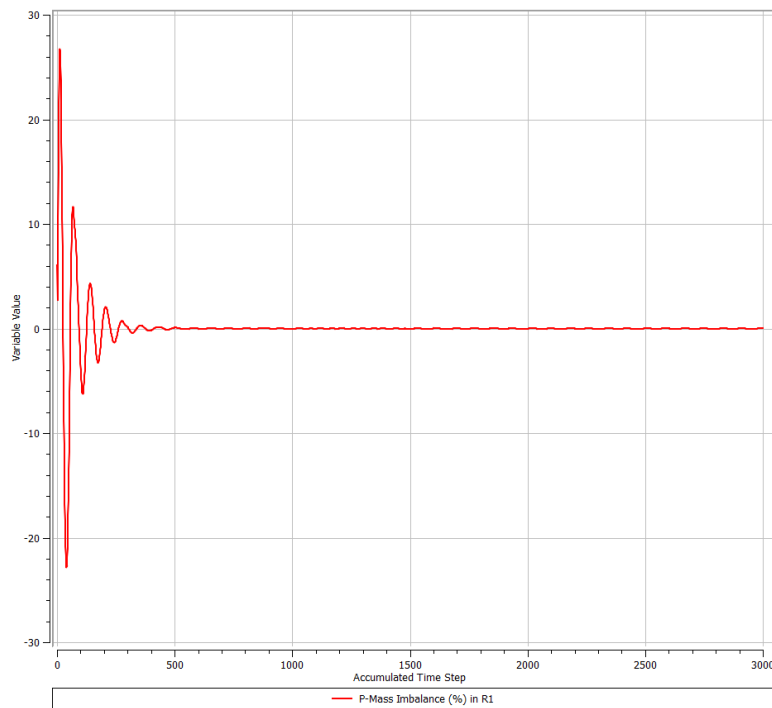


Figure 4.23 Mass Imbalance Convergence Sample near the Design Point

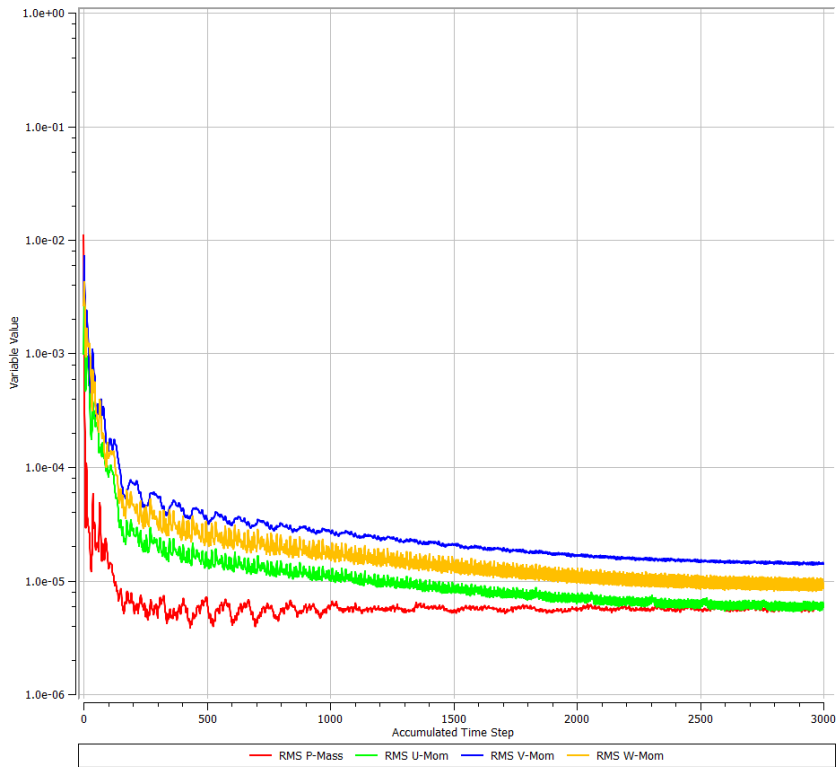


Figure 4.24 RMS Convergence Sample near the Surge Line

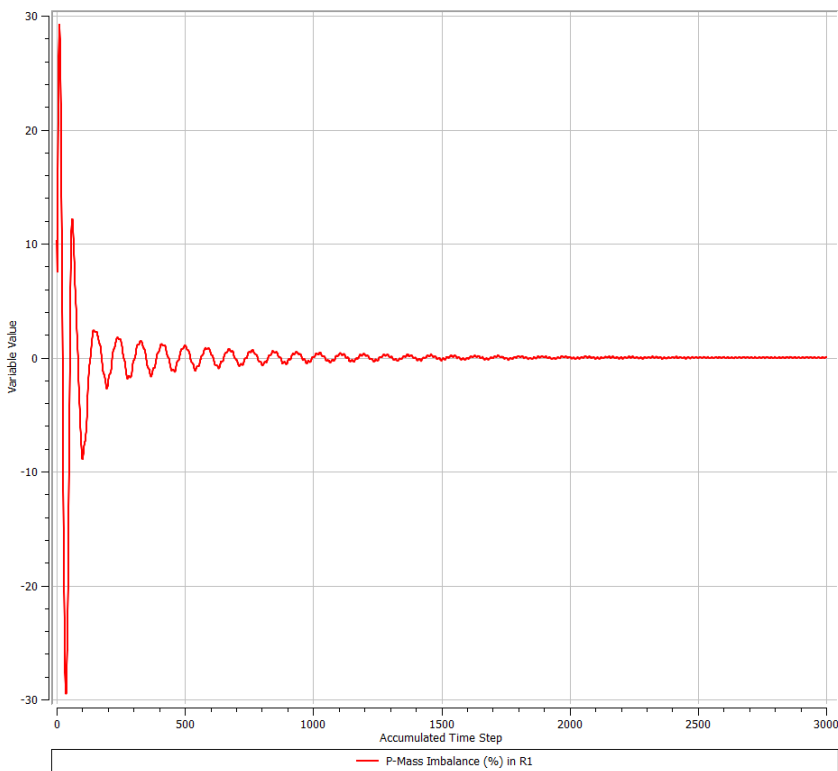


Figure 4.25 Mass Imbalance Convergence Sample near the Surge Line

## 5. Results

### 5.1. Baseline – Free Vortex

As discussed in section 4.1.1, the free vortex solution was chosen as the baseline and a blade has been built as the baseline case.

#### 5.1.1. 1D Design Point

Blade designer's choices have been highlighted in section 4.1. Additionally, there are some other design parameters which are critical and need to be highlighted as well. In the early stage of design, they can evaluate the aerodynamic health of the blade based on comparison with past successful cases and empirical criteria. Those parameters are listed in Table 5.1 below.

Table 5.1

#### *Mid-Section Design Values*

Variable		Value	Criteria
Flow Coefficient	$\varphi$	0.56	0.3 - 0.9
Work Coefficient	$\lambda$	0.52	0.2 - 0.5
Degree of Reaction	Rm	0.6263	N/A
Lieblein's Diffusion Factor	DFm	0.5459	< 0.6
Average Diffusion Factor	DF <sub>avg</sub>	0.4362	≤ 0.45
DeHaller number	DH	0.68	≥ 0.68

In Table 5.1, all the design parameters are within the acceptable range except work coefficient. Work coefficient represents how much work is added compared with the wheel kinetic energy, which is an alternative way to express a stage characteristic

similarly like blade tangential Mach number (Mach number for the wheel speed). Higher tangential Mach number, more stage total temperature increase and also higher shock wave loss (Farokhi, 2009). Because the Mach number at the tip in the relative frame of reference is 0.894 for this baseline case, the work coefficient, which is slightly larger than the criteria, seems acceptable.

### 5.1.2. 2D Airfoil Design

The 2D design of the airfoils was performed by using the method discussed in section 4.2. The flow field and Mach profile were examined by specifying the airfoil shape and the flow conditions upstream and downstream of the cascade. This procedure was repeated at five different span locations, which were 3%, 35%, 61%, 82% and 98% span locations.

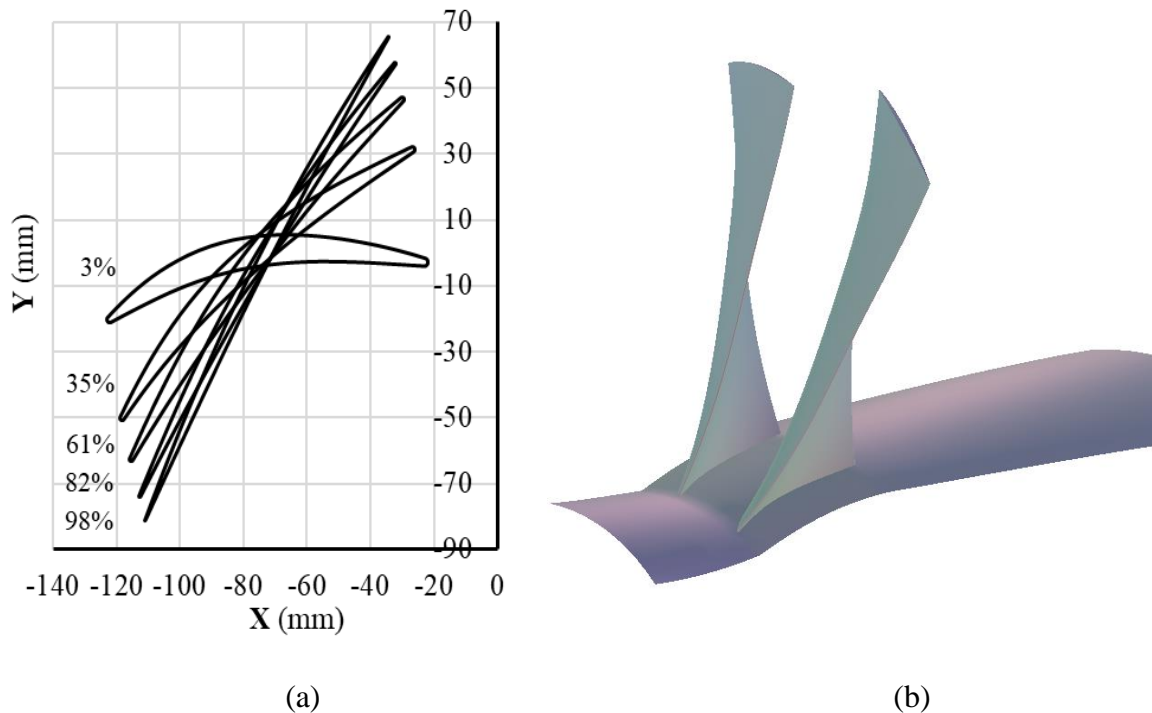


Figure 5.1 Free Vortex Baseline Blade Stacking View

Once the ideal Mach profiles were achieved for all locations, the airfoils were stacked on their centroids in order to form the 3D blade. The stacking view is shown in *Figure 5.1*. 2D Mach profiles for each span locations are presented in Appendix “F”.

### 5.1.3. 3D Performance and Observation

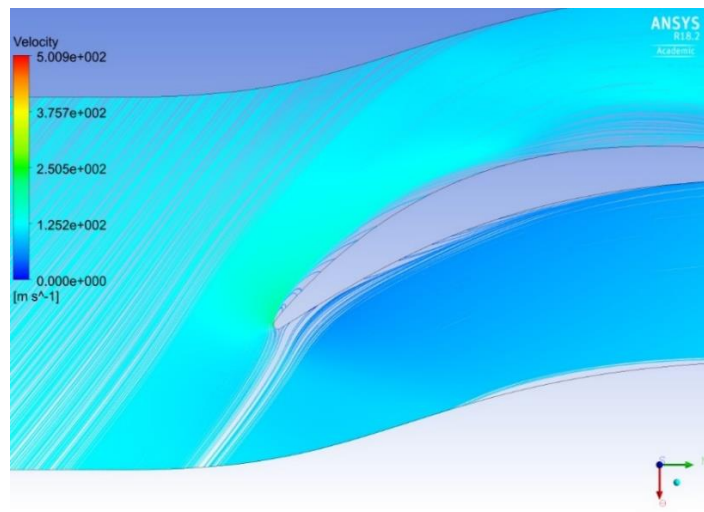
The 3D performance of the baseline case has been examined using the process mentioned in section 4.3. The design point performance is summarized in Table 5.2.

Table 5.2

*Baseline 3D Design Point Parameters*

Variable		Value
Mass Flow Rate	m (kg/s)	57.5015
Pressure Ratio	$\pi_0$	1.2945
Isentropic Efficiency	(%)	93.7871

As is shown in the table above, pressure ratio reached the target at 57.5 kg/s mass flow rate, which is less than what was designed in the 1D analysis (80 kg/s). This is because of the viscous effects and blockage including end-wall blockage.



*Figure 5.2* Free Vortex Baseline 3% Span location Velocity Streamline Plot

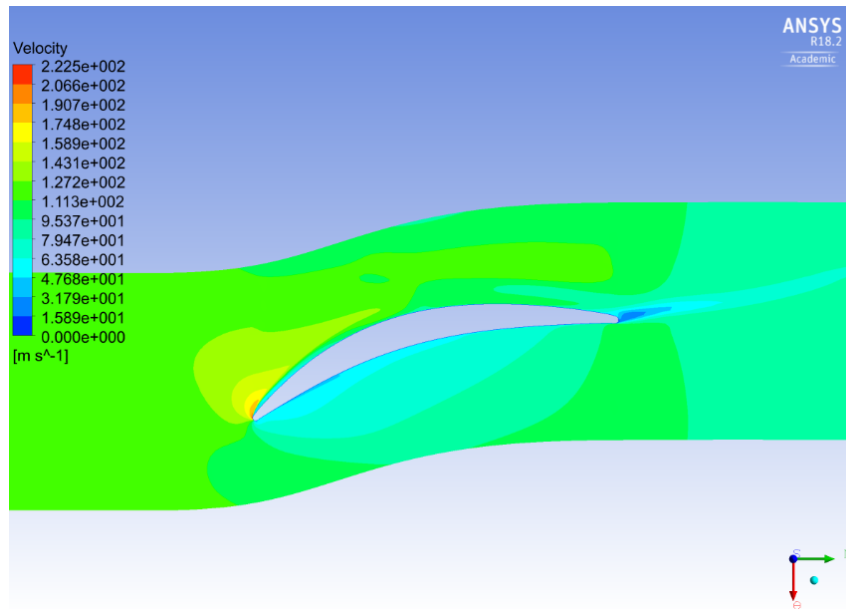


Figure 5.3 Free Vortex Baseline 3% Span location Velocity Contour

Because of the nature of the Free Vortex design, and the constant axial velocity assumption, which doesn't take into account the effect of end-wall blockages, the baseline case behaved poorly as predicted in 3D simulations. It is evident near the hub section as presented above. As shown in *Figure 5.2* velocity streamline plot and *Figure 5.3* velocity contour, the baseline case at 3% span location has a significant positive incidence issue.

Even though it was designed perfectly in 2D CFD analysis, the feedback from 3D CFD varies a lot from the earlier results, which more illustrates the importance of viscous effects and the futility of the uniform axial velocity assumption. The stagnation point was perfectly located on the center of the leading edge which was examined in 2D analysis for the baseline case at 35% span location, as shown in *Figure 4.15 (a)*. However, as presented in *Figure 5.4*, the stagnation point moved considerably from the design intent as shown by the 3D analysis.

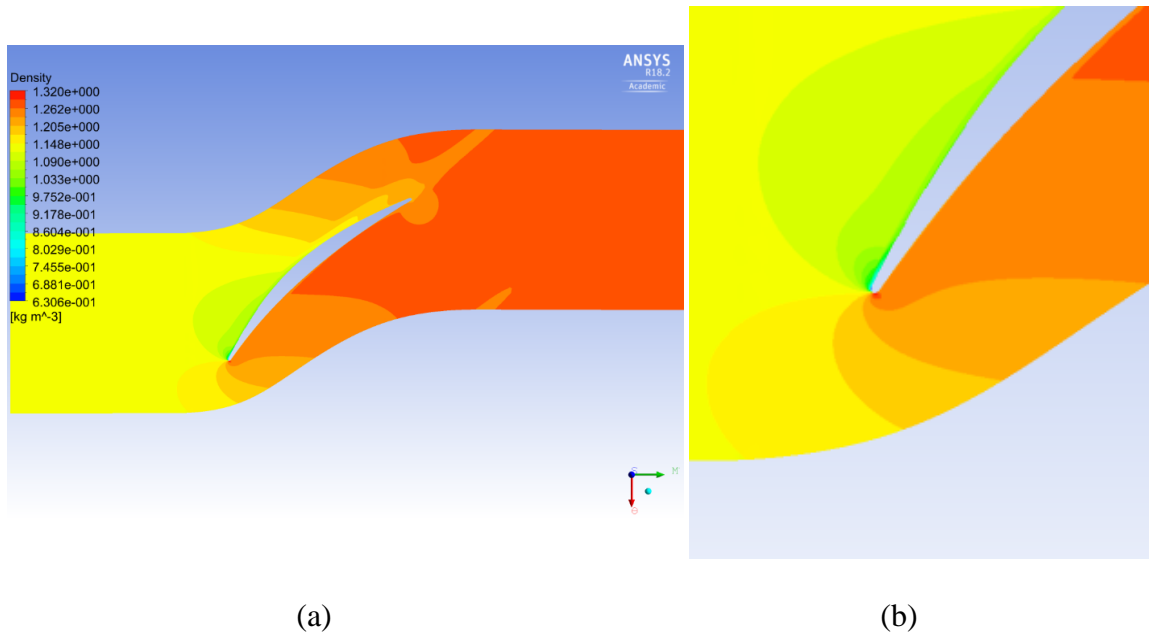


Figure 5.4 Free Vortex Baseline 35% Span location Density Contour (a) and LE Enlarged View(b)

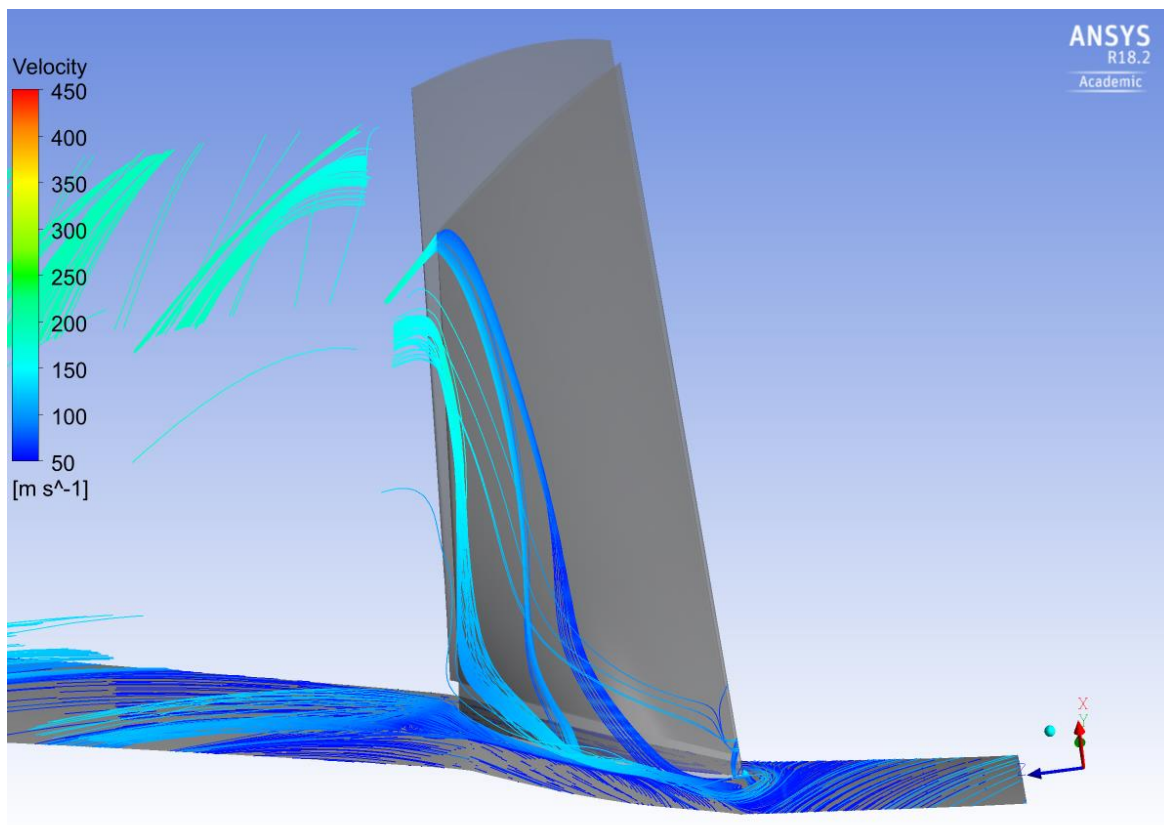
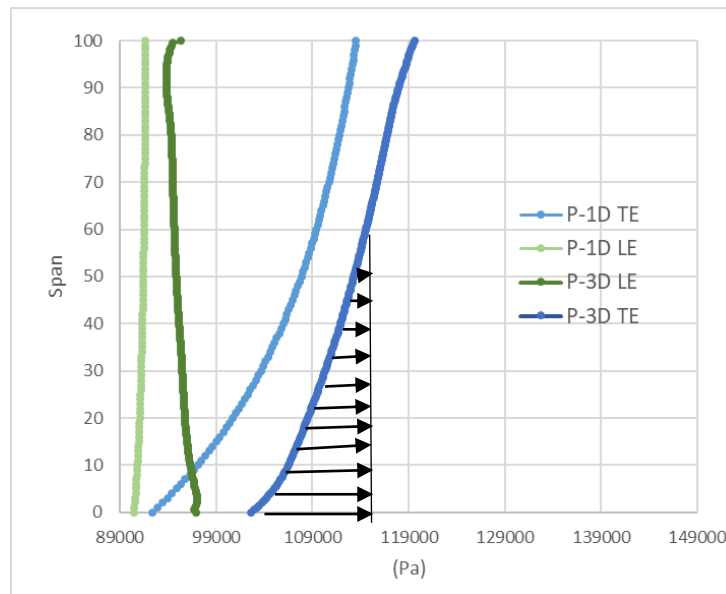


Figure 5.5 Free Vortex Baseline Streamline Plot near Hub (Side View)

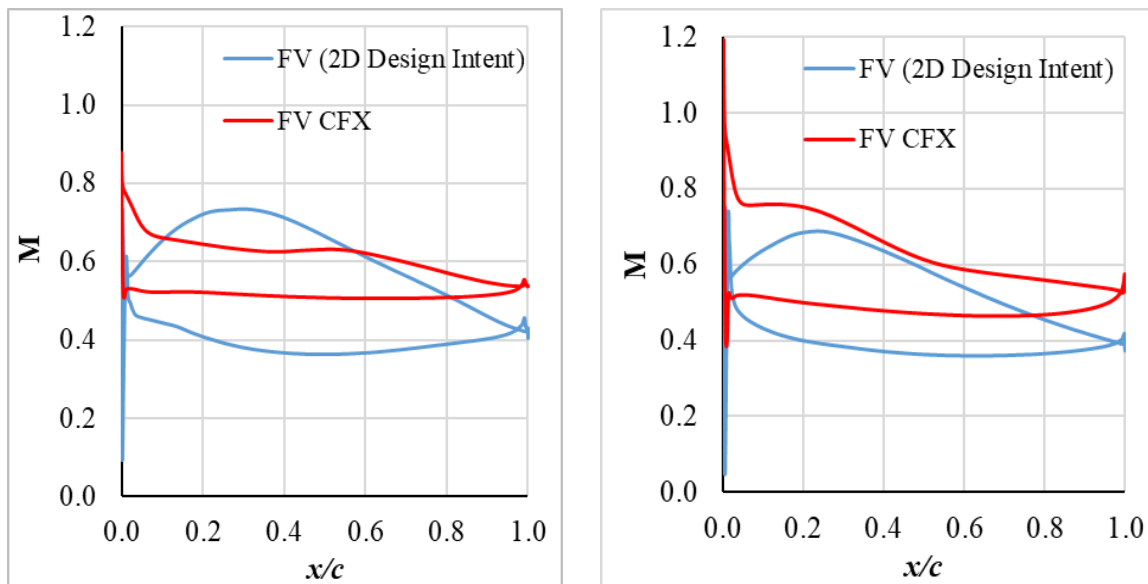
As discussed in section 3.2, the function of the vortex solution is to balance the centrifugal force from hub to tip which is imposed on the flow when the blade is spinning. A closer observation of the flow feature at the hub shows the streamlines on the blade surface were centrifuged from hub to tip and then traveled downstream, which indicates the free vortex solution didn't balance the centrifugal force as demonstrated by *Figure 5.5*.



*Figure 5.6* Static Pressure Distribution Comparison for the Baseline Case

As shown in *Figure 5.6*, the static pressure distribution at the leading edge and the trailing edge were examined. There is no doubt that the design intention was not achieved for the baseline case. The slope of the pressure gradient at the trailing edge from CFX results is smaller than the 1D design intent from 5% to 50% span location, which caused the radial force imbalance shown in *Figure 5.5*.





(a)

(b)

Figure 5.7 Mach Profile Comparison for Baseline Case (a) 3% Span Location and (b) 35% Span Location

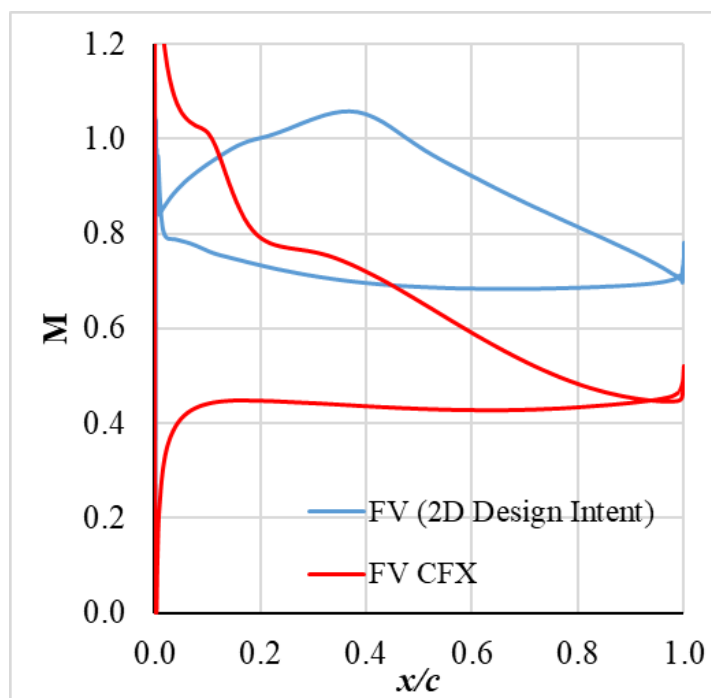


Figure 5.8 Mach Profile Comparison for Baseline Case at 98% Span Location

As shown in *Figure 5.7* and *Figure 5.8*, the Mach profile distributions were evaluated and compared as well.

The distinctions between the 2D and 3D Mach profiles are significant for the baseline case at 3%, 35% and 98% span locations. Huge positive incidences indicate that the blade didn't align with the inlet flow angle in the 3D simulations where viscous effects played an important role in the turbulence model, even though it was designed perfectly in the 2D analysis. It is not only part of the reason why the flow didn't behave as what was designed at the beginning, but also can harm the compressor stall margin as will be discussed in later sections.

Therefore, it can be easily concluded that the design intent for both the leading edge treatment and trailing edge treatment failed for the Baseline case.

## **5.2. Hybrid Vortex**

### **5.2.1. 1D Design Point**

Care must be taken when it comes to the Hybrid Vortex. As mentioned before, an axial velocity profile after an inlet guide vane needs to be imported into the radial equilibrium equation. However, because of the characteristic difference, slight modifications such as inlet mass flow rate and inlet Mach number need to be performed, at the mid span location, in order to maintain the same overall boundary conditions and not distort the outcome.

### **5.2.2. Axial Velocity Convergence Iteration**

The procedure for the hybrid vortex case design was the same as the baseline case. Referencing the hybrid vortex design flowchart, *Figure 3.6*, one iteration of redesign was necessary if the axial velocity profile generated from CFX results was not

the same as what was used for the hybrid vortex cases A and B.

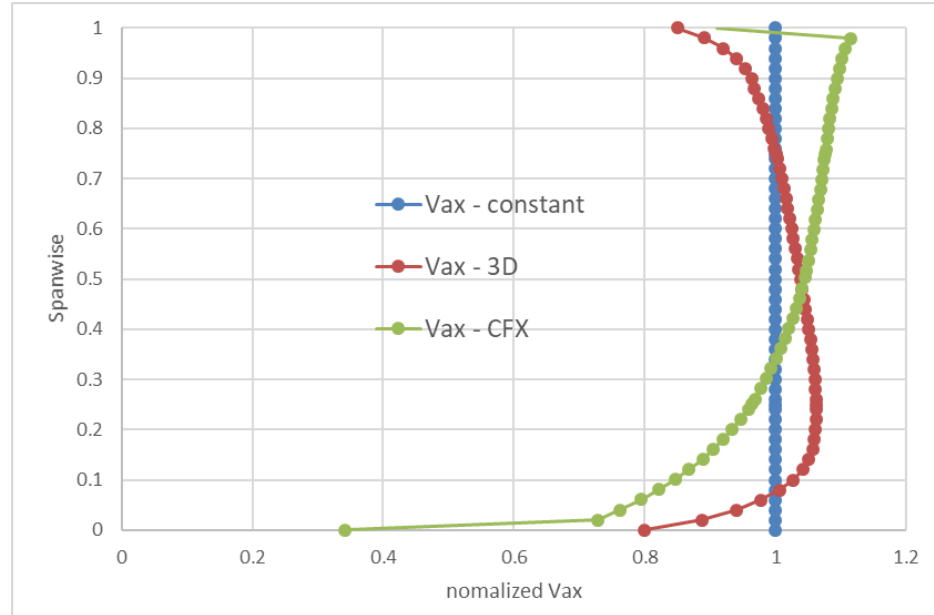


*Figure 5.9* The Comparison of Vax Profile Shape

As shown in *Figure 5.9* above, the normalized axial velocity profiles are completely different, but they share the same average axial velocity. Furthermore, they are all plotted at the leading edge of the rotor and the axial velocity profile generated from CFX results is more accurate for this particular design compared with the axial velocity profile found from reference. Therefore, the hybrid vortex case C has been created using the axial velocity profile from the CFX result of the hybrid vortex case B, which was the final design result. The corresponding initialized profile is attached in Appendix “E”.

### 5.3. Final Hybrid Vortex Case

#### 5.3.1. 2D Airfoil Stacking and Comparison

The 2D design of the Hybrid Vortex airfoils were constructed using the same method as the Baseline case discussed in section 5.1.2. The stacking view is shown in

*Figure 5.10.* 2D Mach profiles for each span locations conform to the same principles and criteria as those utilized for the FV design and are presented in Appendix “G”.

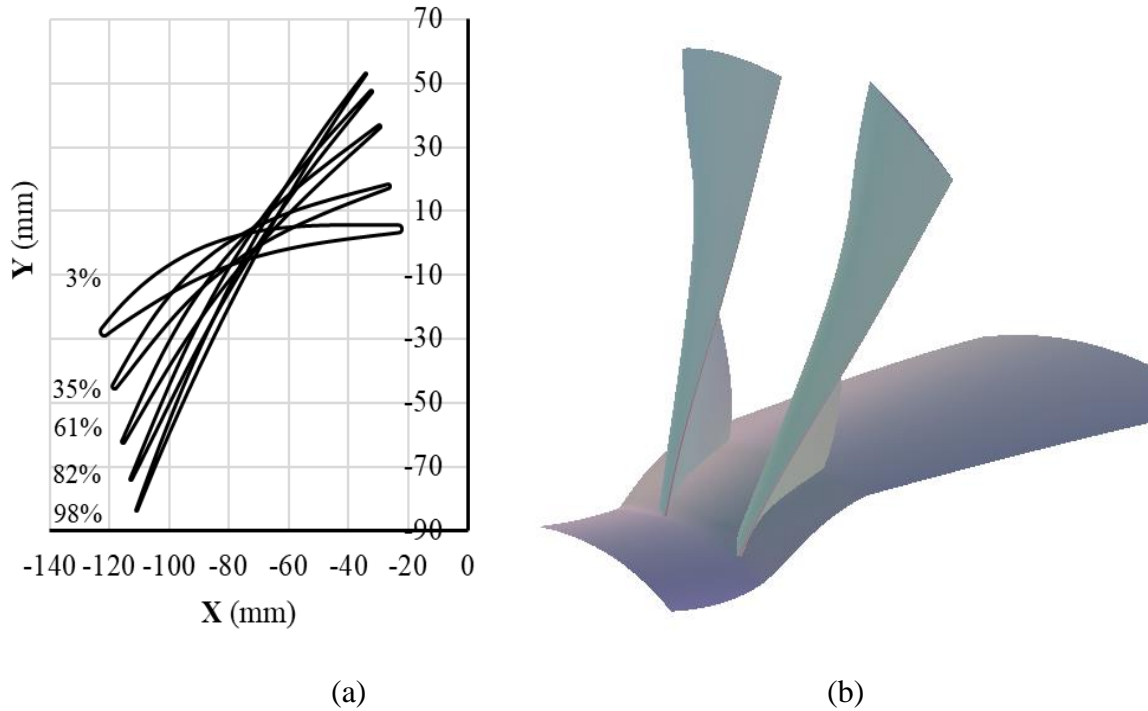


*Figure 5.10* Hybrid Vortex Case C Blade Stacking View

*Figure 5.11* shows the 3D blade geometry comparison between the baseline case and the Hybrid Vortex case C. As can be seen in the picture, the HV case C has less solidity at the tip and more stagger below the mid. A closer observation about airfoil shape at the hub shows that the HV case C has bigger beta and less camber than the baseline case in *Figure 5.12*. It is beneficial to compressor stall margin because the separation at the hub is mainly due to the high camber and the ability to handle positive incidence. Because of less camber at the hub, the work load was redistributed. It resulted in more camber and more work loading at the 35% span location as demonstrated in *Figure 5.13*. The remaining 2D airfoil comparisons for each span location are presented

in Appendix “H”.

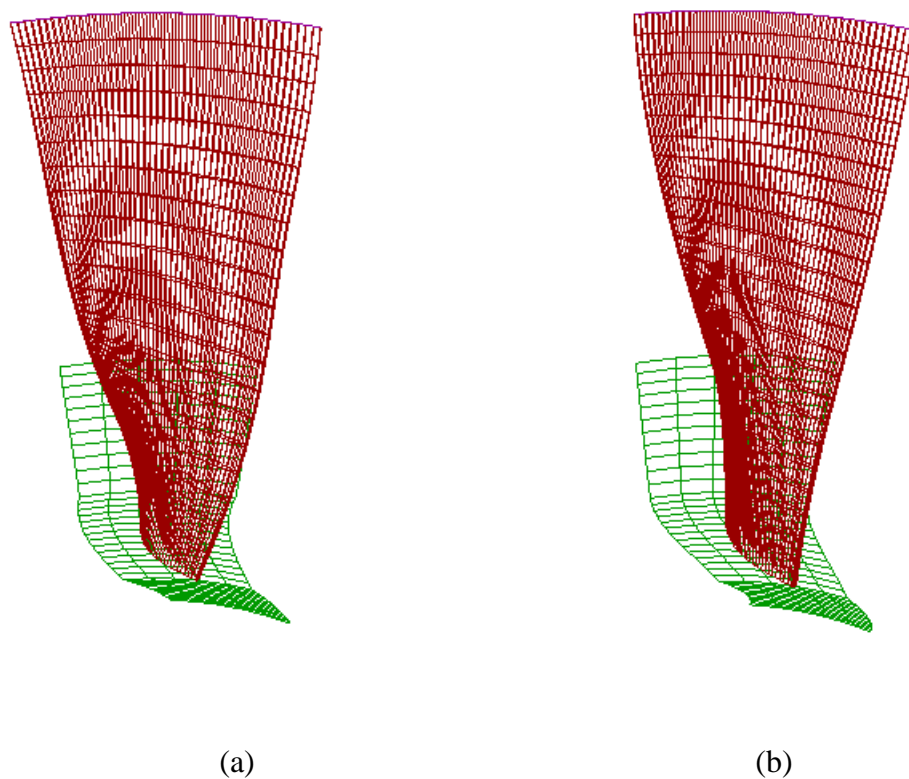


Figure 5.11 3D Blades Geometry Comparison (a) Free Vortex and (b) Hybrid Vortex Case C

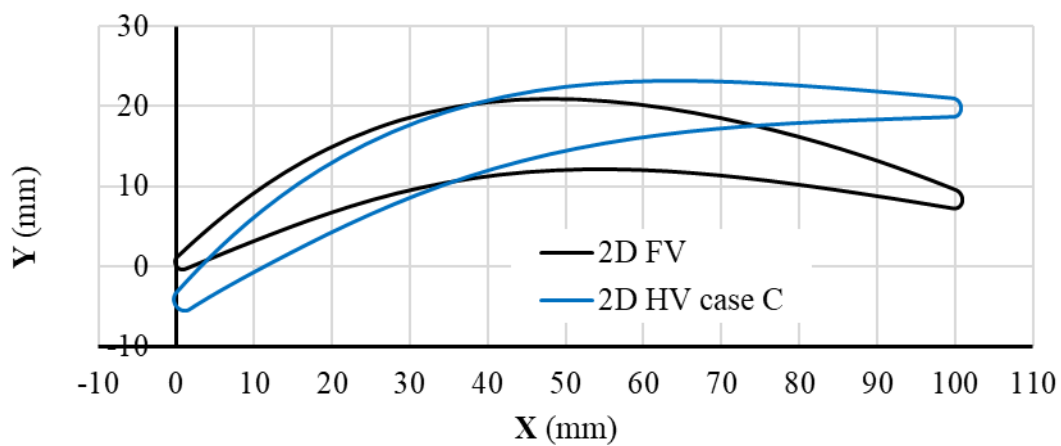


Figure 5.12 2D Airfoils Shape Comparison at 3% Span Location

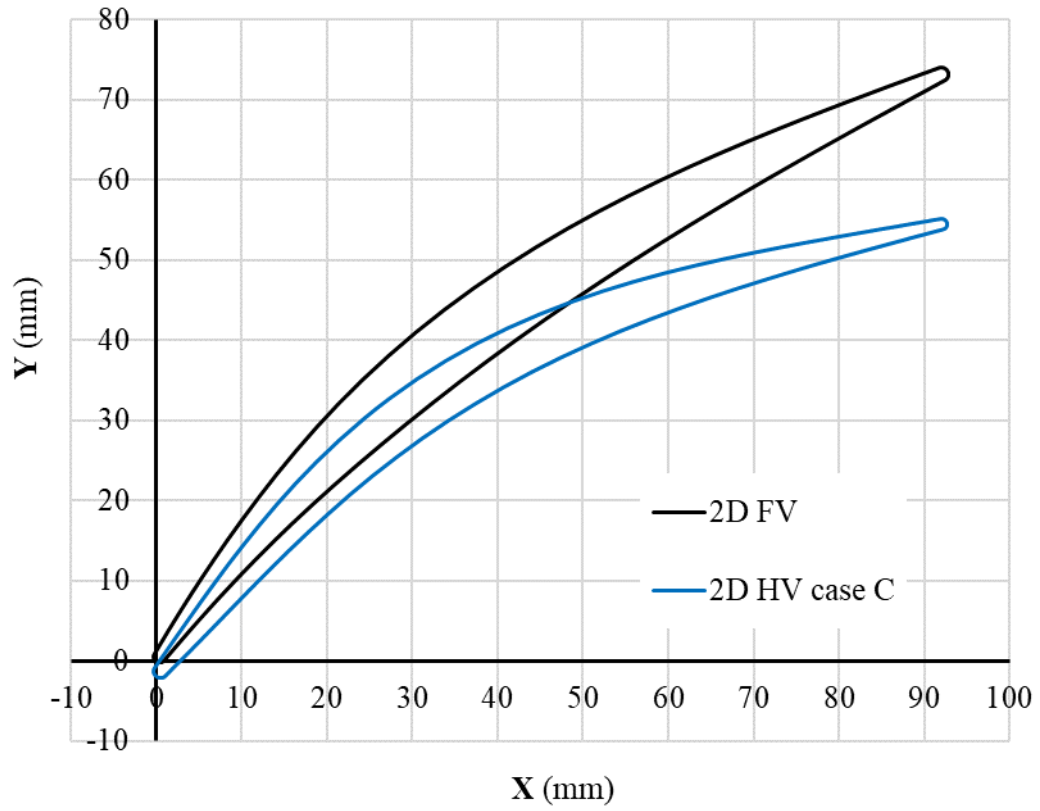


Figure 5.13 2D Airfoils Shape Comparison at 35% Span Location

### 5.3.2. Observed Flow Features and Comparison

The 3D performance of the Hybrid Vortex case C has been examined using the same process as the baseline case. The design point performance is summarized in Table 5.3.

Table 5.3

*Hybrid Vortex Case C 3D Design Point Parameters*

Variable		Value
Mass Flow Rate	m (kg/s)	72.5001
Pressure Ratio	$\pi_0$	1.2927
Isentropic Efficiency	(%)	95.8165

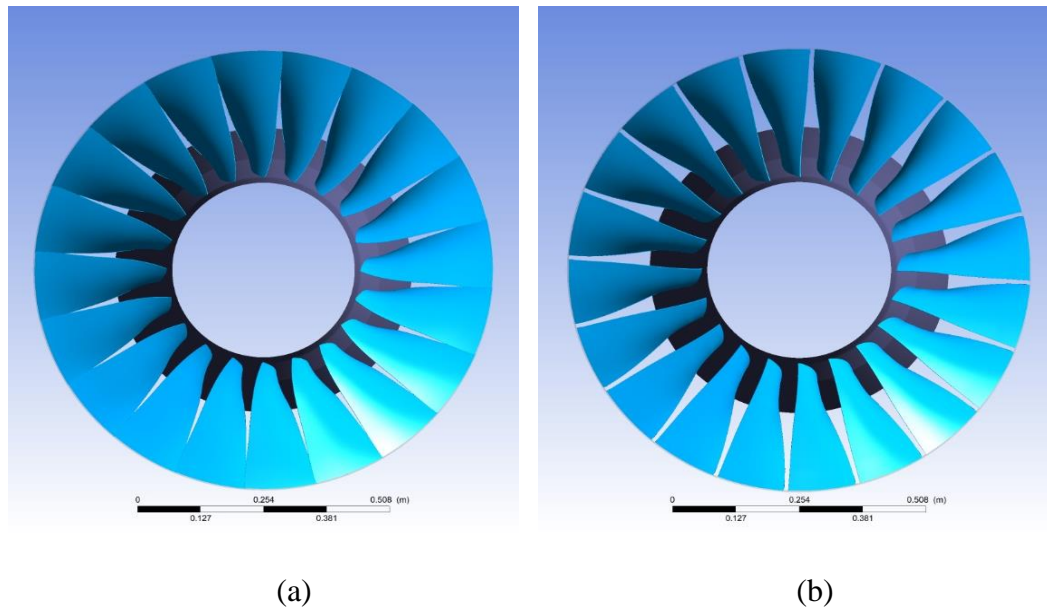


*Figure 5.14 3D Geometry Comparison between Baseline Case (a) and Hybrid Vortex Case C (b)*

As is shown in the table above, pressure ratio reached the target at 72.5 kg/s mass flow rate, which is less than what was designed in the 1D analysis (80 kg/s) as well.

However, it is a great improvement over the baseline case. As is shown in *Figure 5.14*, because the new Hybrid Vortex solution took account of viscous effects, it delivered a blade with less solidity and blockage. Thus, it resulted in more mass flow at the design point.

Unlike the baseline case, the feedback from the 3D CFD for the Hybrid Vortex case C agrees with the previous 2D analysis. As shown in *Figure 5.15*, the stagnation point was on the center of the leading edge, which is consistent with the density contour plot in figure 5.15 (b). This indicates that the new vortex design methodology successfully captured the 3D effects in the early stages of design, which is one of the goals for this research.

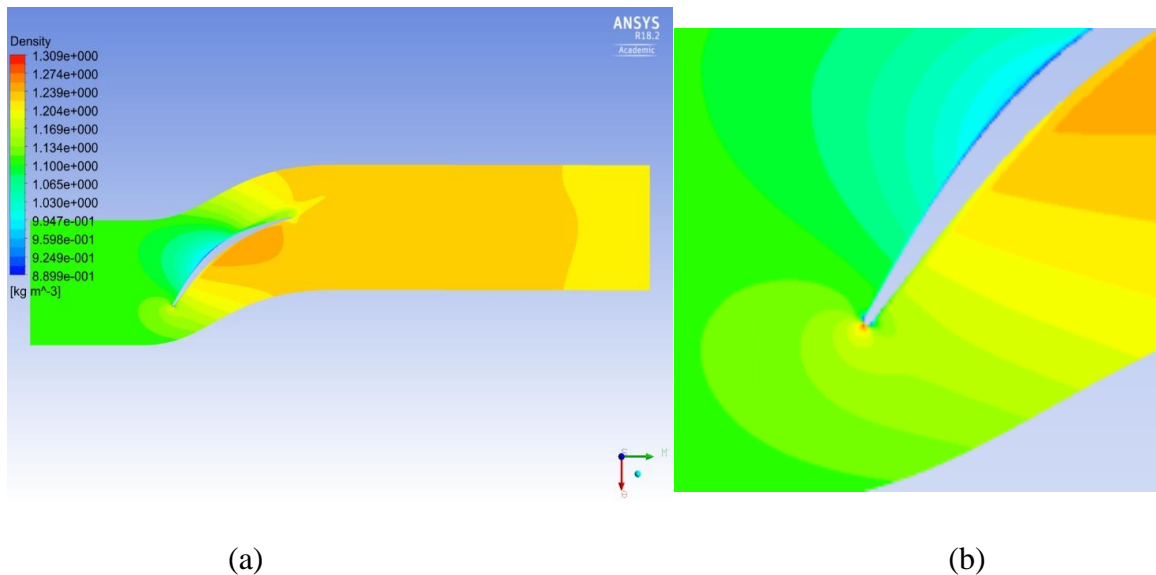


*Figure 5.15* Hybrid Vortex Case C 35% Span location Density Contour (a) and LE Enlarged View(b)

The improvement is also evident when checking the streamline plot for the Hybrid Vortex case C as demonstrated by *Figure 5.16* to *Figure 5.19*. From the side view, the streamlines were subject to the centrifugal forces from hub to tip in the Baseline



case, while this phenomenon was eliminated in the Hybrid Vortex case C. There were a few negligible streamlines at the trailing edge because the flow was outside the channel. It was a significant improvement compared with the baseline case, as is shown clearly in *Figure 5.17*.

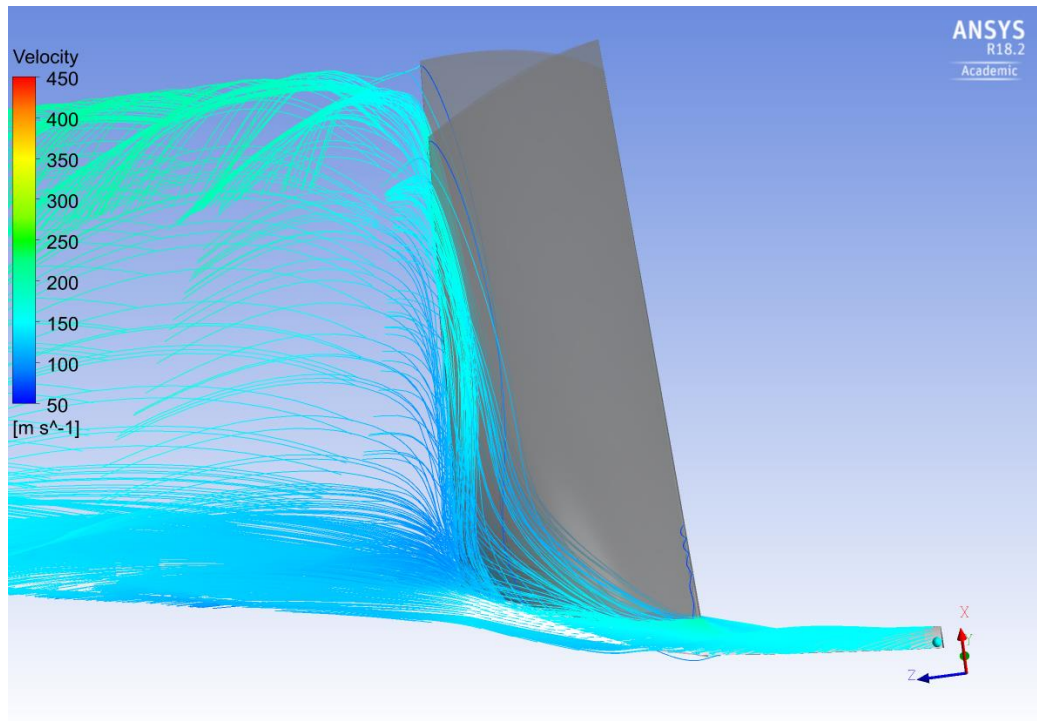


*Figure 5.16* Baseline Case Flow Path Streamline Plot on 3% Span Location (Side View)

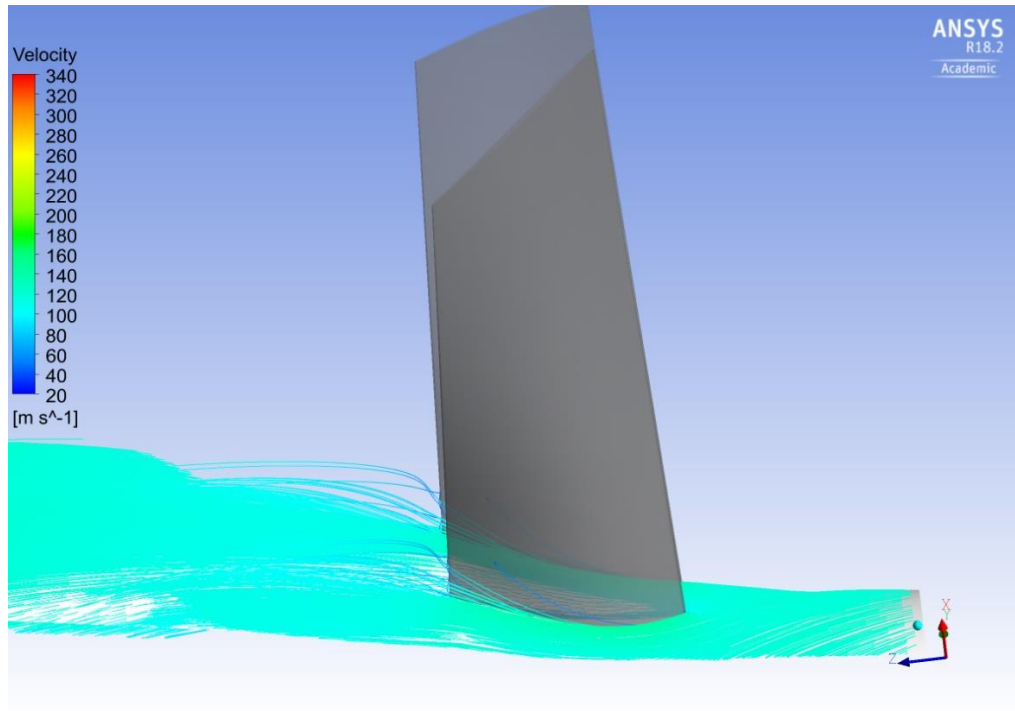


Figure 5.17 Hybrid Vortex Case C Flow Path Streamline Plot on 3% Span Location (Side View)

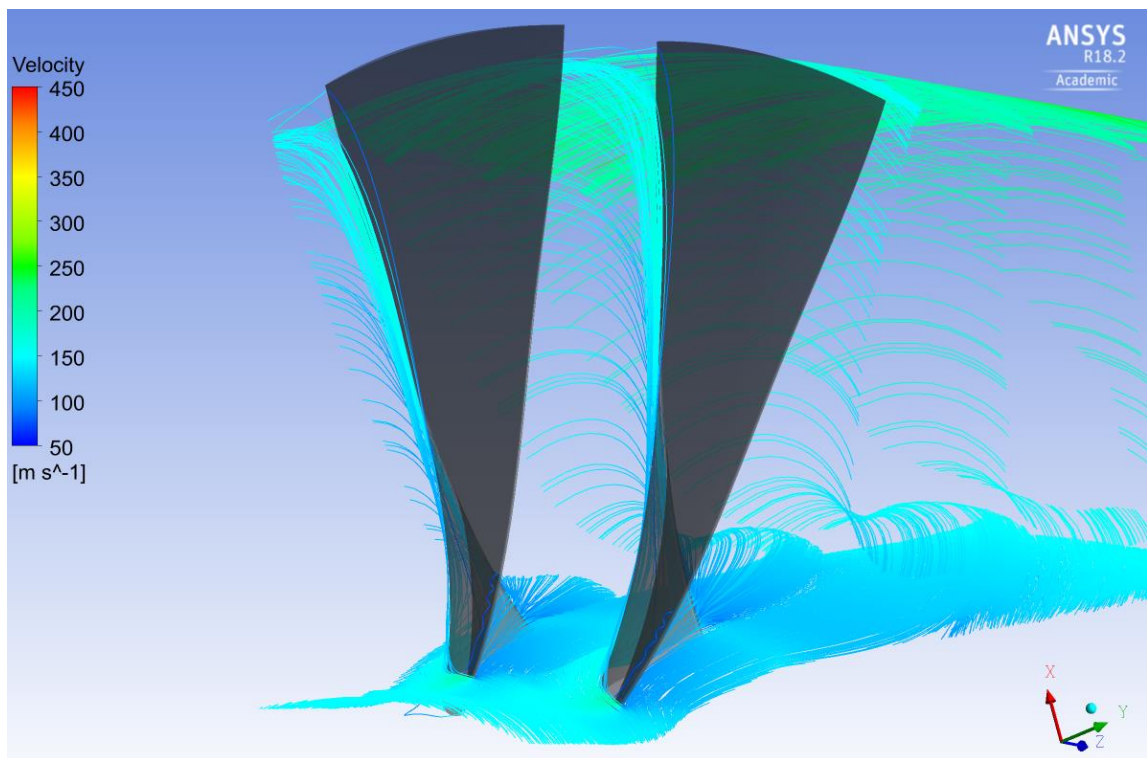
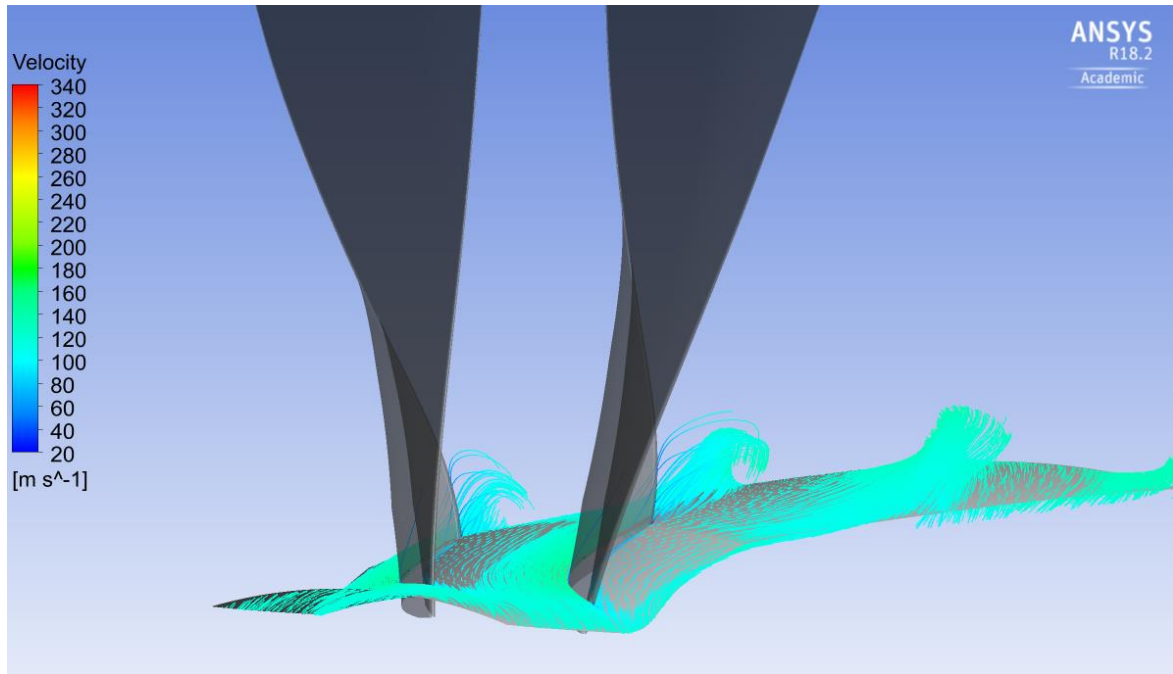


Figure 5.18 Baseline Case Flow Path Streamline Plot on 3% Span Location (Front View)



*Figure 5.19* Hybrid Vortex Case C Flow Path Streamline Plot on 3% Span Location (Front View)

Because of the added viscous on the blade surface, the momentum of the flow particles near the surface is more impacted and thus, it is more difficult to reach radial equilibrium. Examining the streamlines in the channel is a better way to evaluate whether the new vortex solution balanced the centrifugal force in the streamwise direction. As shown in *Figure 5.18* and *Figure 5.19*, the improvement is evident and it can be said the new vortex solution was a success as close to the hub as the 3% span location. The streamlines were straight from the leading edge to the trailing edge in the Hybrid Vortex case C, while they were centrifuged out in the Baseline case.

A similar study was performed at the 10% span location as well. As shown in *Figure 5.20* to *Figure 5.23*, the same phenomenon was observed and radial equilibrium was achieved at the 10% span location.

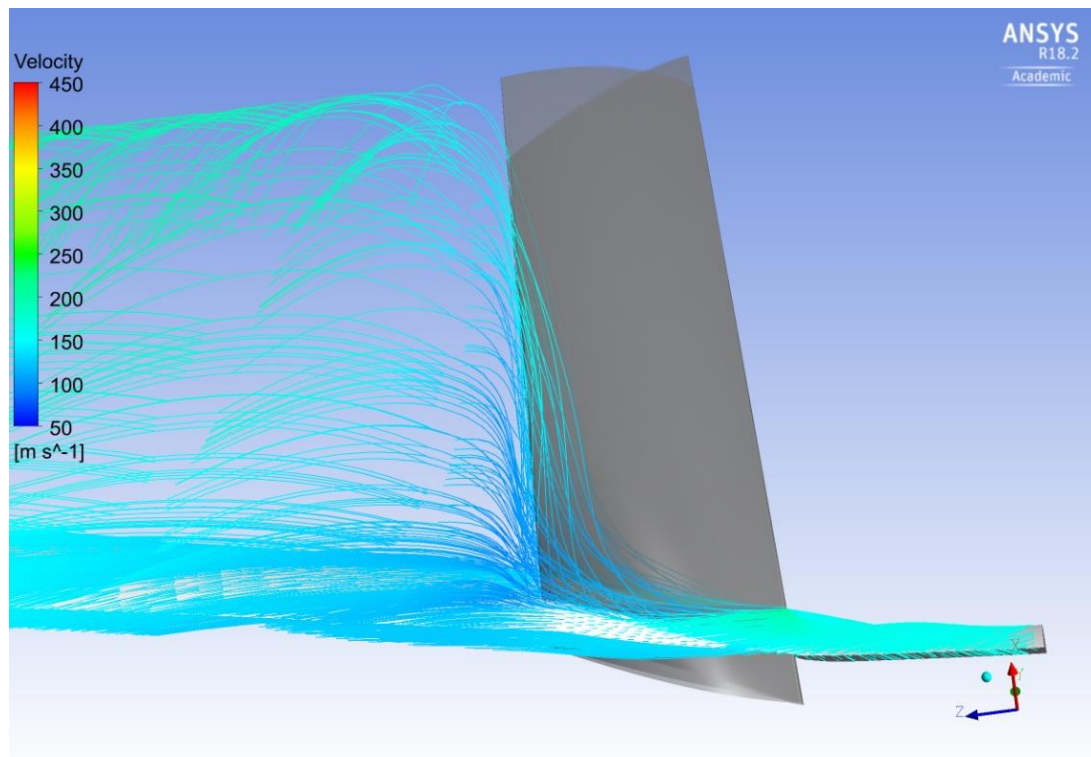


Figure 5.20 Baseline Case Flow Path Streamline Plot on 10% Span Location (Side View)

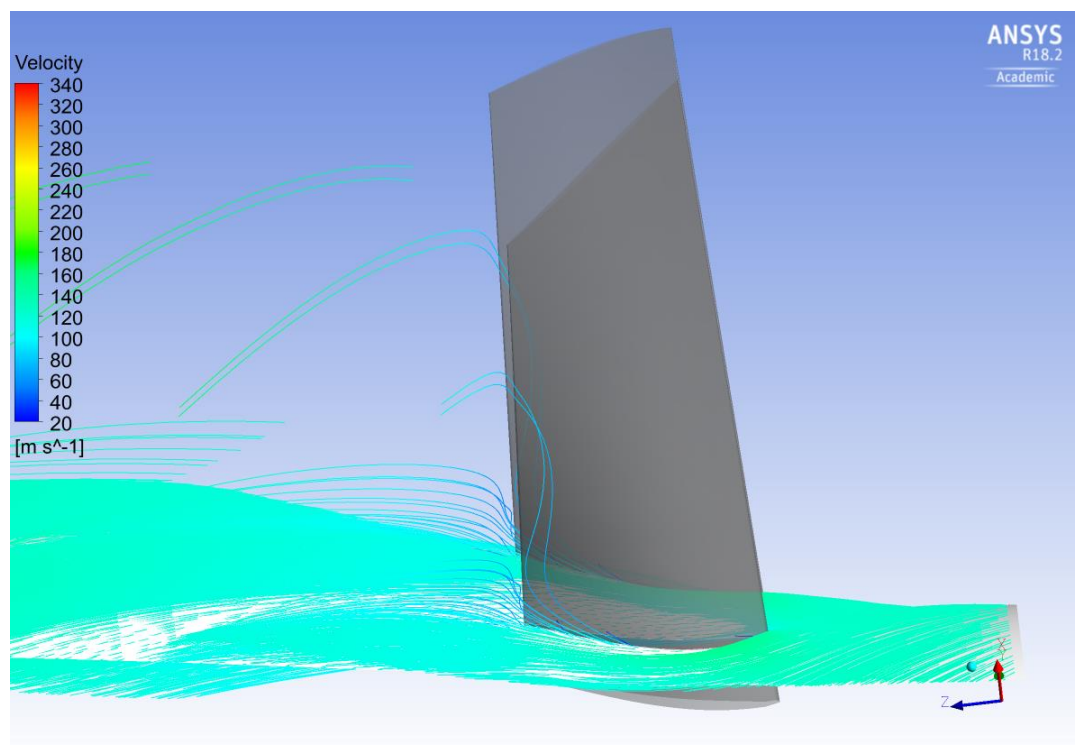


Figure 5.21 Hybrid Vortex Case C Flow Path Streamline Plot on 10% Span Location (Side View)

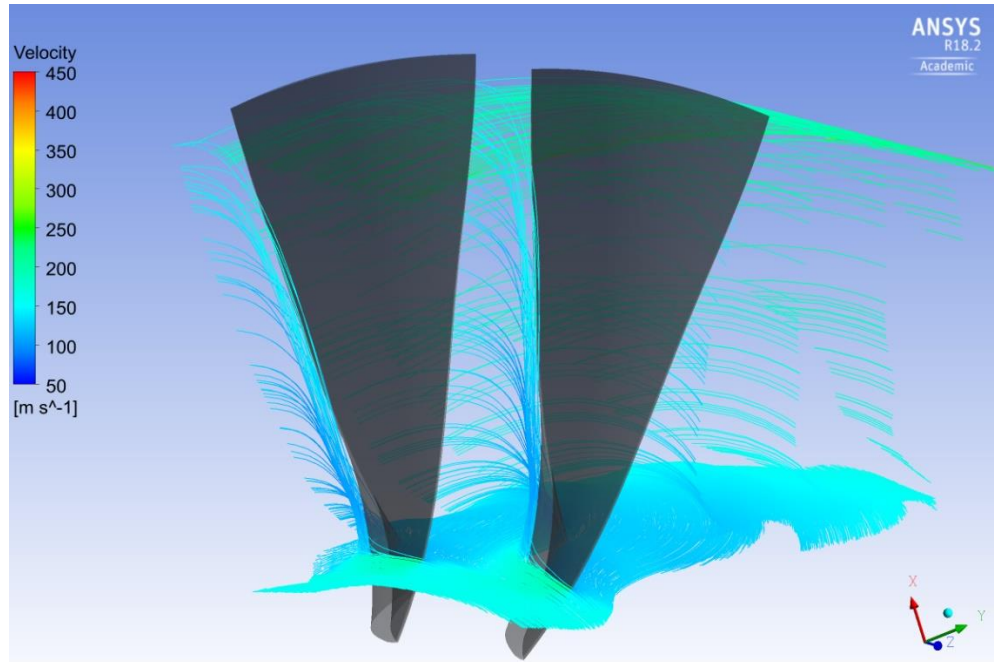


Figure 5.22 Baseline Case Flow Path Streamline Plot on 10% Span Location (Front View)

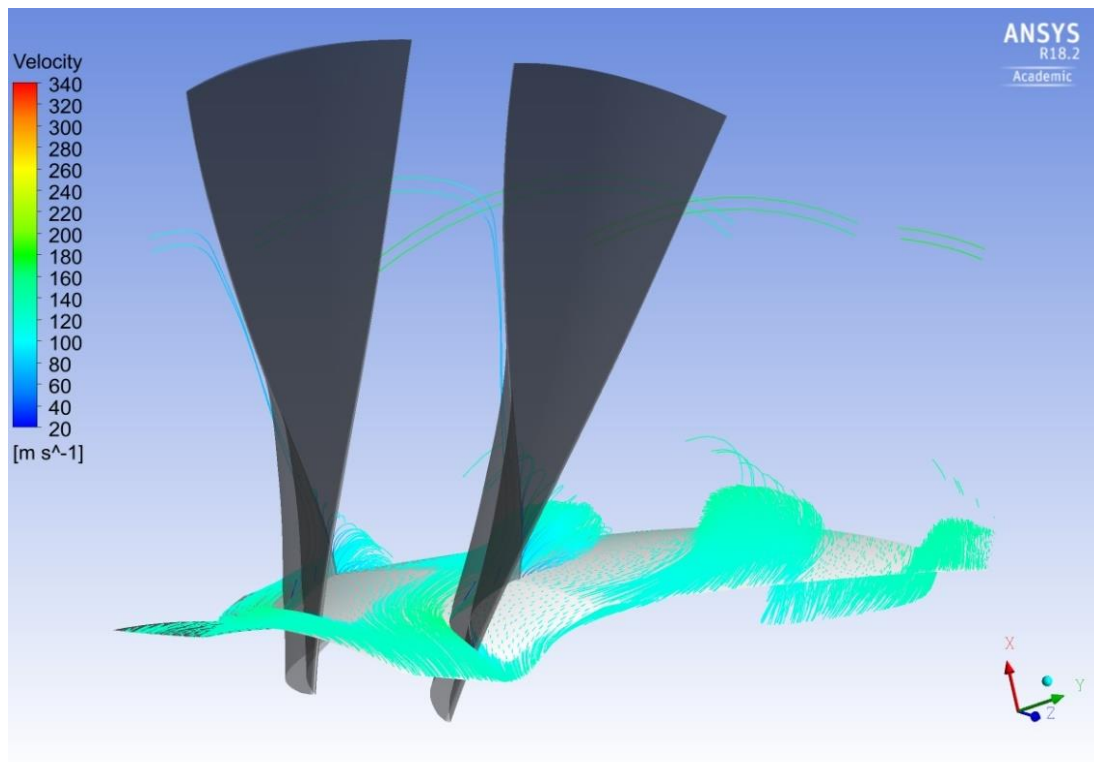
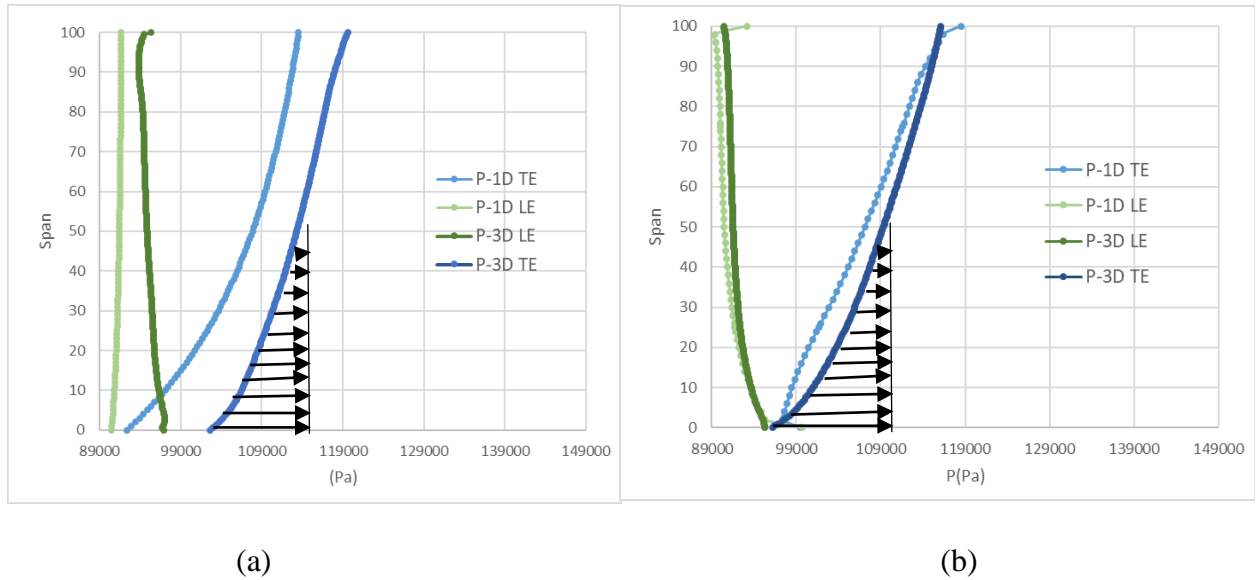


Figure 5.23 Hybrid Vortex Case C Flow Path Streamline Plot on 10% Span Location (Front View)





*Figure 5.24* Static Pressure Distribution Comparison for Baseline Case (a) and Hybrid Vortex Case C (b)

As shown in Figure 5.24, the static pressure distribution comparison between the two cases indicates that the Free Vortex case didn't achieve the desired pressure gradient since it neglected end-wall effects. While the 3D results for the Hybrid Vortex case C highly agreed with the 1D design intent, which is to impose a greater pressure gradient near the hub to stabilize the flow. Introducing viscous effects early in the design stage, as is the case with the HV method, resulted in the blade being more aligned with the flow. The improved performance is clear.

Contrary to the Baseline case, the distinctions between the 2D and 3D Mach profiles are insignificant for the Hybrid Vortex case C at 35% and 98% span locations. The leading edge treatment and the trailing edge treatment appear to have accomplished the objective for the new vortex solution.

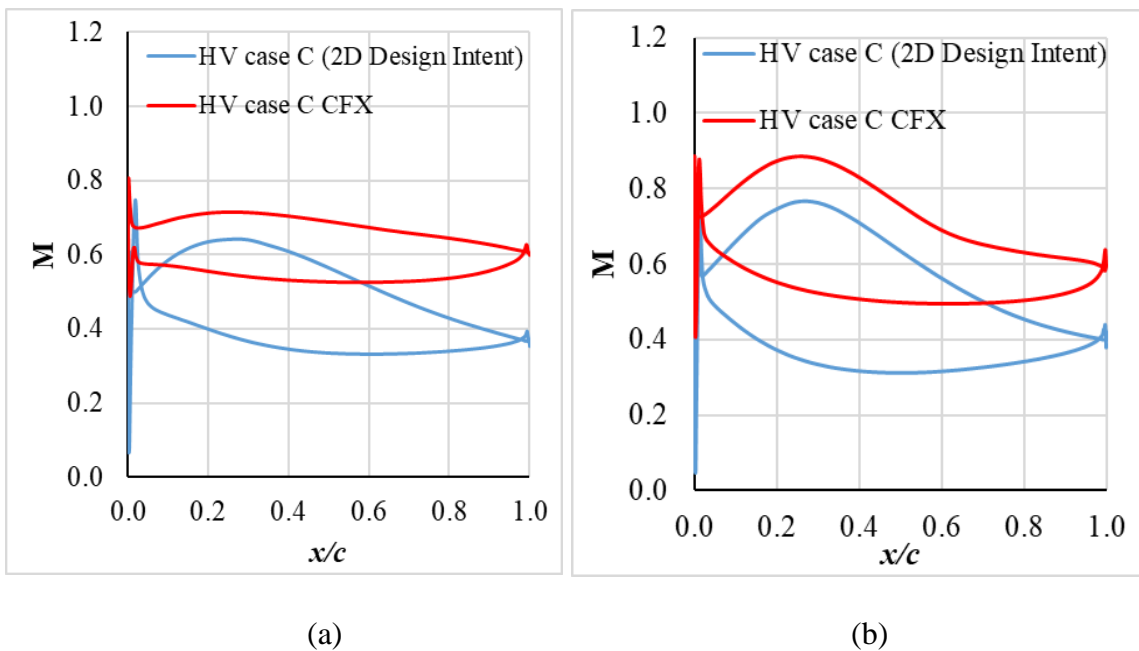


Figure 5.25 Mach Profile Comparison for Hybrid Vortex Case C (a) 3% Span Location and (b) 35% Span Location

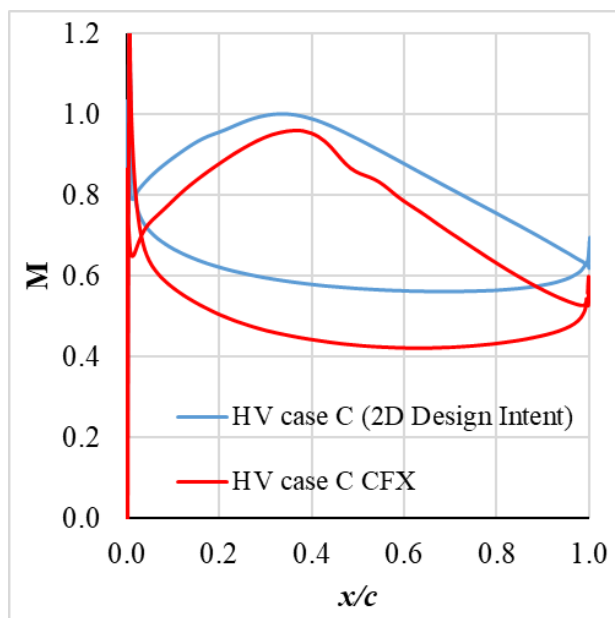


Figure 5.26 Mach Profile Comparison for Hybrid Vortex Case C at 98% Span Location

### 5.3.3. Off-Design Behavior

The general behavior of a compressor can be evaluated from its compressor map. And it is also a tool to verify the improvement introduced by the new design method. Three characteristic lines were produced to generate the full map for both cases at different rotational speeds: 5,795 rpm, 6,100 rpm and 7,200 rpm.

Figure 5.27 shows the compressor map for the FV case (red) and the HV case (blue). The design point values for both cases are summarized in Table 5.4. Apparently, the Hybrid Vortex blade can deliver more pressure ratio as well as more mass flow operating range.

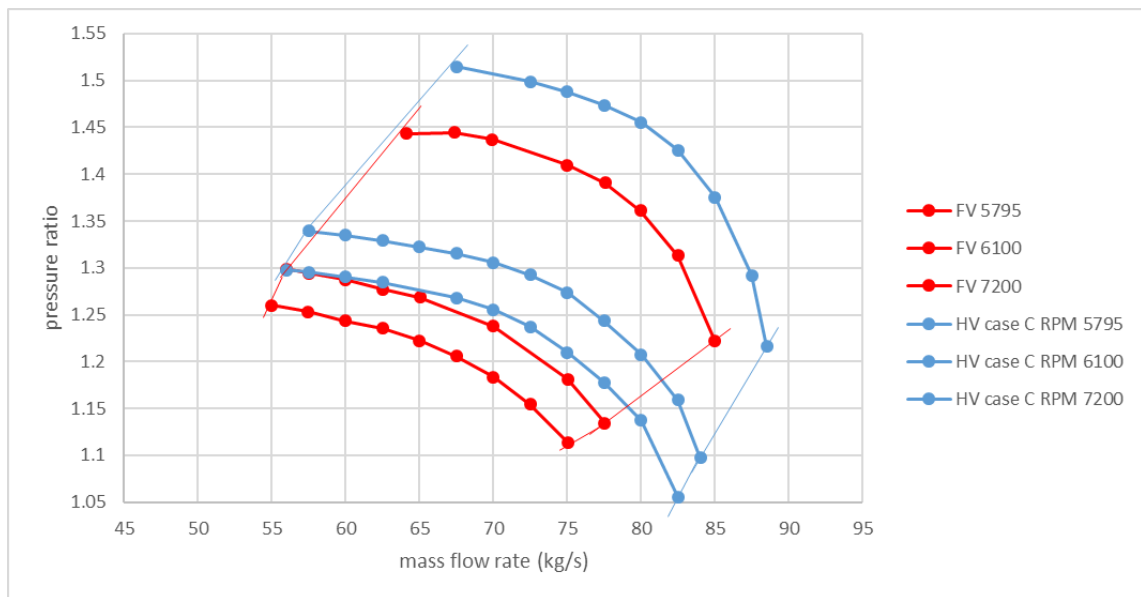


Figure 5.27 Compressor Map Comparison between Free Vortex Case and Hybrid Vortex Case C

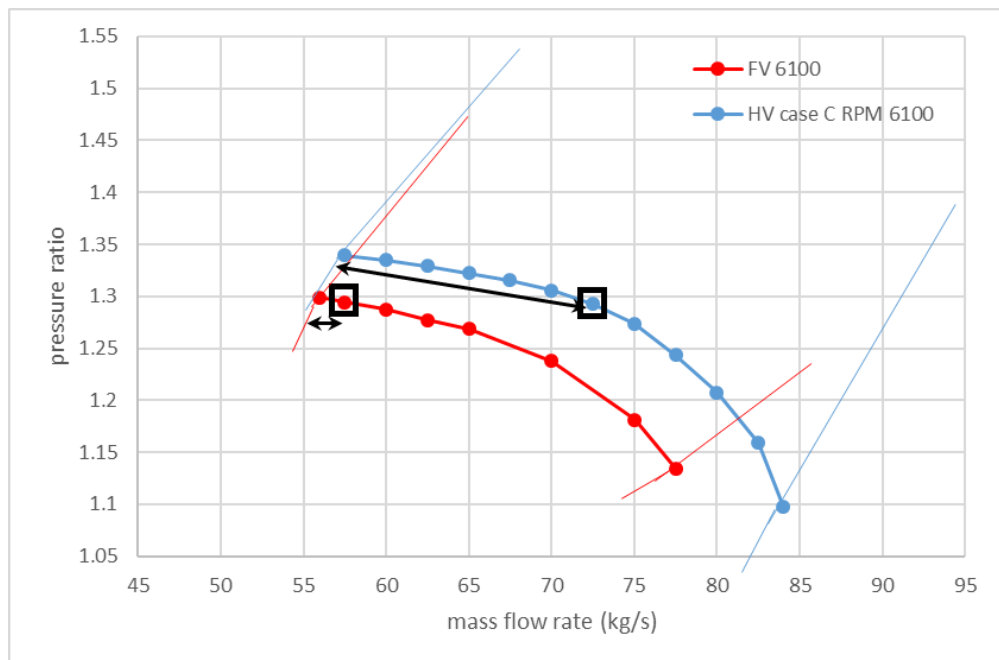


Table 5.4

*Design Point Values*

Case	Mass Flow Rate(kg/s)	Pressure Ratio $\pi_0$	Isentropic Efficiency
Free Vortex	57.5	1.2945	93.7871
Hybrid Vortex Case C	72.5	1.2927	95.8165

Characteristic line comparison at rpm 6100 between the Free Vortex case and the Hybrid Vortex case C was performed in *Figure 5.28*. It shows a considerable increase in the operating range for the airfoil. The design point for the Baseline case was close to stall, while the design point for the Hybrid Vortex case C was operating at 72.5 kg/s, 15 kg/s more than the Baseline case (+26%) with the same total pressure ratio. The detailed mass flow operating range comparison is summarized in Table 5.5. The increase in operating range is 16.15% for the new vortex solution.



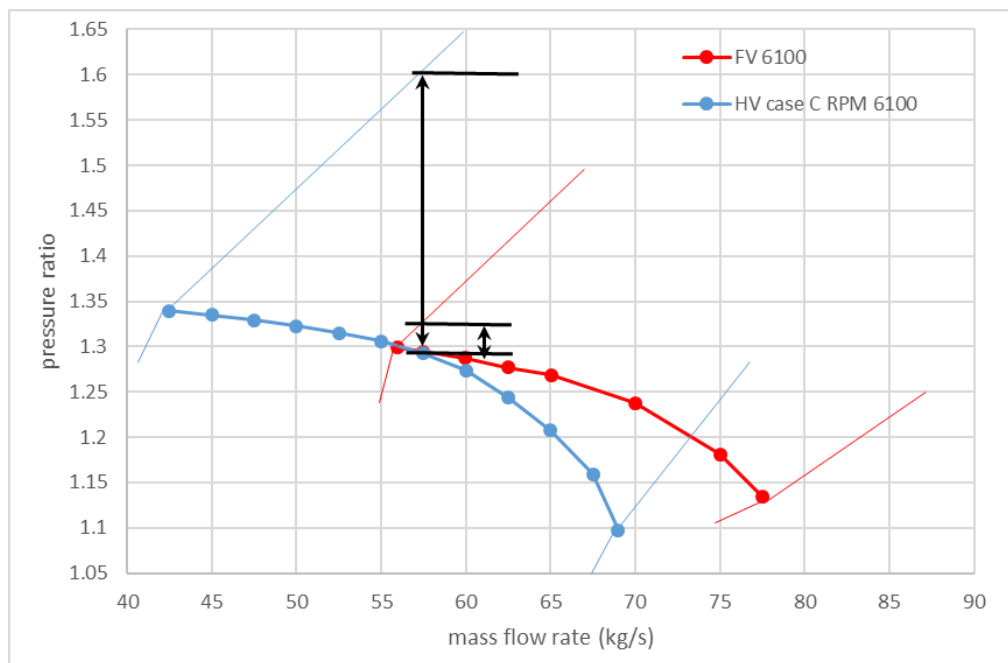
*Figure 5.28* Characteristic Line Comparison at RPM 6100 between Free Vortex Case and Hybrid Vortex Case C

Table 5.5

*Mass Flow Operating Range Comparison*

Case	Surge Mass Flow Rate(kg/s)	Choke Mass Flow Rate(kg/s)	Difference (kg/s)
Free Vortex	55.9884	77.5135	21.5251
Hybrid Vortex Case C	57.5002	82.5014	25.0012
		Increase	16.149%

Theoretically, the compressor map can be relocated by redesigning the blade while maintaining the Hybrid Vortex methodology. The design point would be matched at the same total pressure ratio and the same mass flow rate. This redesign has the potential to relocate the characteristic line as illustrated in *Figure 5.29*, where the Hybrid Vortex characteristic line has been relocated 15kg/s to the left to match the design points of both designs.



*Figure 5.29* Hypothetical Characteristic Line Comparison at RPM 6100 between Free Vortex Case and Hybrid Vortex Case C

In *Figure 5.29*, the surge margin for the hypothetical characteristic lines were marked in black. With the same design point, the increase in surge margin for the hypothetical characteristic line has been calculated. The values of the surge margin are summarized and presented in *Table 5.6*. The potential for the Hybrid Vortex solution are significant. It has 23.77% surge margin compared with 2.356% surge margin for the Free Vortex solution.

Table 5.6

*Surge Margin Comparison*

Case	Designed Pressure Ratio	Surge Pressure Ratio	Surge Margin %
Free Vortex	1.2945	1.325	2.356
Hybrid Vortex Case C	1.2927	1.6	23.772

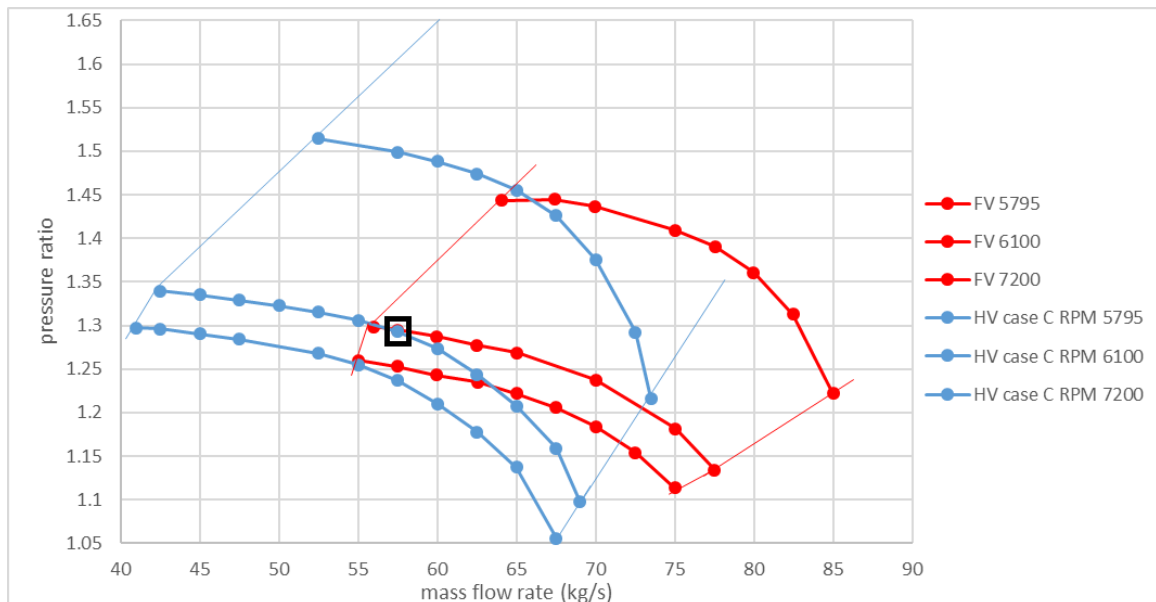


*Figure 5.30* Hypothetical Compressor Map Comparison between Free Vortex Case and Hybrid Vortex Case C

The corresponding compressor map for hypothetical Hybrid Vortex redesign is presented in *Figure 5.30*. The new map is a marked increase in both mass flow operating range and surge margin. The potential for the new Hybrid Vortex solution is certain, requiring additional optimization to match the design point.

## 6. Conclusion

A new Hybrid Vortex theory and design methodology for preliminary design in axial compressors has been presented. The simple radial equilibrium equation has the advantage of predicting swirling flow between blades rows and providing a radial pressure distribution from hub to tip, but it fails to predict the end-wall effect. An axial velocity profile based on the actual physics of the flow is imported in radial equilibrium equation in order to introduce a higher level of fidelity early into the design process.

Preliminary design comparisons among Free Vortex solution, Constant Reaction solution, Forced Vortex solution and Exponential solution are performed. Although Exponential solution has the best performance among four cases, the Free Vortex solution has been chosen as the Baseline case because of the limitation of throughflow code.

Three different approaches were studied in order to find a good way to implement the Hybrid Vortex theory. The Hybrid Vortex Case C is the best one. It was found out that introducing a real normalized  $V_{ax}$  profile after the IGV into the hybrid vortex design and deriving the circumferential velocity distribution will introduce an unrealistic alpha profile for the compressor rotor. Therefore, decoupling the axial velocity profile from the alpha profile is the final treatment for the leading edge. Furthermore, the trailing edge treatment has a tip-strong total pressure modification in order to maintain a positive pressure gradient.

The blade performance was examined and verified using CFX simulations. At the design point, 3D simulation results for the Hybrid Vortex case C were highly agreed with 2D analysis results. While, 3D results and 2D results had huge differences for the

Baseline case. It validated the reliability of the Hybrid Vortex theory. Moreover, the Hybrid Vortex case C had great improvements in off-design performance. The design point for the Baseline case was close to stall, while the design point for the Hybrid Vortex case C was operating at 72.5 kg/s, 15 kg/s more than the Baseline case (+26%) with the same total pressure ratio. With further re-design the Hybrid Vortex case C, it has 23.77% surge margin compared with 2.356% surge margin for the Baseline case.

## **7. Recommendations**

Many issues occurred throughout the study. It is highly recommended to change a better throughflow code to perform the streamline curvature analysis. The current code is easy to use but does not provide reasonable solidity (especially at the hub) which will affect the input for 2D analysis. It is also recommended to choose a front-loaded shape of Mach profile in 2D analysis in order to eliminate or smaller the deviation angle for convergence.

This thesis only studied the Hybrid Vortex solution for the rotor. It would be better to have a further study in rotor-stator interaction (after the refinement of the rotor blade) and to see how the hybrid vortex theory works through multi-stage axial compressors.

## REFERENCES

- ANSYS, Inc. (n.d.). ANSYS CFX User Guide. Retrieved November 2013, from <https://itrss.mst.edu/media/informationtechnology/itrss/documents/ansysdocs/ANSYS%20CFX%20Reference%20Guide.pdf>
- Chima, R. V. (1999, March 1). GRAPE 2-D Grid Generator for Turbomachinery. 10. Cleveland, Ohio, USA: NASA Glenn Research Center. Retrieved 2015
- Chima, R. V. (1999, March 1). RVCQ3D - Rotor Viscous Code Quasi-3-D. 18. Cleveland, Ohio, USA: NASA Glenn Research Center. Retrieved 2015
- Cornelius, C., Biesinger, T., Galpin, P., & Braune, A. (2014). Experimental and computational analysis of a multistage axial compressor including stall prediction by steady and transient CFD methods. *Journal of Turbomachinery*, 136(6), 061013.
- Crouse, J. E., & Gorrell, W. T. (1981). Computer Program for Aerodynamic and Blading Design of Multistage Axial-Flow Compressors. NASA-TP-1946. National Aeronautics and Space Administration Lewis Research Center.
- Cumpsty, N. A. (1989). Compressor aerodynamics (No. BOOK). Longman Scientific & Technical.
- Cumpsty, N. A., & Greitzer, E. M. (2004). Ideas and methods of turbomachinery aerodynamics: a historical view. *Journal of propulsion and power*, 20(1), 15-26.
- Day, I. J. . (1971). Axial compressor performance during surge. *Journal of Propulsion & Power*, 10(3), 329-336.
- Glassman, Arthur J. & Lavelle, Thomas M. & United States. National Aeronautics and Space Administration. (1995). Enhanced capabilities and modified users manual for axial-flow compressor conceptual design code CSPAN. [Washington, DC] : [Springfield, Va : National Aeronautics and Space Administration ; National Technical Information Service, distributor
- Hall, C., & Dixon, S. L. (2013). Fluid mechanics and thermodynamics of turbomachinery. Butterworth-Heinemann.
- Hill, Philip G., & Peterson, Carl R. (1992). Mechanics and thermodynamics of propulsion (2nd revised and enlarged edition). (P. G. Hill & C. R. Peterson, Eds.), Reading. Reading, MA: Addison-Wesley Publishing Co.
- Horlock, J. H. (1958). Axial flow compressors: fluid mechanics and thermodynamics. Butterworths scientific publications.



- Howell, R. A. (1945). Fluid dynamics of axial compressors. ARCHIVE: Proceedings of the Institution of Mechanical Engineers 1847-1982 (vols 1-196), 153(1945), 441-452.
- Köller, U., Mönig, R., Küsters, B., & Schreiber, H. A. (1999, June). Development of Advanced Compressor Airfoils for Heavy-Duty Gas Turbines: Part I—Design and Optimization. In ASME 1999 International Gas Turbine and Aeroengine Congress and Exhibition (pp. V001T03A021-V001T03A021). American Society of Mechanical Engineers.
- Korakianitis, T., & Zou, D. (1993, May). Through-Flow Analysis for Axial-Stage Design Including Streamline-Slope Effects. In ASME 1993 International Gas Turbine and Aeroengine Congress and Exposition (pp. V001T03A024-V001T03A024). American Society of Mechanical Engineers.
- Korn, D. G. (1978). Numerical design of transonic cascades. *Journal of computational physics*, 29(1), 20-34.
- Krain, H. (2005). Review of Centrifugal Compressor's Application and Development. *Transactions of the ASME, Journal of Turbomachinery*. DLR.
- Lieblein, S. (1965). Experimental flow in two-dimensional cascades. *NASA Special Publication*, 36, 183.
- Molinari, M., & Dawes, W. N. (2006). Review of evolution of compressor design process and future perspectives. *Proceedings of the Institution of Mechanical Engineers, Part C: Journal of Mechanical Engineering Science*, 220(6), 761–771. <https://doi.org/10.1243/09544062JMES298>
- Schmidt, E. (1980). Computation of supercritical compressor and turbine cascades with a design method for transonic flows. *Journal of Engineering for Power*, 102(1), 68-74.
- Stodola, A., & Loewenstein, L. C. (1905). *Steam Turbines: With an Appendix on Gas Turbines and the Future of Head Engines*. D. Van Nostrand Company.
- Wilson, D. G. (1998). *Design of high-efficiency turbomachinery and gas turbines*. MIT Press.
- Wu, C. H. (1952). A general theory of three-dimensional flow in subsonic and supersonic turbomachines of axial-, radial, and mixed-flow types (No. NACA-TN-2604). National Aeronautics and Space Administration Washington DC.
- Zheng, X., & Yang, H. (2016). End-wall boundary layers and blockages of multistage axial compressors under different conditions. *Journal of Propulsion and Power*, 1-9.

## A. Radial Equilibrium Derivations

### Radial Momentum Equation

Starting from the momentum equation:

$$F - \oint_{CS} p \cdot dS = \oint_{CS} (\rho V \cdot dS) \cdot V + \frac{d}{dt} \iiint_{CV} \rho \cdot V dV \quad (A.1)$$

Applying equation (A.1) to a small element:

$$f - \nabla p = (\rho V \cdot \nabla) V + \rho V \cdot (\nabla \cdot V) + \frac{d}{dt} (\rho \cdot V) \quad (A.2)$$

Splitting equation (A.2) into components:

$$f_r - \frac{1}{\rho} \frac{\delta p}{\delta r} = \frac{\partial V_r}{\partial t} + V_r \frac{\partial V_r}{\partial r} + \frac{V_u}{r} \frac{\partial V_r}{\partial u} + V_{ax} \frac{\partial V_r}{\partial ax} - \frac{V_u^2}{r} \quad (A.3)$$

$$f_u - \frac{1}{r\rho} \frac{\delta p}{\delta u} = \frac{\partial V_u}{\partial t} + V_r \frac{\partial V_u}{\partial r} + \frac{V_u}{r} \frac{\partial V_u}{\partial u} + V_{ax} \frac{\partial V_u}{\partial ax} - \frac{V_u V_r}{r} \quad (A.4)$$

$$f_{ax} - \frac{1}{\rho} \frac{\delta p}{\delta ax} = \frac{\partial V_{ax}}{\partial t} + V_r \frac{\partial V_{ax}}{\partial r} + \frac{V_u}{r} \frac{\partial V_{ax}}{\partial u} + V_{ax} \frac{\partial V_{ax}}{\partial ax} \quad (A.5)$$

With the assumption of axisymmetric flow:

$$\frac{\delta}{\delta u} = 0 \quad (A.6)$$

The radial velocity is assumed to be zero:

$$V_r = 0 \quad (A.7)$$

Assume steady flow:

$$\frac{\partial}{\partial t} = 0 \quad (A.8)$$

Assume infinitely long cylinder:

$$\frac{\partial}{\partial ax} = 0 \quad (\text{A.9})$$

With the assumption of no body forces:

$$f_r = f_{ax} = f_u = 0 \quad (\text{A.10})$$

Equation (A.3) can be rewritten to:

$$\frac{1}{\rho} \frac{dp}{dr} = \frac{V_u^2}{r} \quad (\text{A.11})$$

Which is the same as the Equation 3.3.

## Radial Equilibrium Equation

From the first law of thermodynamics:

$$dQ = dU + dW \quad (\text{A.12})$$

Work can be represented by:

$$dW = pdV \text{ (for a reversible process)} \quad (\text{A.13})$$

From the second law of thermodynamics for an internally reversible process:

$$dQ = Tds \quad (\text{A.14})$$

Because enthalpy is a function of the energy of the system:

$$H = U + pV \quad (\text{A.15})$$

Thus,

$$dH = dU + Vdp + pdV \quad (\text{A.16})$$

Substitute equations (A.12), (A.13) and (A.16) into equation (A.14):

$$Tds = dH - Vdp \quad (\text{A.17})$$

In the radial direction, considering a per mass system:

$$\frac{dh}{dr} = T \frac{ds}{dr} + \frac{dT}{dr} ds + \frac{1}{\rho} \frac{dp}{dr} \quad (\text{A.18})$$

Assuming  $\frac{dT}{dr} ds$  is a higher order term than the remaining parts of equation, it can

be eliminated. Substitute into equation (3.3):

$$\frac{dh}{dr} = T \frac{ds}{dr} + \frac{V_u^2}{r} \quad (\text{A.19})$$

The total enthalpy is defined as:

$$dh_0 = dh + d\left(\frac{V_r^2}{2} + \frac{V_u^2}{2} + \frac{V_{ax}^2}{2}\right) \quad (\text{A.20})$$

Equation (A.20) in the radial direction can be written as:

$$\frac{dh_0}{dr} = \frac{dh}{dr} + V_r \frac{dV_r}{dr} + V_u \frac{dV_u}{dr} + V_{ax} \frac{dV_{ax}}{dr} \quad (\text{A.21})$$

Substitute equation (A.19) into equation (A.21):

$$\frac{dh_0}{dr} = T \frac{ds}{dr} + \frac{V_u^2}{r} + V_r \frac{dV_r}{dr} + V_u \frac{dV_u}{dr} + V_{ax} \frac{dV_{ax}}{dr} \quad (\text{A.22})$$

Thus, with the assumption of  $\frac{dh_0}{dr} = 0$ ,  $\frac{ds}{dr} = 0$  and  $\frac{dV_r}{dr} = 0$ , the equation can be rearranged as:

$$\frac{d}{dr} (V_{ax})^2 = -\frac{1}{r^2} \frac{d}{dr} (rV_u)^2 \quad (\text{A.23})$$

Which is the same as the Equation 3.4.

## B. Various Vortex Solutions

Table B.1

*Vortex solutions (Horlock, 1958)*

<i>Method of Design</i>	<i>Work variation with radius</i>	<i>Tangential velocity distribution</i>	<i>Axial velocity distribution</i>	<i>Reaction distribution with radius</i>	<i>Radial equilibrium</i>
A. <i>Two-dimensional</i>	Supposed constant	Supposed constant	Supposed constant	Supposed constant	Ignored
B. <i>Free vortex</i>	Constant	$V_u r = \text{constant}$	Constant	Increases with radius	Yes
C. <i>Constant reaction (without equilibrium)</i>	Supposed constant	$V_u = ar^n \pm \frac{b}{r}$	Supposed constant	Supposed constant	Ignored
D. <i>Half vortex</i>	Supposed constant	Arithmetic mean of free vortex and constant reaction distributions	Supposed constant	Not far from constant	Ignored
E. <i>'Constant <math>\alpha_2</math>'</i>	Supposed constant	Fixed by the condition that $V_{u2}$ (entry to stator) = (constant) $V_{u1}$ (entry to rotor) = $a - b/r$	Supposed constant	Not far from constant	Ignored
F. <i>Constant reaction</i>	Constant	$V_u = ar^n \pm \frac{b}{r}$	From radial equilibrium	Constant	Yes
G. <i>Forced vortex</i>	Increases with $r^2$	$V_u$ proportional to $r$	From radial equilibrium	Varies with radius	Yes
H. <i>'Exponential'</i>	Constant	$V_u = a \pm \frac{b}{r}$	From radial equilibrium	Varies with radius	Yes

### C. NASA GRAPE Sample Input

'3% Span – Hybrid Vortex Case C'

&grid1 jmax=300 kmax=60 ntetyp=3 nairf=5 nibdst=7 nobshp=7

jairf=121 jtebot=25 jtetop=276 norda=0 3 maxita= 0 3000 nout=4

dsi=1.18733e-5 xle=0.0 xte=0.3307 xleft=-.1005 xright=.45 rcorn=0.025

&end

&grid2 nobcas=0 nle=40 nte=22 dsra=.49 dsle=.001 dste=.0007

pitch=0.2011 yscl=1. xfrac=1. dsobi=.0017 dswex=.0047

aaai=0.45 bbbi=0.45 ccci=0.35 dddi=0.35 jwakex=1 kwakex=0 csmoo=1.

jcaph=28

&end

### D. NASA RVCQ3D Sample Input

'3% Span – Hybrid Vortex Case C'

&nl1 m=MMM n=NNN mtl=xxxMTLxxx mil=xxxMILxxx &end

&nl2 nstg=4 ivdt=1 irs=1 eps=1.0 ndis=2 cfl=5.6 avisc2=0. avisc4=.5

ipc=0 pck=.1 refm=0.4 hcuspk=.10 ausmk=0.6 icdup=0 &end

&nl3 ibcinu=1 ibcinv=1 ibcex=1 itmax=4340 iresti=0 iresto=1 ires=10

icrnt=50 ixrm=0 ibcext0=1 &end

&nl4 amle=.295816 alle=21.141 bete=5.709 prat=0.965439 p0in=1. t0in=1.

g=1.4 &end

&nl5 ilt=5 jedge=35 renr=5.93e6 prnr=.7 tw=0. vispwr=.667

itur=2 cmutm=14. &end

&nl6 omega=-0.24 nblade=20 nmn=20 &end

&nl7 tintens=.01 tlength=2.20e-5 hrough=0. &end

-0.1676 -0.1482 -0.1289 -0.0859 -0.0429 0.0000 0.0355 0.0711 0.1067

0.1423 0.1778 0.2134 0.2490 0.2846 0.3201 0.3572 0.3942 0.4313

0.4683 0.5053

0.6224 0.6263 0.6302 0.6336 0.6369 0.6403 0.6550 0.6698 0.6846

0.6993 0.7141 0.7289 0.7436 0.7584 0.7732 0.7774 0.7816 0.7858

0.7899 0.7942

1.0000 1.0171 1.0342 1.0492 1.0641 1.0790 1.0649 1.0508 1.0366

1.0225 1.0084 0.9943 0.9802 0.9660 0.9519 0.9489 0.9459 0.9429

0.9399 0.9369



### E. Sample CFX Inlet Velocity Profile File

The following file is the inlet initialized velocity profile which was imported into the simulations to assume same rotor inlet conditions from the inlet guide vane for all four cases. The file is in '.csv' format and provides the unit vector 's velocity direction at corresponding location.

[Name]

R1 Inlet

[Spatial Fields]

x            y            z

[Data]

			Velocity Direction in Stn	Velocity Direction in Stn	Velocity Direction in Stn
x [ in ]	y [ in ]	z [ in ]	Frame u	Frame v	Frame w
18.39	0	-5.413	0	0.159538	0.987192
18.1662	0	-5.413	0	0.161425	0.986885
17.9424	0	-5.413	0	0.163357	0.986567
17.7186	0	-5.413	0	0.165336	0.986237
17.4948	0	-5.413	0	0.167362	0.985896
17.271	0	-5.413	0	0.169437	0.985541
17.0472	0	-5.413	0	0.171564	0.985173
16.8234	0	-5.413	0	0.173744	0.984791
16.5996	0	-5.413	0	0.17598	0.984394
16.3758	0	-5.413	0	0.178272	0.983981
16.152	0	-5.413	0	0.180625	0.983552
15.9282	0	-5.413	0	0.183039	0.983106
15.7044	0	-5.413	0	0.185517	0.982641
15.4806	0	-5.413	0	0.188062	0.982157
15.2568	0	-5.413	0	0.190676	0.981653
15.033	0	-5.413	0	0.193363	0.981127
14.8092	0	-5.413	0	0.196125	0.980579
14.5854	0	-5.413	0	0.198966	0.980006
14.3616	0	-5.413	0	0.201888	0.979409
14.1378	0	-5.413	0	0.204895	0.978784
13.914	0	-5.413	0	0.207991	0.978131
13.6902	0	-5.413	0	0.21118	0.977447
13.4664	0	-5.413	0	0.214467	0.976731
13.2426	0	-5.413	0	0.217854	0.975981

[Data]			Velocity Direction in Stn	Velocity Direction in Stn	Velocity Direction in Stn
x [ in ]	y [ in ]	z [ in ]	Frame u	Frame v	Frame w
13.0188	0	-5.413	0	0.221347	0.975195
12.795	0	-5.413	0	0.224951	0.97437
12.5712	0	-5.413	0	0.228671	0.973504
12.3474	0	-5.413	0	0.232513	0.972593
12.1236	0	-5.413	0	0.236482	0.971636
11.8998	0	-5.413	0	0.240585	0.970628
11.676	0	-5.413	0	0.244827	0.969567
11.4522	0	-5.413	0	0.249218	0.968447
11.2284	0	-5.413	0	0.253763	0.967266
11.0046	0	-5.413	0	0.258471	0.966019
10.7808	0	-5.413	0	0.26335	0.9647
10.557	0	-5.413	0	0.26841	0.963305
10.3332	0	-5.413	0	0.27366	0.961827
10.1094	0	-5.413	0	0.27911	0.960259
9.8856	0	-5.413	0	0.284773	0.958595
9.6618	0	-5.413	0	0.290659	0.956827
9.438	0	-5.413	0	0.296782	0.954945
9.2142	0	-5.413	0	0.303155	0.952941
8.9904	0	-5.413	0	0.309793	0.950804
8.7666	0	-5.413	0	0.316712	0.948522
8.5428	0	-5.413	0	0.323928	0.946082
8.319	0	-5.413	0	0.331461	0.943469
8.0952	0	-5.413	0	0.339329	0.940668
7.8714	0	-5.413	0	0.347553	0.93766
7.6476	0	-5.413	0	0.356157	0.934426
7.4238	0	-5.413	0	0.365164	0.930943
7.2	0	-5.413	0	0.374601	0.927186

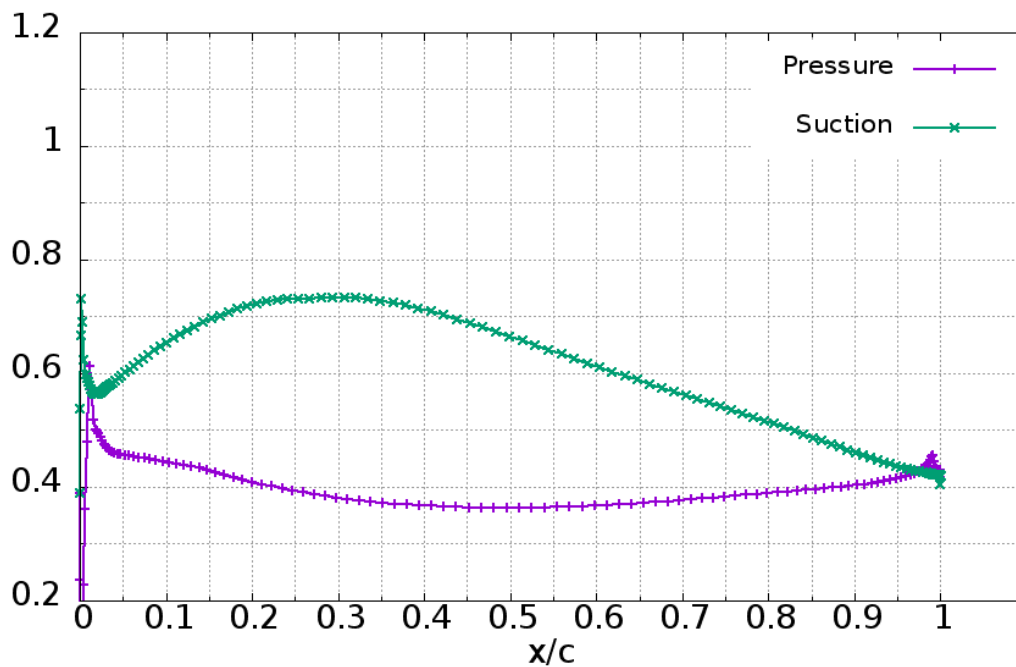
**F. 2D Mach Profile Output for the Baseline Case****Mach profile, 3 percent**

Figure F.1 Free Vortex Baseline 3% Span location 2D Mach Profile

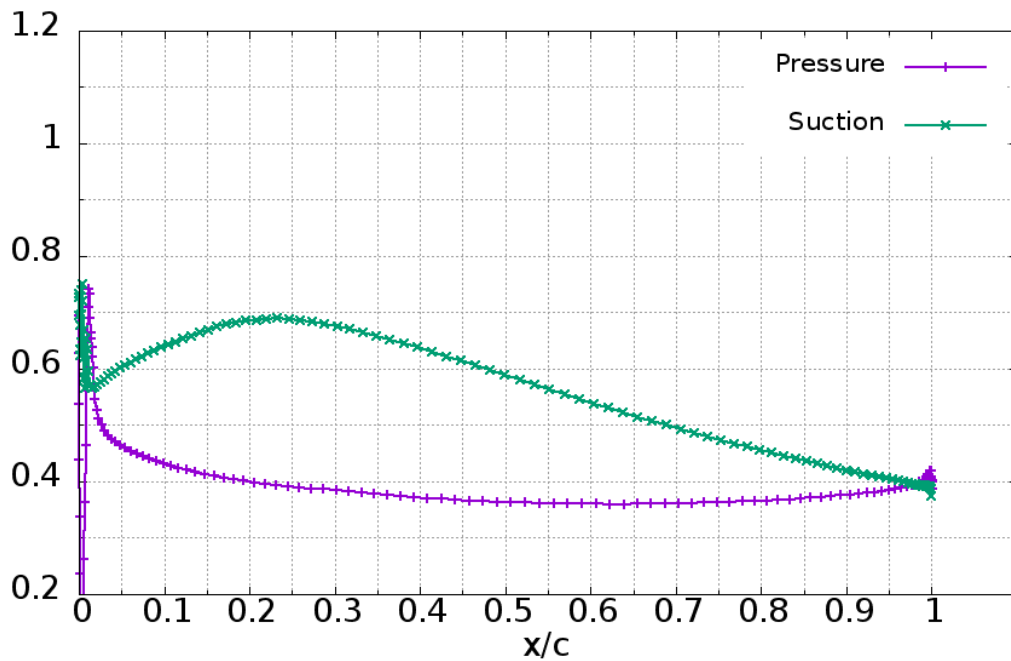
**Mach profile, 35 percent**

Figure F.2 Free Vortex Baseline 35% Span location 2D Mach Profile

## Mach profile, 61 percent

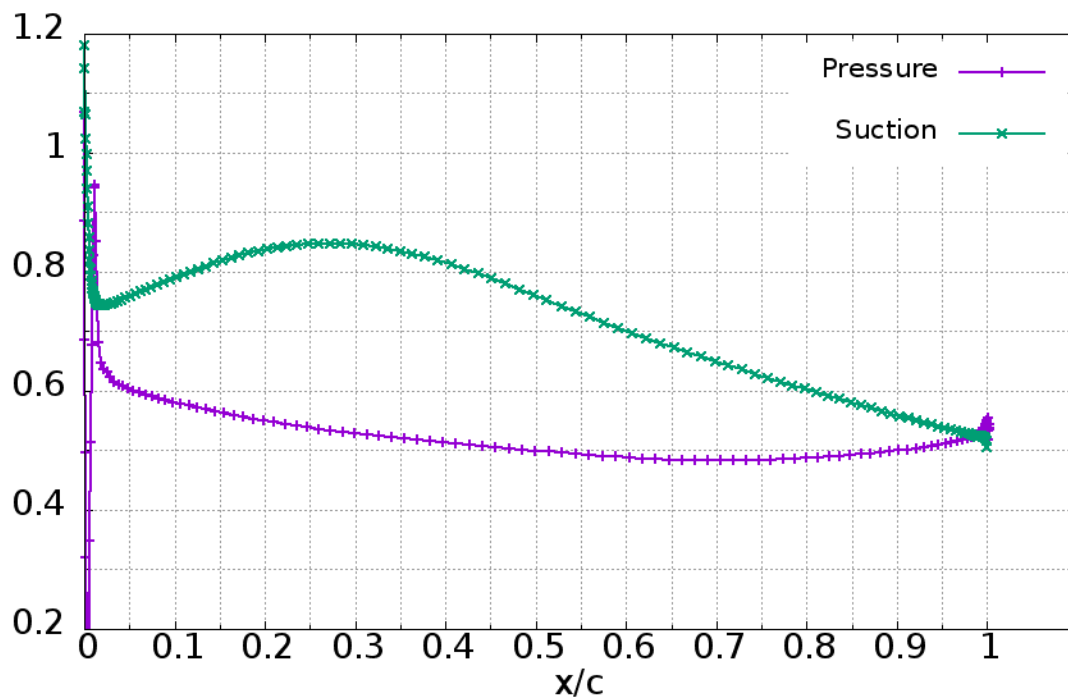


Figure F.3 Free Vortex Baseline 61% Span location 2D Mach Profile

## Mach profile, 82 percent

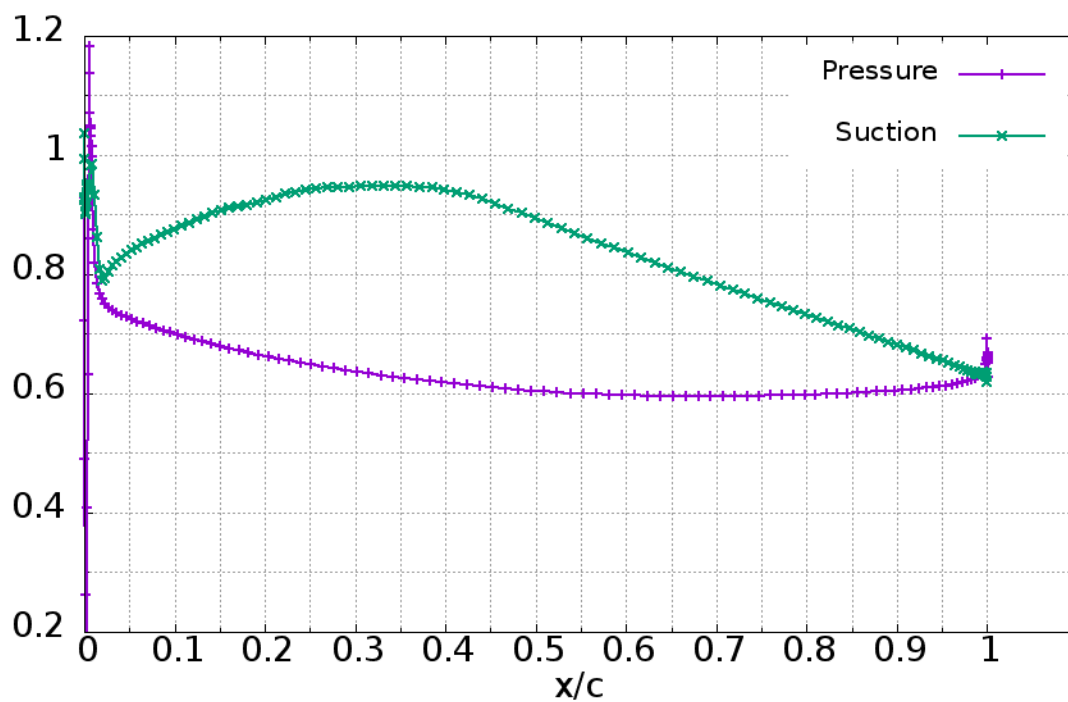


Figure F.4 Free Vortex Baseline 82% Span location 2D Mach Profile

## Mach profile, 98 percent

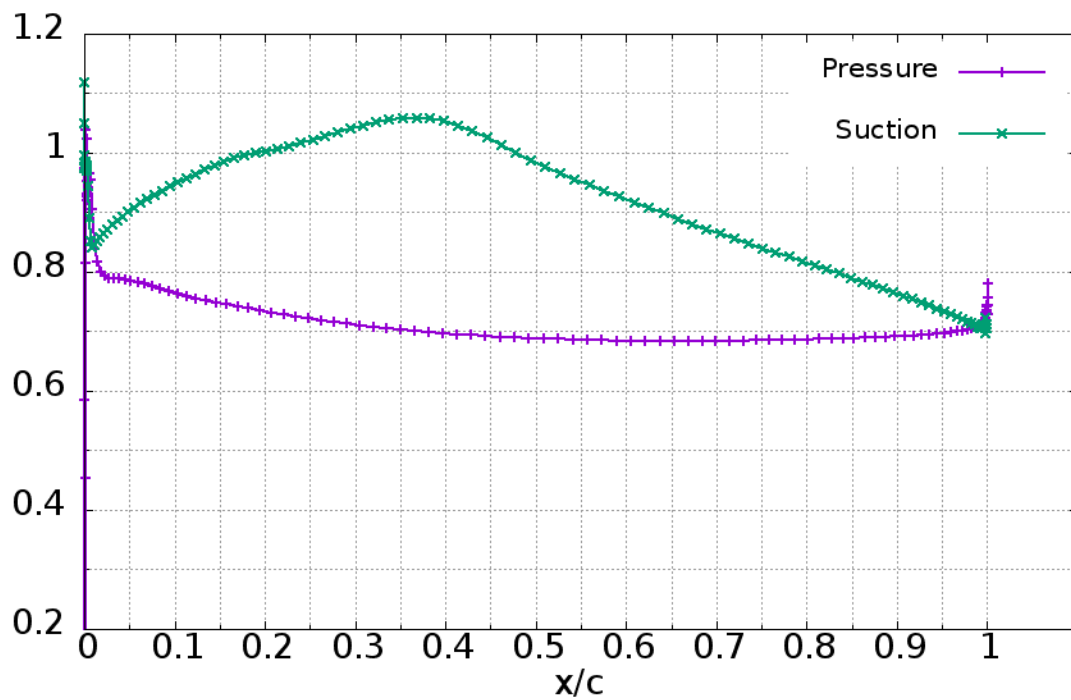
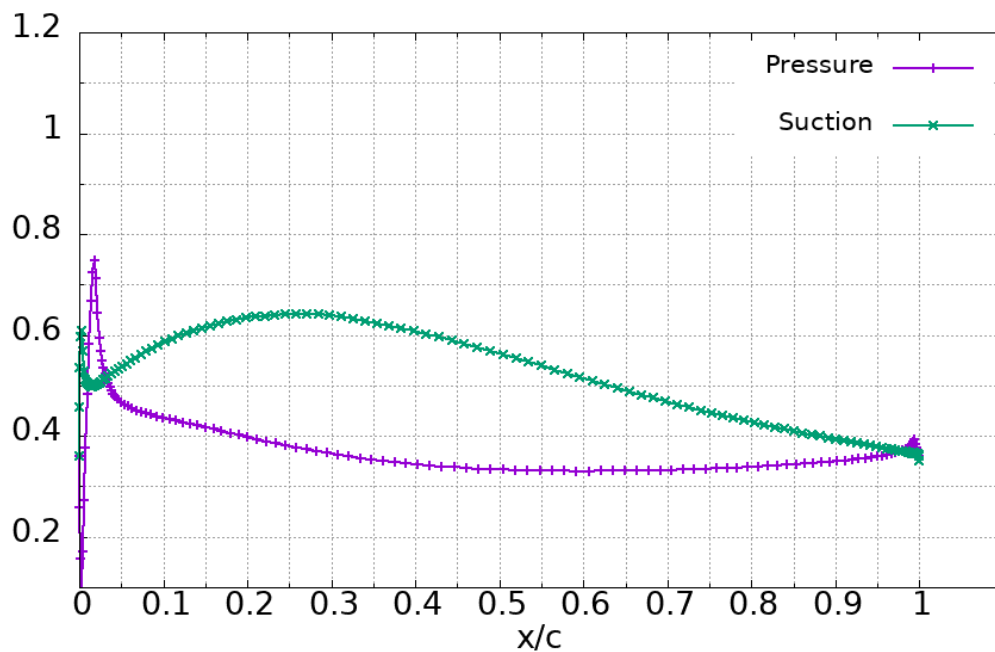
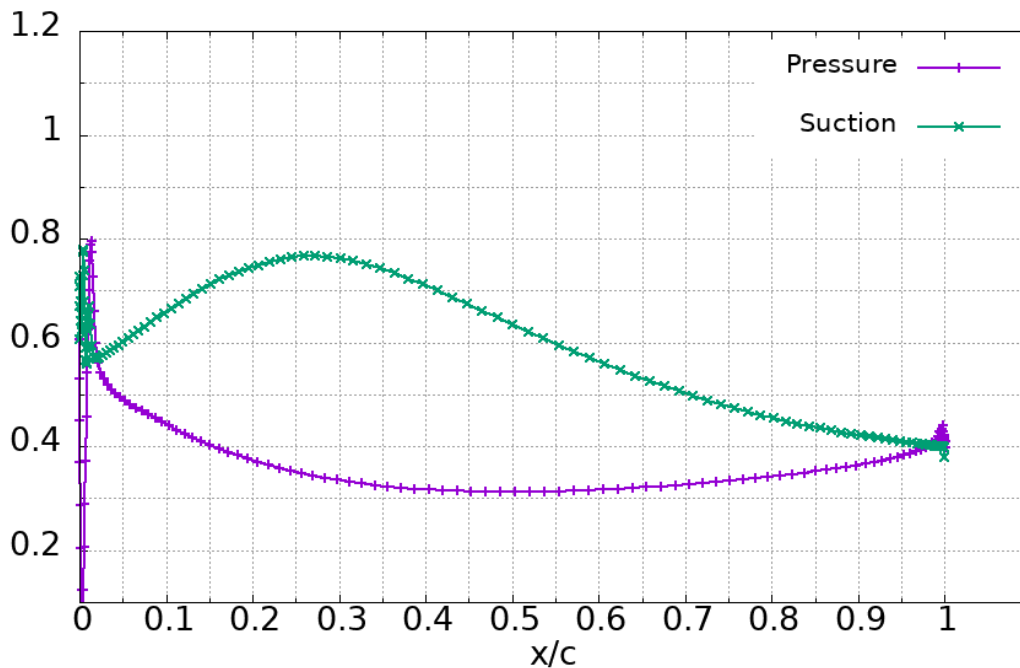


Figure F.5 Free Vortex Baseline 98% Span location 2D Mach Profile

**G. 2D Mach Profile Output for the Hybrid Vortex Case C****Mach profile, 3 percent***Figure G.6 Hybrid Vortex Case C 3% Span location 2D Mach Profile***Mach profile, 35 percent***Figure G.7 Hybrid Vortex Case C 35% Span location 2D Mach Profile*

## Mach profile, 61 percent

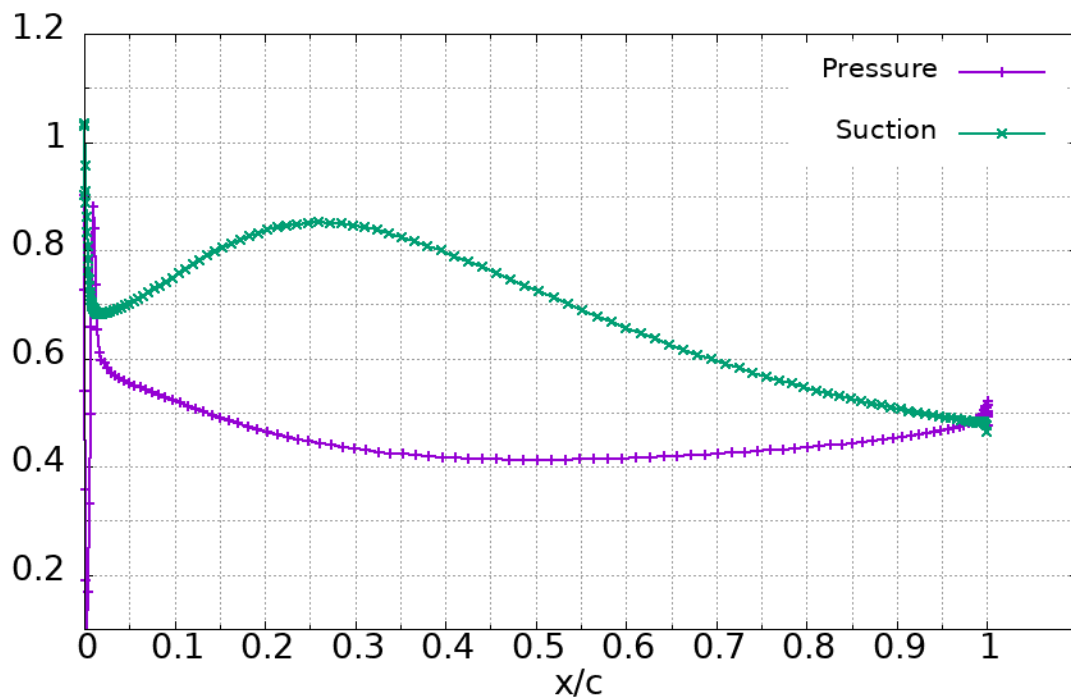


Figure G.8 Hybrid Vortex Case C 61% Span location 2D Mach Profile

## Mach profile, 82 percent

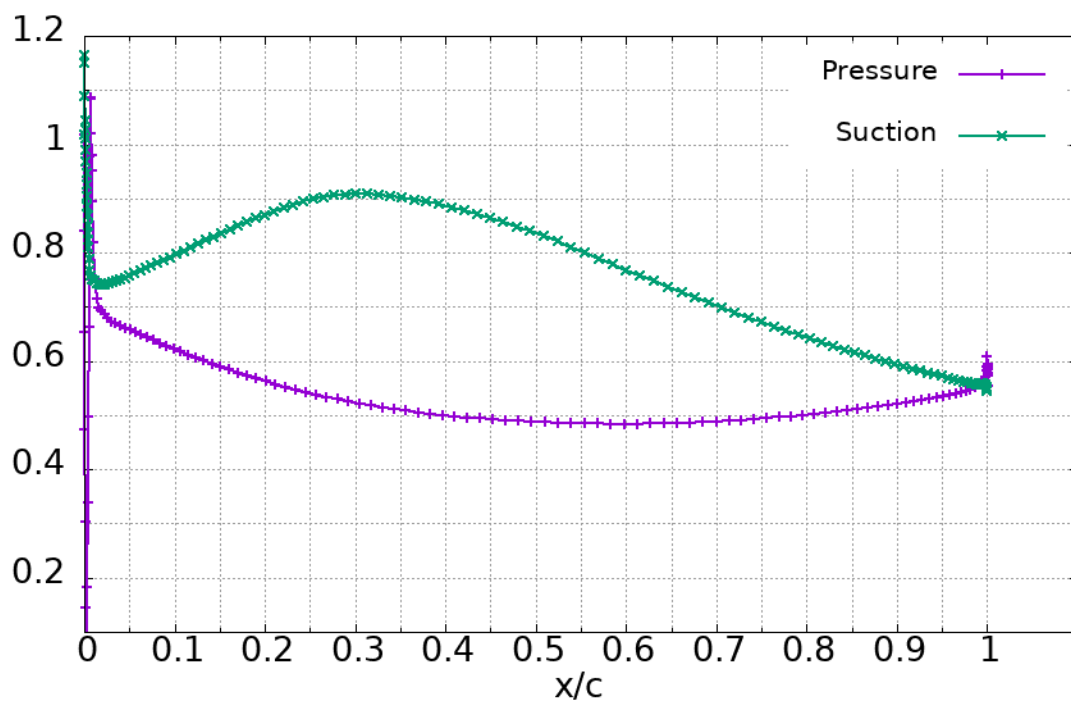


Figure G.9 Hybrid Vortex Case C 82% Span location 2D Mach Profile

## Mach profile, 98 percent

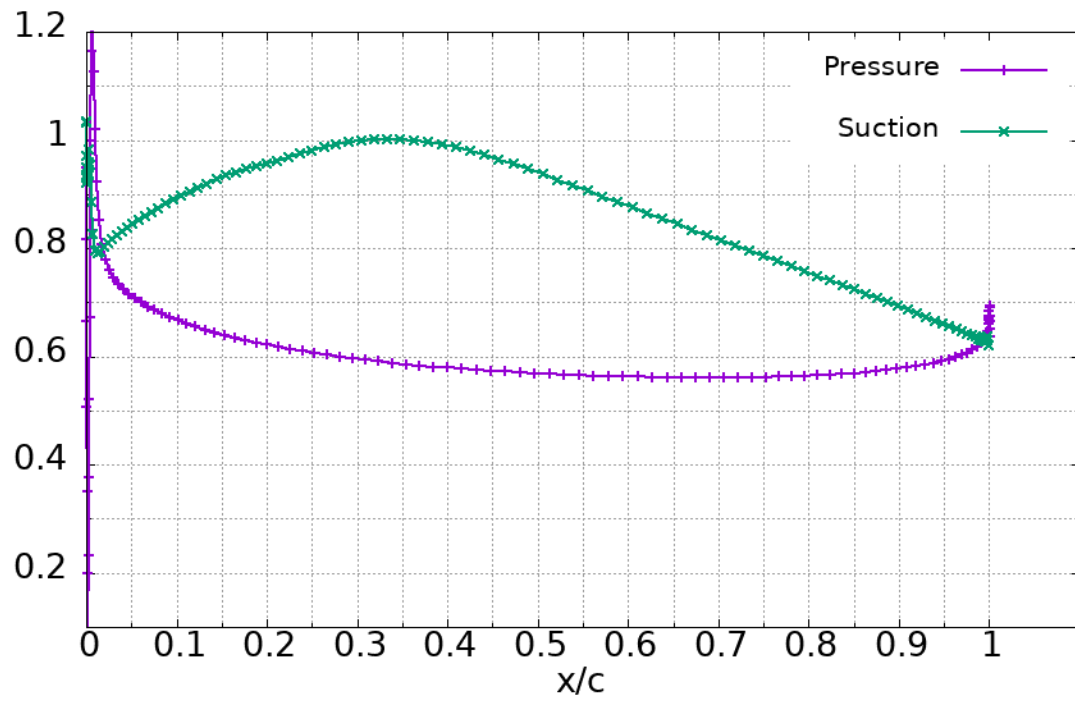


Figure G.10 Hybrid Vortex Case C 98% Span location 2D Mach Profile



## H. 2D Blade Geometry Comparison

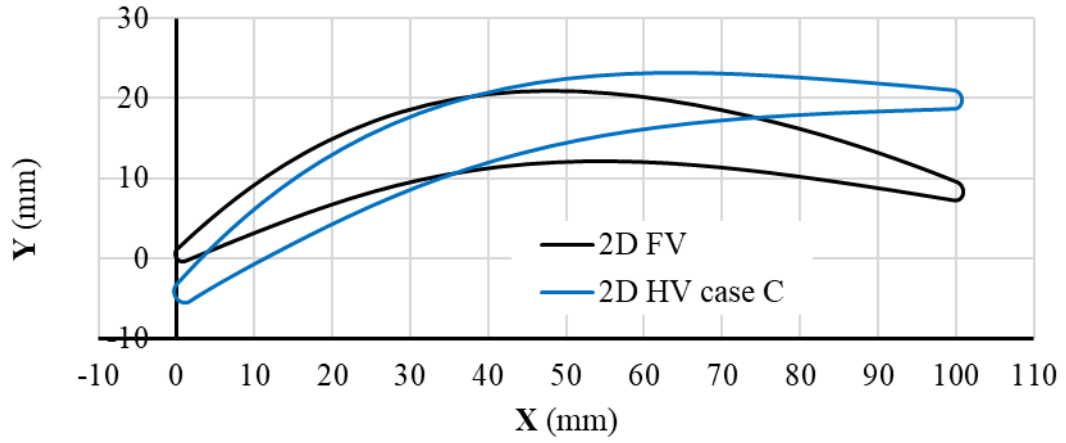


Figure H.11 2D Airfoil Comparison at 3% Span location

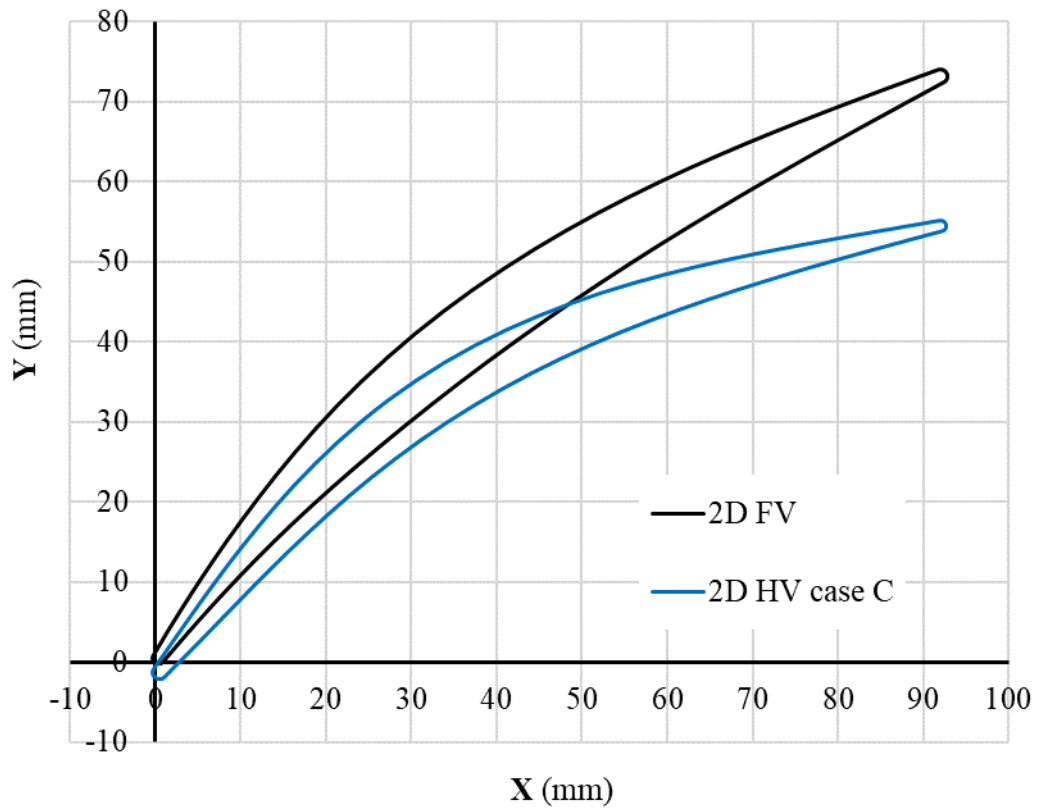


Figure H.12 2D Airfoil Comparison at 35% Span location

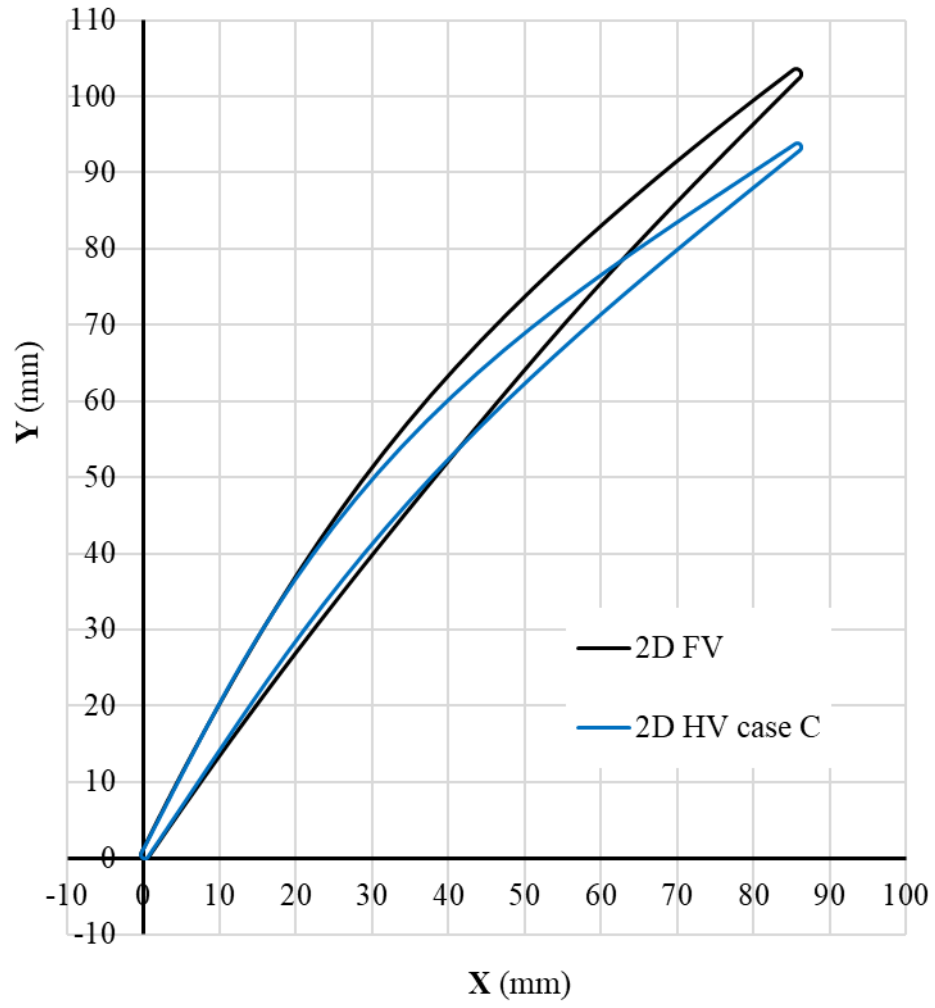


Figure H.13 2D Airfoil Comparison at 61% Span location

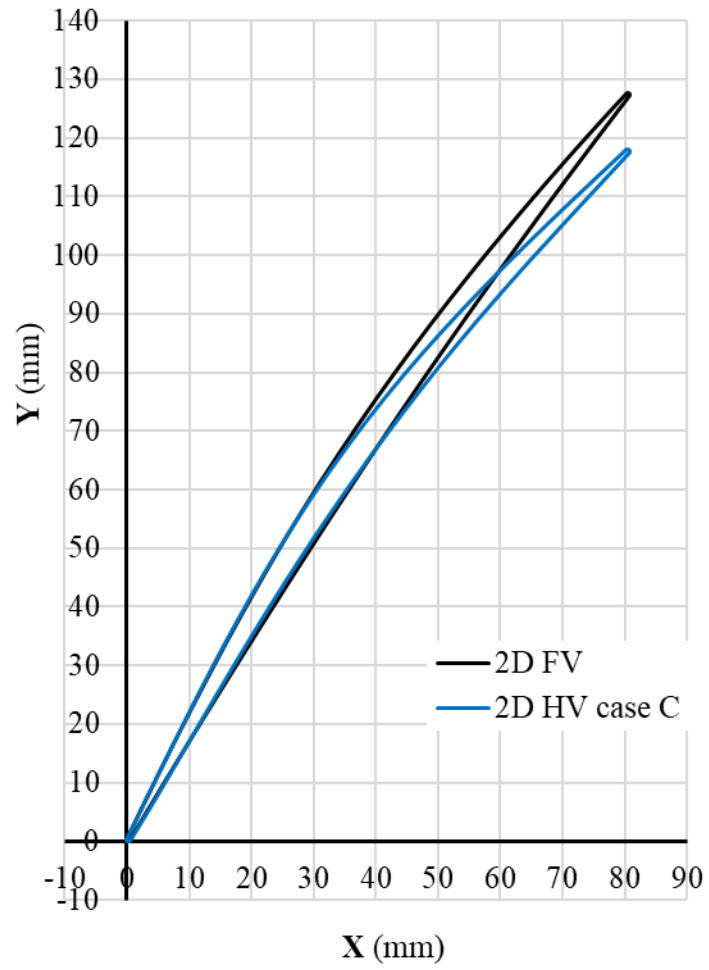


Figure H.14 2D Airfoil Comparison at 82% Span location

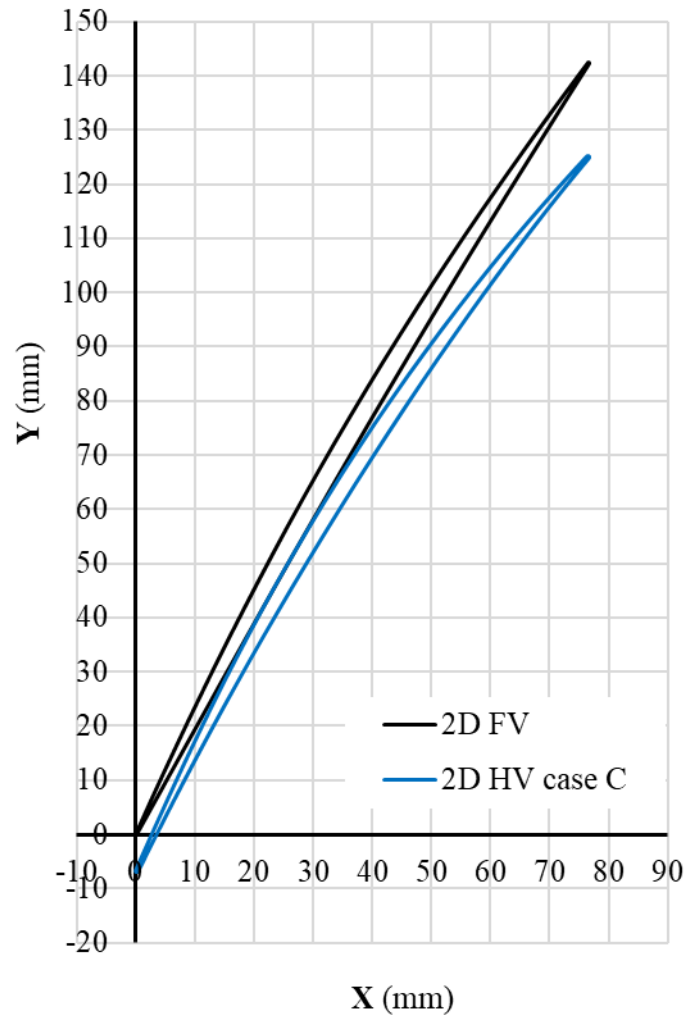


Figure H.15 2D Airfoil Comparison at 98% Span location